NONLINEAR MODELING OF PIEZOELECTRIC STACK ACTUATORS WITH FLEXURE BASED DISPLACEMENT AMPLIFIER MECHANISMS

A THESIS SUBMITTED TO
THE GRADUATE SCHOOL OF NATURAL AND APPLIED SCIENCES
OF
MIDDLE EAST TECHNICAL UNIVERSITY

BY

OZAN YURDAKUL

IN PARTIAL FULFILLMENT OF THE REQUIREMENTS
FOR
THE DEGREE OF MASTER OF SCIENCE
IN
MECHANICAL ENGINEERING

AUGUST 2022

Approval of the thesis:

NONLINEAR MODELING OF PIEZOELECTRIC STACK ACTUATORS WITH FLEXURE BASED DISPLACEMENT AMPLIFIER MECHANISMS

submitted by **OZAN YURDAKUL** in partial fulfillment of the requirements for the degree of **Master of Science** in **Mechanical Engineering, Middle East Technical University** by,

Prof. Dr. Halil Kalıpçılar
Dean, Graduate School of **Natural and Applied Sciences**

Prof. Dr. M. A. Sahir Arıkan
Head of the Department, **Mechanical Engineering**

Assoc. Prof. Dr. M. Bülent Özer
Supervisor, **Mechanical Engineering, METU**

Dr. Erdinç N. Yıldız
Co-Supervisor, **Ekinoks-AG Inc.**

Examining Committee Members:

Prof. Dr. Yiğit Yazıcıoğlu
Mechanical Engineering Dept., METU

Assoc. Prof. Dr. M. Bülent Özer
Mechanical Engineering Dept., METU

Assist. Prof. Dr. Kutluk Bilge Arıkan
Mechanical Engineering Dept., TED University

Prof. Dr. S. Çağlar Başlamışlı
Mechanical Engineering Dept., Hacettepe University

Assist. Prof. Dr. Orkun Özşahin
Mechanical Engineering Dept., METU

Date: 26.08.2022

I hereby declare that all information in this document has been obtained and presented in accordance with academic rules and ethical conduct. I also declare that, as required by these rules and conduct, I have fully cited and referenced all material and results that are not original to this work.

Name, Last name : Ozan Yurdakul

Signature :

ABSTRACT

NONLINEAR MODELING OF PIEZOELECTRIC STACK ACTUATORS WITH FLEXURE BASED DISPLACEMENT AMPLIFIER MECHANISMS

Yurdakul, Ozan
Master of Science, Mechanical Engineering
Supervisor: Assoc. Prof. Dr. M. Bülent Özer
Co-Supervisor: Dr. Erdinç N. Yıldız

August 2022, 109 pages

In this thesis, modeling methods for piezoelectric stack actuators (PSA) are studied. Both linear and nonlinear modeling methodologies are provided. FEM which is derived from constitutive piezoelectric equations is implemented to model linear behavior of piezoelectricity. Validation of the FEM model is performed through experiments. It is observed that modeling and test results are matched with high quality.

Rhombus type amplifier mechanism (RTAM) is selected for this study after conducting a detailed literature survey about flexure-based displacement amplifier mechanisms (FDAMs). The amplifier mechanism is designed and optimized via FEM. After manufacturing the mechanism, it is also validated via tests. In addition, accuracy of both analytical and geometrical formulas in literature are compared.

Although linear modeling is sufficient to design an actuator, the model should be made more accurate by adding nonlinearities for precise engineering applications.

PSAs exhibits highly nonlinear behavior, and the major source of this nonlinearity is hysteresis. Bouc-Wen model is utilized to represent hysteretic behavior for this work. Modified Bouc-Wen models in the literature are compiled comprehensively. As these models only work well in limited voltage ranges with symmetrical hysteresis shapes, a new type modified model named as Multivalued Bouc-Wen model (MVB-W) is developed to increase matching performance in extended input voltage ranges up to 150 V. Moreover, creep, another cause of nonlinearity, is modeled, and its parameters are identified through testing. Since PSAs are generally utilized in an amplifier mechanism under prestress, effect of prestress on hysteresis and creep is also investigated.

Keywords: Piezoelectric, FEM, Bouc-Wen model, Hysteresis, Nonlinear

ÖZ

PİEZOELEKTRİK YIĞIN EYLEYİCİLERİN VE ESNEK MEKANİK YÜKSELTİCİ MEKANİZMALARIN DOĞRUSAL OLMAYAN MODELLENMESİ

Yurdakul, Ozan
Yüksek Lisans, Makina Mühendisliği
Tez Yöneticisi: Doç. Dr. M. Bülent Özer
Ortak Tez Yöneticisi: Dr. Erdinç N. Yıldız

Ağustos 2022, 109 sayfa

Bu tezde, piezoelektrik yığın eyleyicileri için modelleme yöntemleri incelenmiştir. Bu eyleyiciler için hem doğrusal hem de doğrusal olmayan modelleme metodolojisi uygulanmıştır. Genel piezoelektrik denklemlerinden türetilen sonlu elemanlar modeli, piezoelektrik malzemenin doğrusal davranışını modellemek için kullanılmıştır. Sonlu elemanlar modelinin doğrulaması, deneyler vasıtasıyla gerçekleştirilmiş, modelleme ve test sonuçlarının yüksek kalitede eşleştiği gözlemlenmiştir.

Mekanik yükselticiler hakkında ayrıntılı bir literatür araştırması yapıldıktan sonra bu çalışma için Rhombus tipi yükseltici mekanizma seçilmiştir. Mekanik yükseltici mekanizması sonlu elemanlar metodu ile tasarlanmış ve optimize edilmiştir. Tasarlanan mekanizma, üretildikten sonra deneysel olarak doğrulanmıştır. Ayrıca literatürdeki analitik ve geometrik formüllerin doğrulukları karşılaştırılmıştır.

Doğrusal modelleme bir eyleyici tasarlamak için yeterli olsa da, hassas mühendislik uygulamaları için doğrusal olmayan kısımlar eklenerek, model daha doğru hale getirilmelidir. Piezoelektrik eyleyiciler oldukça doğrusal olmayan davranış sergiler ve bu doğrusal olmamanın ana sebebi histerezistir. Literatürde bulunan histerezis modelleri sunulduktan sonra, bu çalışma için histeretik davranışı temsil etmek amacıyla Bouc-Wen modeli kullanılmıştır ve literatürdeki modifiye Bouc-Wen modelleri de kapsamlı bir şekilde derlenmiştir. Bu modeller sadece sınırlı voltaj aralıklarında ve simetrik histerezis için iyi çalıştığından, geniş giriş voltaj aralıklarında, (0,150 V) eşleştirme performansını artırmak için çok değişkenli Bouc-Wen modeli olarak adlandırılan yeni bir modifiye Bouc-Wen modeli geliştirilmiştir. Bu çalışmada, Doğrusal olmamanın bir başka nedeni olan sünme de modellenmiş ve model parametreleri testler aracılığıyla bulunmuştur. Piezoelektrik eyleyiciler genellikle bir yükseltici mekanizmasında ön gerilim altında kullanıldığından, ön gerilimin histerezis ve sünme üzerindeki etkisi de ayrıca incelenmiştir.

Anahtar Kelimeler: Piezoelektrik, Sonlu elemanlar modeli, Bouc-Wen modeli, Histerezis, Doğrusal olmayan

To my family…

ACKNOWLEDGMENTS

I would like to sincerely thank my supervisor Associate Professor Dr. M. Bülent ÖZER for his direction, guidance and assistance through the study.

I would like to express my gratitude my co-supervisor and my manager Dr. Erdinç N. YILDIZ for teaching me essence of mechanical engineering, and his lead along this thesis.

I wish to express my appreciation to Fatih BÜKE and Egemen İŞERİ for their efforts in setting up test set-ups, and their guidance and assistance while carrying out experiments. I am grateful to my unit chief Dr. Tuğrul KOZAK for his understanding. Also, I would like to thank Ekinoks-AG Inc. for all the facilities they have provided.

Enormous thanks go to my lovely mother Aynur for her endless love and great compassion. Special thanks go to my father Süleyman, for his unconditional support and encouragement he provided me throughout my life. I am also grateful for having my beloved sister Öykü.

Finally, I would like to present my special and deepest gratitude to my beautiful wife Melis for her noble love, understanding and moral support she provided me.

TABLE OF CONTENTS

CHAPTERS

LIST OF TABLES

TABLES

LIST OF FIGURES

FIGURES

LIST OF ABBREVIATIONS

ABBREVIATIONS

UAV	Unmanned Aerial Vehicle
FSM	Fast Steering Mirror
PEA	Piezoelectric Actuator
PSA	Piezoelectric Stack Actuator
APA	Amplified Piezoelectric Actuator
FEA	Finite Element Analysis
FEM	Finite Element Modeling
FDAM	Flexure-based Displacement Amplifier Mechanism
RTAM	Rhombus-type Amplification Mechanism
EDM	Electro Discharge Machining
DOF	Degree of Freedom
LTI	Linear time invariant
B-W	Bouc-Wen
CB-W	Classical Bouc-Wen
MB-W	Modified Bouc-Wen
MVB-W	Multivalued Bouc-Wen
COMSOL	COMSOL Multiphysics 5.5
RMSE	Root Mean Square Error
RRMSE	Relative Root Mean Square Error

LIST OF SYMBOLS

SYMBOLS

R_{amp} = Amplification ratio

$\mathcal{L}$ = Lagrangian work

$\mathcal{W}$ = Virtual work

Ω = Surface, area

e_{rms} = Root Mean Square Error

δ = Relative Root Mean Square Error

CHAPTER 1

INTRODUCTION

1.1 Motivation of the Study

Recently, utilization of piezoelectric ceramics has become increasingly popular in precise positioning and stabilization systems. Ultra precision machining, scanning probe microscopes (SPMs), microelectromechanical systems (MEMS), antenna orientation stages, Tip-tilt platforms and fast steering mirrors are the leading application areas of piezoelectricity for precise positioning and stabilization systems.

Tip-Tilt Platforms are driven by three or four piezoelectric stack actuators (PSAs). Displacement on PSAs is transmitted by flexure hinges and becomes angular deformation. Tip-Tilt Platforms are the steering mechanism of electro optic systems named as fast steering mirrors (FSM). Many unmanned aerial vehicles (UAV), helicopters, airplanes and satellites rely on FSM for laser beam stabilization, a single axis tip-tilt platform is presented in Figure 1.1.

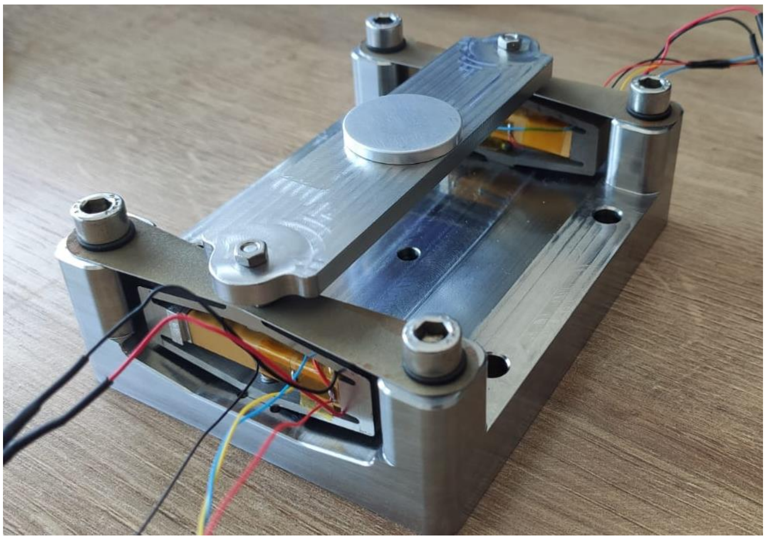

Figure 1.1 Single Axis Tip-Tilt Platform

The reason why piezoelectric actuators are frequently used in fine positioning and stabilization is that they have the following features:

- Accuracy and precision
- Fast response time
- High resolution
- High resonant frequency
- High stiffness
- High force generation capability
- Low energy consumption

Besides all these advantages, highly nonlinear behavior is the most important drawback of piezoelectric ceramic actuators. To overcome this disadvantage, an accurate nonlinear modeling is essential to control piezoelectric actuators with wide bandwith. Another constraint for piezoelectric actuators is limited stroke capacity. This limitation is generally solved with a mechanical amplification mechanism, as shown in Figure 1.2.

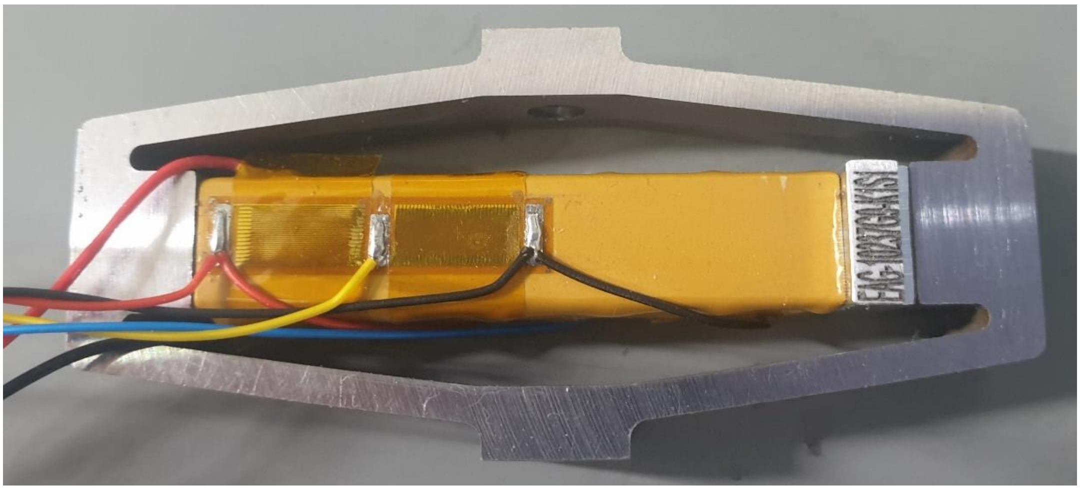

Figure 1.2 Mechanical Amplifier Mechanism

1.2 Objective and Scope of the Study

This thesis aims to establish a practical linear and nonlinear modeling methodology for piezoelectric stack actuators (PSA) with flexure-based displacement amplifier mechanisms (FDAM). In this scope, piezoelectricity is examined with focusing on PSA. Finite element modeling (FEM) is implemented to design amplifier mechanism and to model linear part of piezoelectric actuator. Then, hysteresis and creep nonlinearities in PSA is studied. Another objective of this study to develop a single degrees of freedom (SDOF) model by uniting linear and nonlinear models. Finally, it is aimed to verify validity of proposed models with experimental case studies.

1.3 Thesis Outline

The outline of the thesis is as follows:

- Detailed information about piezoelectricity is presented in Chapter 1

- In Chapter 2, Literature review on the subjects of modeling methods, amplifier mechanisms and nonlinearities present in piezoelectric actuators are presented by putting emphasis on hysteresis.
- Modeling methodology is given in Chapter 3. Linear finite element modeling in COMSOL is presented. A rhombus type mechanical amplifier designing and optimizing methodology is explained. In addition to linear model, non-linear modeling theory with focusing on hysteresis is presented. Also, a novel hysteresis Bouc-Wen model for extended voltage ranges is developed.
- Test setups for verification studies and experimental results are shown in Chapter 4
- Chapter 5 consists of four numerical case studies.
    - **Case Study I:** Single piezoelectric element is analyzed. COMSOL results and derived FEM formulation results are compared to clarify and validate COMSOL background formulation.
    - **Case Study II:** Developed hysteresis model is tested and its parameters are identified.
    - **Case Study III:** Creep model is tested and its parameters are identified.
    - **Case Study IV:** A flexure-based displacement amplification mechanism (FDAM) is designed, produced and verified via experiments.
- Finally, in the sixth and the last chapter, main research findings are concluded, and future works are suggested.

1.4 Piezoelectricity

1.4.1 Introduction to Piezoelectric Materials

Piezoelectric materials can be categorized under two headings that are natural and synthetic piezo materials. Quartz, Rochelle salt and ammonium phosphate are some examples for natural piezo materials. There are also some artificial materials that are non-piezoelectric and isotropic before the poling process. When these raw synthetic materials are heated above their curie temperature, and a strong electrical field is applied simultaneously, the material gains piezoelectricity and becomes anisotropic.

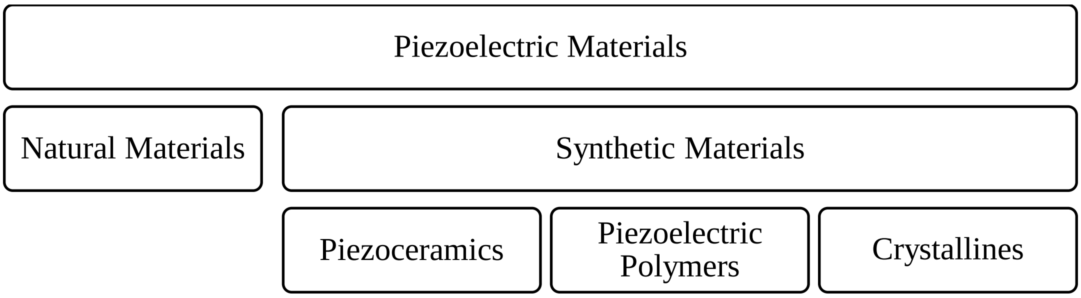

Figure 1.3 Piezoelectric Materials

In engineering applications, synthetic piezoelectric materials are preferred commonly as a result of strong electromechanical coupling coefficients. Piezoceramics, piezoelectric polymers and crystallines are three sub-groups of synthetic piezo materials. In piezoceramics family, barium titanate, lead niobrate, lead lanthanum zirconate titanate (PLZT) are the common materials [1]. However, Lead zirconate titanate (PZT) is the most preferred piezo material, especially in actuators thanks to high stiffness and actuation capacity of PZT. On the other hand, polyvinylidene fluoride (PVDF) is a piezo polymer material, and its low modulus elasticity makes PVDF ideal material for sensors [2].

1.4.2 History of Piezoelectric Materials

From the discovery of piezoelectric materials to today, development history of piezoelectric materials may be examined by dividing into 5 periods. These eras are the discovery period (19th Century), First World War Period, Second World War period and afterwards, Japanese Developments (1965 – 2000) and Recent History (2000– present).

19th Century: The word "piezo" is derived from a Greek word "piezein" which means to press or squeeze. That's why, it was named as piezoelectricity, when Pierre and Jacques Curie brothers discovered the way that generating charge or voltage by applying pressure on single crystal quartz in 1880 [3]. Afterward, this phenomenon was called as the direct piezoelectric effect. In 1881, inverse effect of piezoelectricity was suggested by G. Lippman. Two years later, this inverse phenomena was also confirmed experimentally by Curie brothers [3]. In 1894, findings of the Curie brothers were taken a step further by W. Voight. Curie brothers established some of the piezoelectric relations. However, the well-grounded relations between crystal structure and piezoelectricity are determined by W. Voight. He described linear behavior of piezo materials by mechanical stress tensors and electric vectors in 1884 [4].

First World War Period: In this era, the tragedy of the sinking of Titanic into the North Atlantic Ocean and demand for searching German U-boats under the sea created a need for an electronic device which measure the distance of the objects from the ships [5]. Although radio waves were the standard technology for that times, they don't propagate under sea water. That's why, the solution was using acoustic waves in an ultrasonic sonar device made from a piezoelectric crystal.

Second World War Period and Afterwards: During the time of the war, Japanese, American and Soviet Researchers independently found that some ceramic materials have dielectric and piezoelectric properties 100 times higher than natural crystals [6]. After the war, in 1945, the discovery of ferroelectricity in barium titanate ($BaTiO_3$) initiated the commercializing piezo products since producing and shaping barium titanate was inexpensive. This discovery is considered as a trigger event of the era of the piezoelectric ceramic and beginning of modern history of piezoelectricity. After the invention of barium titanate, it continued with merchandizing lead zirconate titanate (PZT) family which is the most preferred piezo material in today's world [6].

Japanese Developments (1965-2000): Japanese companies began to invest in piezo technology more and more from late 1960's to 1980's. However, this investment did not bring commercial success in the short term except for usage in cathode-ray tubes in black and white television receivers and small engine applications [7]. The main problem was high cost, brittle behavior, inadequate manufacturing methods, mechanical unreliability and complex driving circuit of piezo products [7]. In the late 1980's, developments in reliable piezo manufacturing technology like multi-layer co-firing process, and new integrated circuits laid the foundations of today's piezo technology. Also, another great contribution of that era was made by Kawai [8] by discovering piezoelectricity in polyvinylidene fluoride (PVDF) that is still the most favored material in piezo sensors.

Recent History: From 2000 to today commercial products of piezoelectric materials and their application areas have been increasing rapidly. Piezoelectric devices are preferred for positioning, sensing, vibration controlling and energy harvesting applications in automotive, acoustics, MEMS, biotechnology, aerospace and defense industries. Valves, fuel injectors, resonators, gyroscopes, smartphone speakers, sonar equipment, guidance systems, inkjet printers, disk drives, dental equipment, tire pressure sensors are just a few examples of growing application fields of piezoelectricity.

1.4.3 Piezoelectricity in Piezo Ceramics

Piezo ceramics have perovskite crystalline structure (ABO_3 structure) which is illustrated in Figure 1.4. For instance, molecular form of lead zirconate titanate (PZT) which is solution of lead zirconate ($PbZnO_3$) and lead titanate ($PbTiO_3$) has perovskite type moleculer structure [9]. Piezo ceramics have simple cubic molecular orientation and no dipole moments above the critical (curie) temperature (Figure 1.4a), while piezo ceramics have tetragonal orientation which leads to a dipole moment below the curie temperature (Figure 1.4b). However, overall polarization in material is zero since direction of dipole moments in each crystal is random (Figure 1.5a). In order to obtain a polarized piezo material, a strong DC electrical field is applied at a temperature close to curie temperature, therefore dipoles are directed towards electrical field direction (Figure 1.5b). Most of the dipoles are locked with small deviations when electrical field is removed, so permanent polarization is achieved (Figure 1.5c) [10].

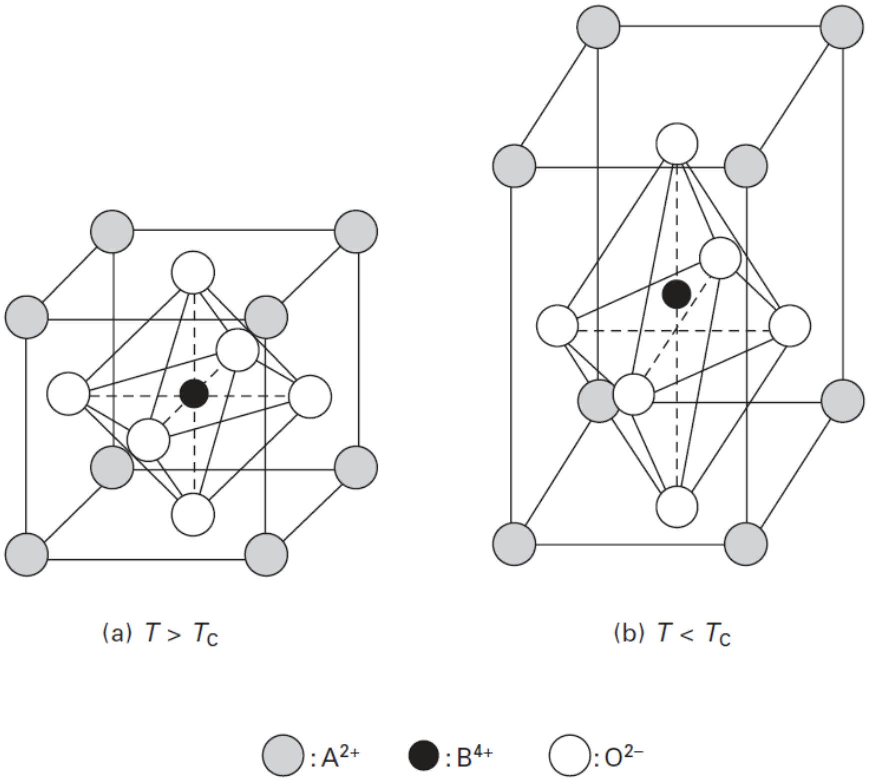

Figure 1.4 Schematic diagram of perovskite ABO_3 structure [9]

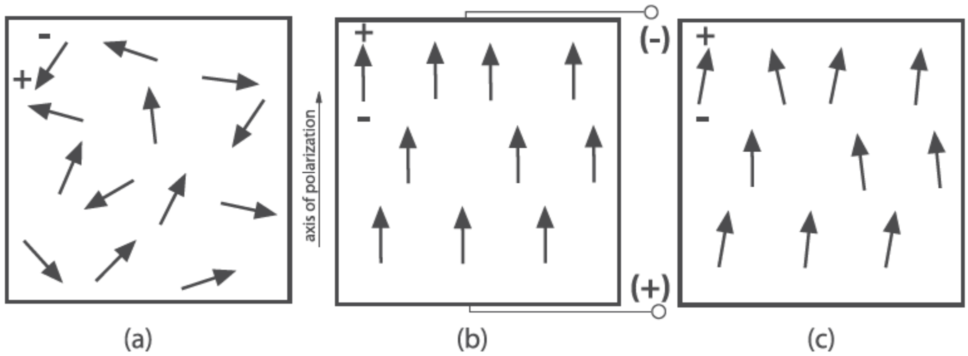

Figure 1.5 Poling process, a) before poling, b) during poling, c) after poling [10]

1.4.4 Piezoelectric Stack Actuators

Piezoelectric stack actuators (PSA) are quite popular in various engineering applications since they provide much longer strokes than single piezo element depending on the number of layers. Therefore, thickness of individual piezo layer becomes thinner and thinner to fit more layer inside PSA. In today’s commercial PSAs, the typical layer thickness is between 50-100 μm [11]. Thin ceramic sheets are generally produced with tape-casting after mixing and calcination steps, and the procedure continues with screen printing of inner electrodes that has thickness around 1 μm. Then, piezo layers with electrodes are laminated by stacking on top of each other, and the inner electrode and piezo ceramic is co-fired for sintering. As an electrode material, rare metals like platinum, palladium or silver-palladium alloy are used due to high sintering temperature of piezo ceramics that is above 1100 °C [12]. Sintering at low temperature with common metals may cause problems such as porosity, poor adhesion or high contact resistance between piezo and electrode layer [13]. As a final step, polarization is performed as explained in section 1.4.3. The whole procedure is summarized visually in Figure 1.6.

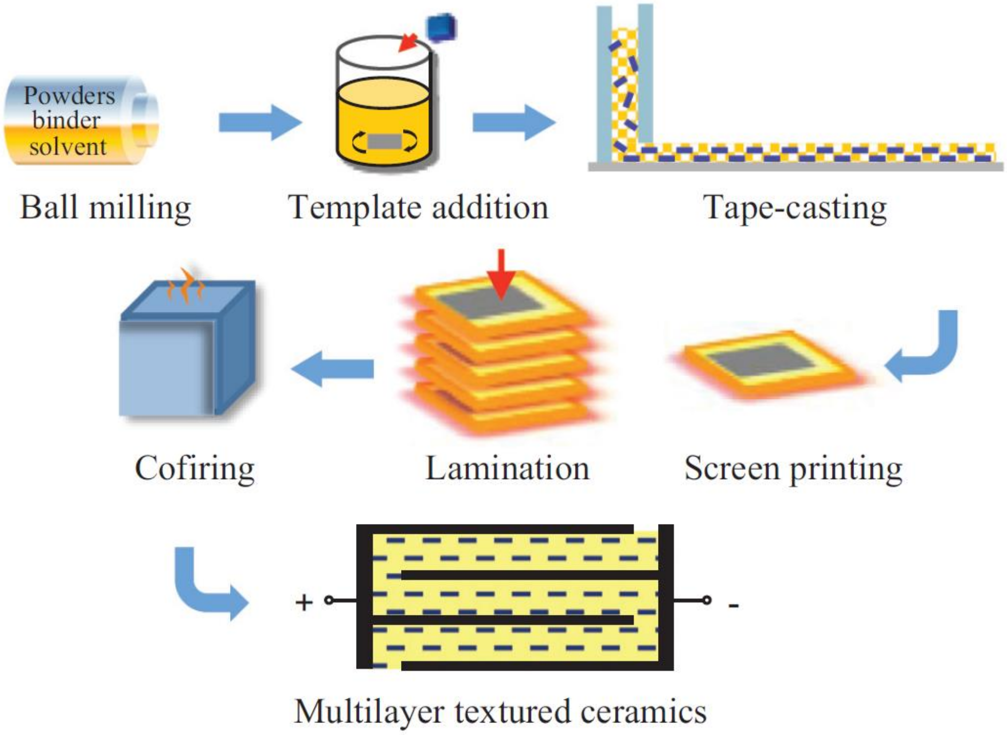

Figure 1.6 Procedure for PSA manufacturing [13]

PSAs have strong electro-mechanical coupling at moderate voltages (0-150V) and wide frequency range. In other words, PSAs converts electrical energy to mechanical energy efficiently. PSAs elongate with approximately 0.1% strain value at the maximum applied voltage. For example, a PSA with 30 mm length and 400 piezo layers which corresponds to 75 µm layer thickness can expand 30 µm when 2 kV/mm or 60 kV total voltage is applied. To supply this cumulative voltage value, utilizing 150 V in each electrode is enough for the PSA [14]. This feature makes PSAs powerful, and it explains why these type actuators are favored frequently. In below figure conventional PSAs with round and rectangular cross-sections are given.

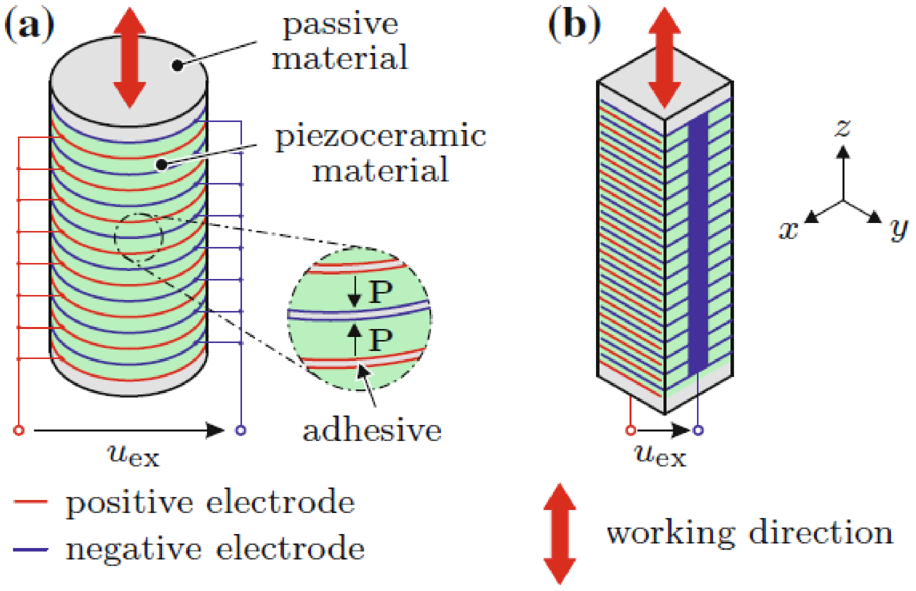

Figure 1.7 PSA with **(a)** round cross-section **(b)** rectangular cross-section [11].

Because of strong electrical field between very thin layers, hysteresis effect on PSAs are more dominant compared to single layer piezo material. Figure 1.8 depicts the growth of the hysteresis loops with increasing electrical field for different piezoelectric specimens [15]. It is apparent that the hysteresis loops are strongly dependent on voltage per unit length.

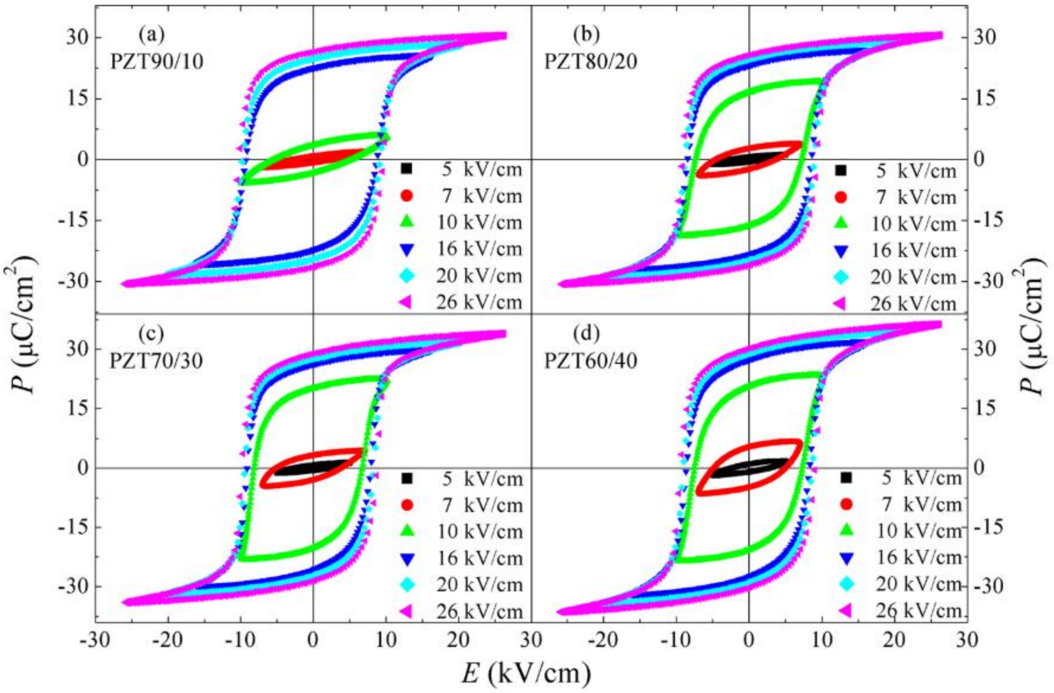

Figure 1.8 Field dependent P-E hysteresis loops [15]

Although P-E hysteresis is different than hysteresis between strain and voltage, it can be understood from the P-E hysteresis loop below that these two types of hysteresis are directly proportional to each other since small hysteresis loop between point C and point B represents strain-voltage hysteresis.

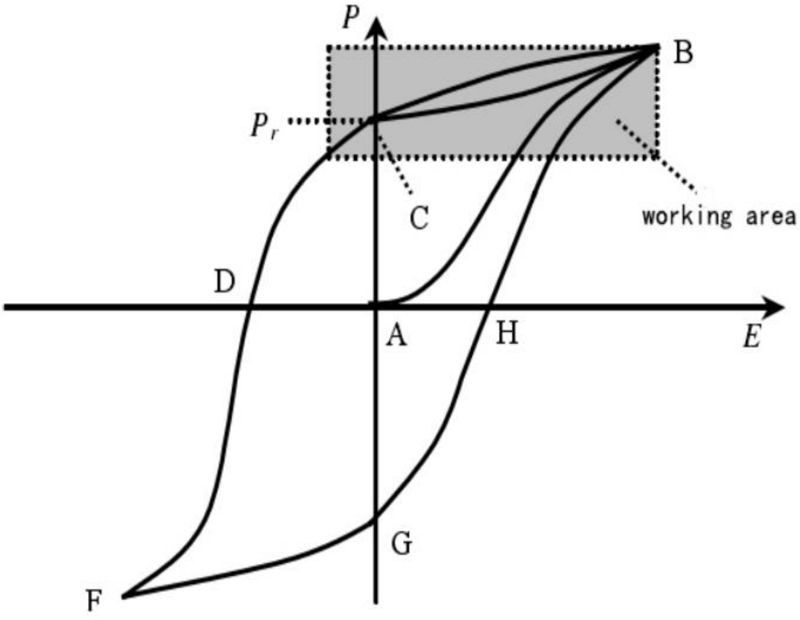

Figure 1.9 P-E hysteresis loops [16]

CHAPTER 2

LITERATURE SURVEY

Objective of this chapter is presenting a review of the studies on the modeling of piezoelectric materials, nonlinearities in piezoelectric materials and amplifier mechanisms.

2.1 Modeling Methods for Piezoelectric Actuators

Modeling methods for piezo materials may be divided into two categories. The first category is the exact methods. Direct analytical solution and transfer matrix method are the two sub-categories [17]. Dynamic analytical solution was derived by Liu [18]. Although this analytical solution matches well with experimental results, applying this method to hundreds of thin piezo layers or applying it to a complex geometry is cumbersome. A simpler method which is called as transfer matrix method was proposed by Bloomfield [19]. His method is based on continuity rule of boundary conditions in each layer of multi-layer piezo stack actuators. The second category is the approximate methods. The first approximate method is lumped model, which is quite common in piezo modeling. For a piezoelectric stack actuator, a non-linear lumped-parameter model is derived by Goldfarb [20]. He also modeled and measured the hysteresis behavior of piezo stack actuators, and his outcome of hysteresis occurring between voltage and displacement, not between charge and displacement, at low frequencies is valuable.

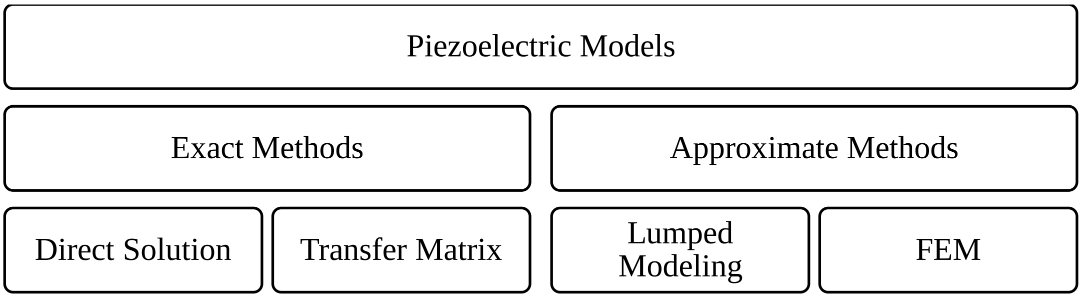

Figure 2.1 Piezoelectric models

A more powerful tool for modeling PEA is finite element modeling (FEM) which was first introduced by Allik and Hughes [21]. In the article, finite element formulation was derived by using linear piezoelectric constitutive equations and variational principle for piezoelectric continuum. Although, there has been huge improvements in FEM of piezoelectric structures, the derived equation set by Allik & Hughes [21] is still utilized in whole commercial FEM software for piezoelectricity. For PEA modeling, FEM begins to become prominent among all other modeling methods like all other disciplines of mechanical engineering [22],[23].

2.2 Nonlinearities in Piezoelectric Actuators

Piezoelectric actuators exhibit highly nonlinear behavior. In general, linear modeling results may deviate from actual results with approximately 15% margin of error due to nonlinear characteristics of piezo materials [24],[25]. Moreover, in the study of Barret and Quate [26], it was reported that nonlinearities may cause up to 40% error in positioning. In literature, hysteresis and creep (drift) are the two principal inherent nonlinear characteristics of piezoelectric materials.

Voltage excitation is the common method to steer electromechanical actuators due to ease of implementation. However, in piezoelectric actuators, this method brings hysteresis and creep, resulting in nonlinearities between voltage and displacement. On the other hand, charge driven actuators show almost no hysteresis behavior, but implementation of a charge driver is complicated because of long design and precise calibration processes [27],[28]. The third way of steering piezoelectric actuators in literature is capacitor insertion method. Even though this method eliminates both hysteresis and creep, this method severely restricts the movement capacity because total voltage is divided between the inserted capacitor and piezoelectric actuator as illustrated in Figure 2.2c.

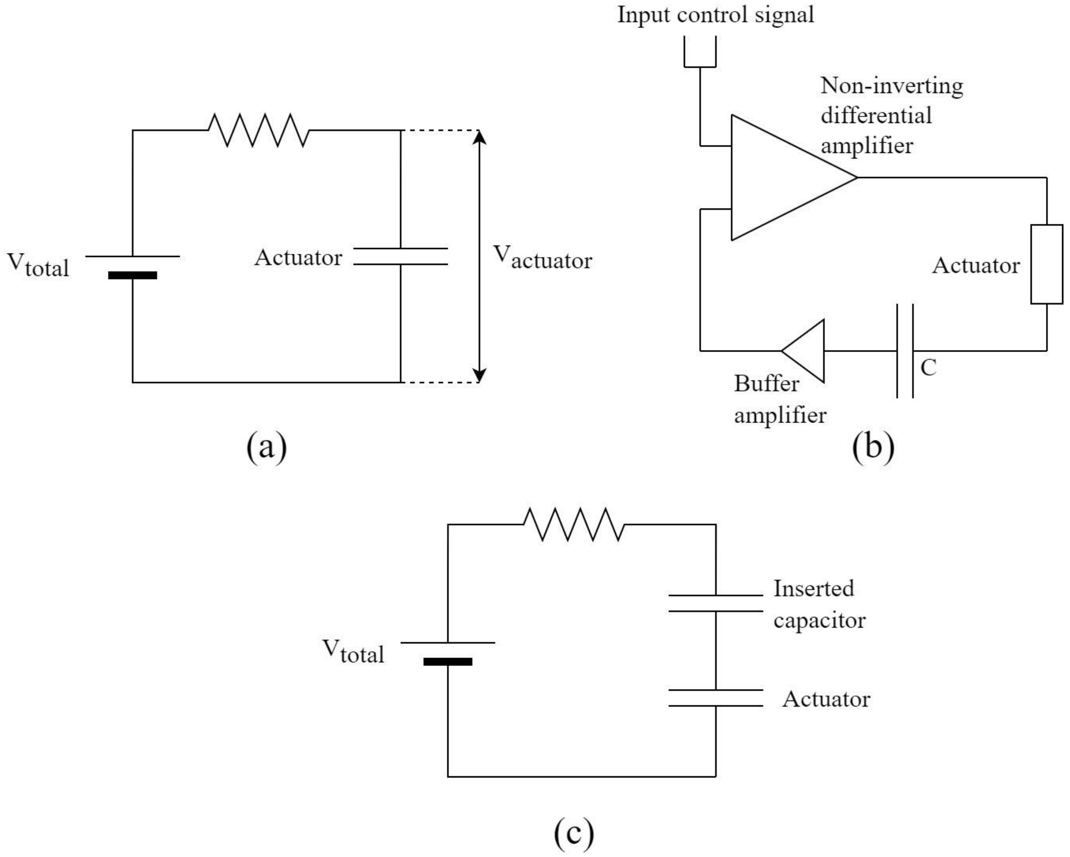

Figure 2.2 Driving methods for Piezoelectric Actuators [27]: (a) voltage driven (b) charge driven, (c) capacitor insertion method.

The advantages and disadvantages of these three driving methods in the literature are summarized in the table below.

Table 2.1 Comparison of Excitation Methods for Piezoelectric Actuators

Parameter / Method	**Voltage Excitation**	**Charge Excitation**	**Capacitor Insertion**
Application	Simple, common, economic	Complicated	Simple
Hysteresis	High	Low	Very Low
Creep	High	High	Low
Available Capacity	Full capacity	Limited capacity	Very low capacity

To sum up, although charge excitation and capacitor insertion method eliminated hysteresis and creep, implementation difficulty and limited capacity are important drawbacks of these methods. In the scope of this work, the voltage excitation method is selected to model the piezoelectric actuator since the disadvantages of the voltage driving method can be eliminated by accurate nonlinear modeling.

2.2.1 Hysteresis

Hysteresis in piezoelectric literature is defined as nonlinearity between input voltage and output displacement, and it is the most prominent nonlinearity present in PSA. Although, the word *“hysteresis”* is originated from ancient Greek which means “lagging behind” or “coming behind” [24], hysteresis in piezoelectricity is different from “phase lag” which exist in many linear systems. Nonlinear relationship between voltage and strain (or displacement) is illustrated in Figure 2.3. At the macroscopic level, hysteresis could be defined as the piezoelectric material's energy loss or power dissipation during expansion or contraction [29].

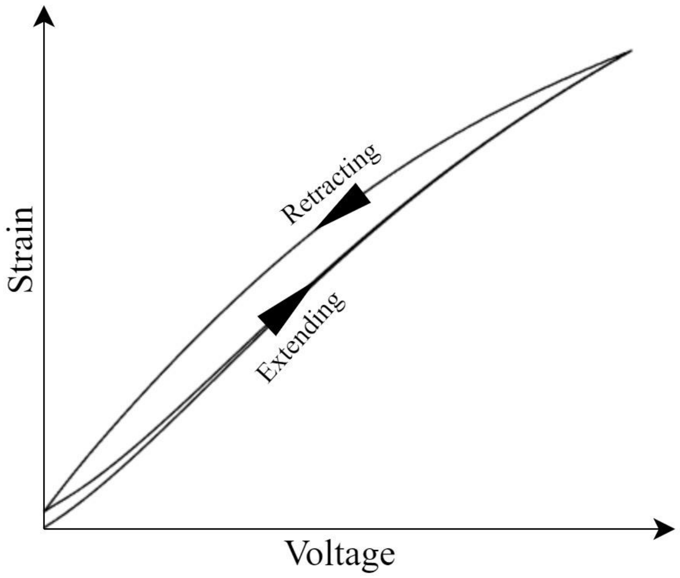

Figure 2.3 Hysteresis Curve

Hysteresis models for piezoelectric actuators may be classified into physics based models and phenomenology based (mathematical) models [30]. Jiles-Atherton model [31] and domain wall model [32] are classified as physics based hysteresis models. Although, the physics based models define the theory of hysteresis phenomena, this methods quite complex to implement due to inherent nature of piezoelectricity [33]. Thus, phenomenology-based models (i.e, mathematical models) are frequently preferred for modeling applications. The phenomenology based models may be divided into two types: differential equation based (dynamic) and operator based (static) [34]. While Prandtle–Ishlinskii [35], Preisach [36] and Krasnoselskii-Pokvrovski [37] models are operator based mathematical models, Duhem [38], Backlash-like [39] and Bouc-Wen [40] models are defined as differential equation based mathematical models. Also, Nero/Fuzzy [41], Polynomial [42] and Ellipse-based [43] models are the other models that define hysteresis.

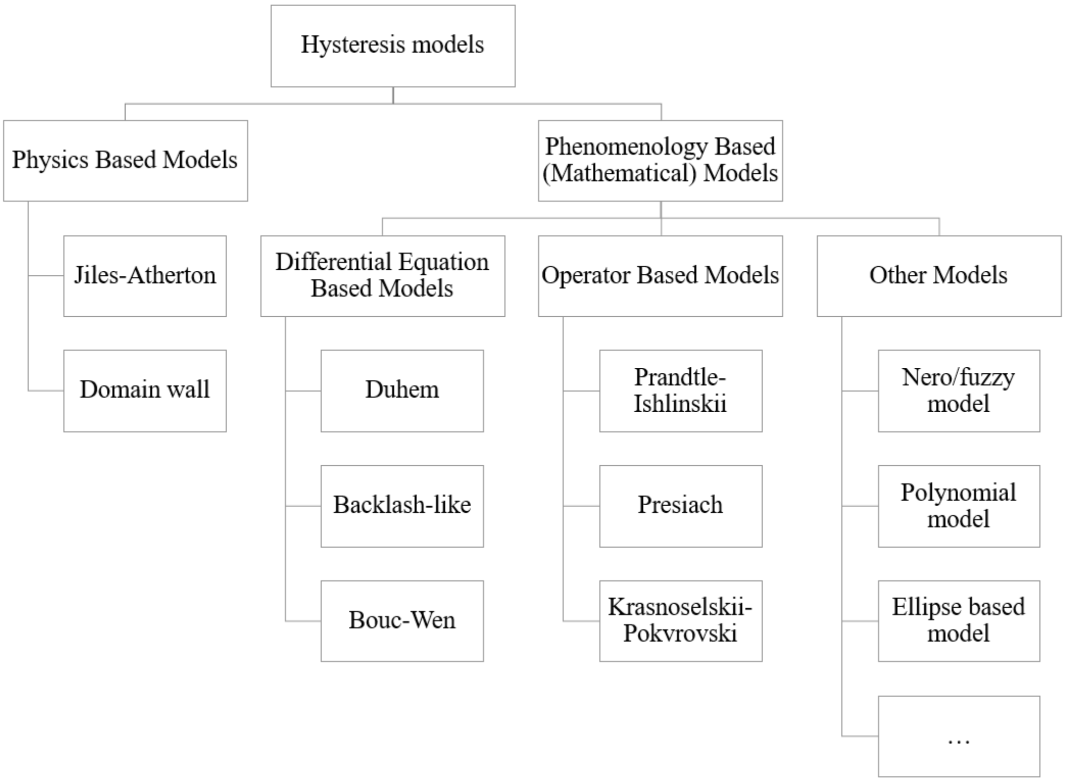

Figure 2.4 Hysteresis models [24], [30], [39], [44]

Another classification can be made according to whether hysteresis depends on input voltage frequency or not. Input frequency independent hysteresis models are classified as rate-independent, while the others are categorized as rate-dependent hysteresis (Figure 2.5).

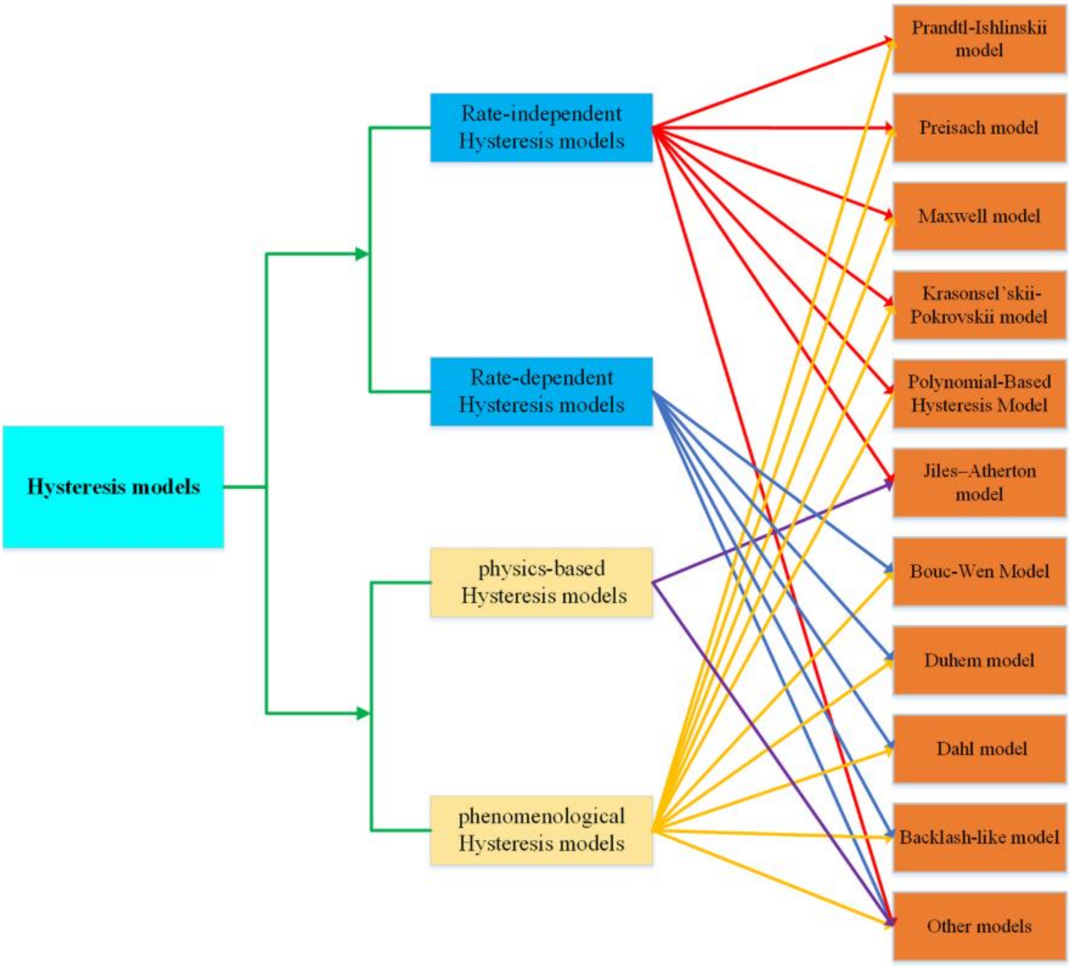

Figure 2.5 Classification of hysteresis models [44]

A method for describing hysteresis was first proposed by Bouc in 1967 [45], then this method was generalized by Wen in 1976 [46]. After that, this method is named as Bouc-Wen model, and it has been widely utilized to simulate hysteretic behavior in various engineering applications [47]. In this study, Bouc-Wen model is chosen for hysteresis modeling thanks to following features:

- ability to capture a wide range of hysteresis curve shapes with high matching quality [48]
- need for only one auxiliary differential equation [49],[50]
- simple parameter identification process [44]

- computational simplicity [51]
- ease of obtaining inverse model for hysteresis compensation [44]
- ease of designing controller [44]

Classical Bouc-Wen model is given in equation (2.2)

$$m\ddot{x} + b\dot{x} + kx = k(du - h) \tag{2.1}$$

$$\dot{h} = \alpha d\dot{u} - \beta|\dot{u}|h|h|^{n-1} - \gamma\dot{u}\ |h|^{n} \tag{2.2}$$

where d (m/V), is the piezoelectric strain constant, u (volts) is the input voltage, and h (m) is the hysteretic state variable. Since n is usually assumed to “1” for ease of computation, equation (2.2) is simplified to:

$$\dot{h} = \alpha d\dot{u} - \beta|\dot{u}|h - \gamma\dot{u}\ |h| \tag{2.3}$$

In piezoelectricity literature, many studies have been carried out to increase accuracy and to extend the application range of Bouc-Wen model by modifying it. In the following paragraph, improvements and modifications made to Bouc-Wen models are described in chronological order.

Firstly, a non-symmetrical B-W is proposed by Zhu and Wang [33], by adding non-symmetrical factor δ. Then, this model was taken one step further with introducing frequency factor τ [52]. Another upgraded model was established by Wan [53]. In this study, a two degree polynomial function is engaged in the linear part (X(t)). Ming [54] obtained Modified B-W model by adding a cubic function dependent on the derivative of the voltage with respect to time. After that, the enhanced B-W model was developed by Gan [55]. In this study, α, β and γ are considered as first order polynomial function of frequency instead of constants to increase rate-independent accuracy of the hysteresis model. Then, Gan [56] proposed another generalized B-W model in order to cover higher frequency input voltages up to 110 Hz. This model is formulated upon integrating relaxation functions $k(u,\dot{u})$ and $\alpha(u,\dot{u})$. It is stated that, when input voltage frequency is very low ($\dot{u} \cong 0$), the values k and α becomes constant, thus the model transforms to classical B-W. More recently, Shao et al. [57] utilize a second order polynomial function as a in the linear part (X(t)), and B-W model is discretized to be employed in discrete control sytems. Finally, a fractional order Bouc-Wen model is developed by Kang et al. [58]. In this model, fractional calculus is utilized to take derivative of auxilary hystresis variable inspired by extensive usage of fractional calculus to describe hystresis loops with rate-dependent characteristics. Equation sets of all Bouc-Wen models are compiled in the table below.

Table 2.2 Equation sets for modified Bouc-Wen models

Model	**Equation Set**
Classical Bouc-Wen	$x = X + h$ $X = du$ $\dot{h} = \alpha d\dot{u} - \beta\lvert\dot{u}\rvert h - \gamma\dot{u}\,\lvert h\rvert$
Non-symmetrical Bouc-Wen [33]	$x = X + h$ $X = du$ $\dot{h} = \alpha d\dot{u} - \beta\lvert\dot{u}\rvert h - \gamma\dot{u}\,\lvert h\rvert + \delta usgn(\dot{u})$
Generalized Non-symmetrical Bouc-Wen [52]	$x = X + h$ $X = \frac{k_1}{\tau}e^{-t/\tau}u + h$ $\dot{h} = \alpha d\dot{u} - \beta\lvert\dot{u}\rvert h - \gamma\dot{u}\,\lvert h\rvert + \delta usgn(\dot{u})$
Asymmetric Bouc-Wen [53]	$x = X + h$ $X = pu^2 + qu$ $\dot{h} = \alpha d\dot{u} - \beta\lvert\dot{u}\rvert h - \gamma\dot{u}\,\lvert h\rvert$

Table 2.2 Equation sets for modified Bouc-Wen models (Cont’d)

Modified Bouc-wen [54]	$x = X + h + \mathrm{p}\dot{u} + q\dot{u}^3$ $X = du$ $\dot{h} = \alpha d\dot{u} - \beta\lvert\dot{u}\rvert h - \gamma\dot{u}\,\lvert h\rvert$
Enhanced Bouc-Wen [55]	$x = X + h$ $X = k(f) * u$ $\dot{h} = \alpha(f)d\dot{u} - \beta(f)\lvert\dot{u}\rvert h - \gamma(f)\dot{u}\,\lvert h\rvert$
Generalized Bouc-Wen [56]	$x = X + h$ $X = k(u,\dot{u}) * u$ $\dot{h} = \alpha(u,\dot{u}).\,d\dot{u} - \beta\lvert\dot{u}\rvert h - \gamma\dot{u}\,\lvert h\rvert$ $k(u,\dot{u}) = pe^{-q\dot{u}}$ $\alpha(u,\dot{u}) = \varepsilon \mathrm{e}^{\delta\lvert\dot{u}\rvert}$
Discrete Bouc-Wen [57]	$x = X + h$ $X = d_1u + d_2u^2$ $\dot{h} = \alpha d\dot{u} - \beta\lvert\dot{u}\rvert h - \gamma\dot{u}\,\lvert h\rvert$
Fractional order Bouc-Wen [58]	$x = X + h$ $X = d_1u + d_2u^2 + d_3u^3$ $\frac{d^{\lambda_2}h}{dt} = \rho\left(\frac{d^{\lambda_1}u}{dt} - \sigma\left\lvert\frac{d^{\lambda_1}u}{dt}\right\rvert h\right.$ $\left. + (\sigma - 1)\frac{d^{\lambda_1}u}{dt}\lvert h\rvert\right)$ $0 < \lambda_{1,2} \leq 1$

2.2.2 Creep

In linear piezoelectricity, it is expected that displacement values remain constant when a step voltage input is applied. However, in reality, a logarithmically decaying increase in movement is observed because of Creep phenomenon. Creep can be described as a slow drift in displacement which results from a sudden change in electric potential. The reason for this phenomenon is that the material continues to draw charges that leads to slow rise in displacement. In open-loop control, ignoring creep effect will cause inaccuracy in the model, especially at low frequencies or steady positioning applications. In addition, the error becomes larger and larger as time goes on.

Two main creep modeling methods take place in classical literature [59]:

1- Logarithmic model
2- Linear time invariant (LTI) model

Logarithmic model defines creep with the following expression in the time domain [60]:

$$L(t) = L_o\left(1 + \gamma \log_{10}\left(\frac{t}{0.1}\right)\right) \tag{2.4}$$

Where L_o is nominal displacement value, γ is the creep factor. The simplicity of this model makes it powerful. Most of the piezoelectric actuator producers express creep behavior of their products with the logarithmic model.

Creep can also be modelled with a series of equivalent springs and dampers in the frequency domain. The expression for this method, named LTI model, is presented in Figure 2.6.

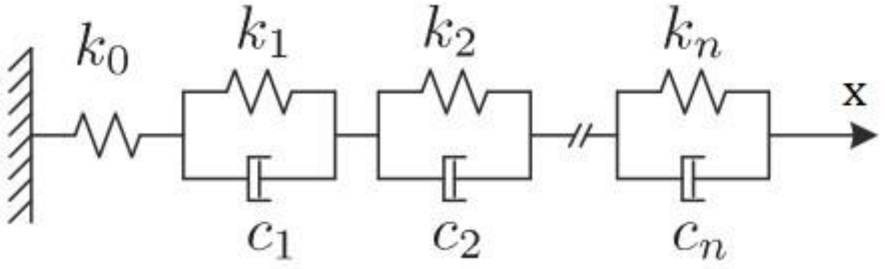

Figure 2.6. Spring-damper creep model [61]

Laplace form of spring-damper creep model is given with below expression [61].

$$G_s(s) = \frac{X(s)}{U(s)} = \frac{1}{K_0} + \sum_{i=1}^{n} \frac{1}{c_i s + k_i} \tag{2.5}$$

Here $X(s), U(s), c_i$ and k_i denotes for displacement, input voltage, spring and damping constants, respectively. It is easy to implement LTI model on linear PEA model, whereas it is difficult to find a large number of parameters for this method [59].

Beside phenomenology based classical creep models, a physics-based new approach for describing creep is proposed by Liu [61], named fractional order creep model. Piezoelectric materials, more generally dielectric materials, are neither pure resistors nor pure capacitances; these materials behave as resistocapacitance [62]. In Laplace domain, the model is expressed as [59]:

$$G_c(s) = K_c \left(\frac{1}{s}\right)^{\mu} \tag{2.6}$$

where μ stands for the order of the creep, while $\mu = 0$ means ideal resistor, $\mu = 1$ represents ideal capacitor. The value of μ also describes the rate of creep. As μ increase, creep motion becomes faster [61].

2.3 Amplifier Mechanisms

Piezoelectric stack actuators are generally used with integrated amplifier mechanisms because of their inherent low displacement characteristics. Traditional mechanisms with assembled rigid links, gears, and joints cannot be utilized in precise positioning and control due to their coarse resolution and lack of precision brought on by friction and backlash [63]. That’s why, compliant mechanisms produced as single piece (monolithic) are generally preferred since they have no backlash and friction, and motion occurs with smooth elastic deformations. Compliant amplifier mechanisms or i.e. flexure-based displacement amplification mechanisms (FDAMs) steadily gain importance in the field of precision engineering owing to their feasibility and performance [64]. There are various types of FDAM, and nine of them are visualized in Figure 2.7.

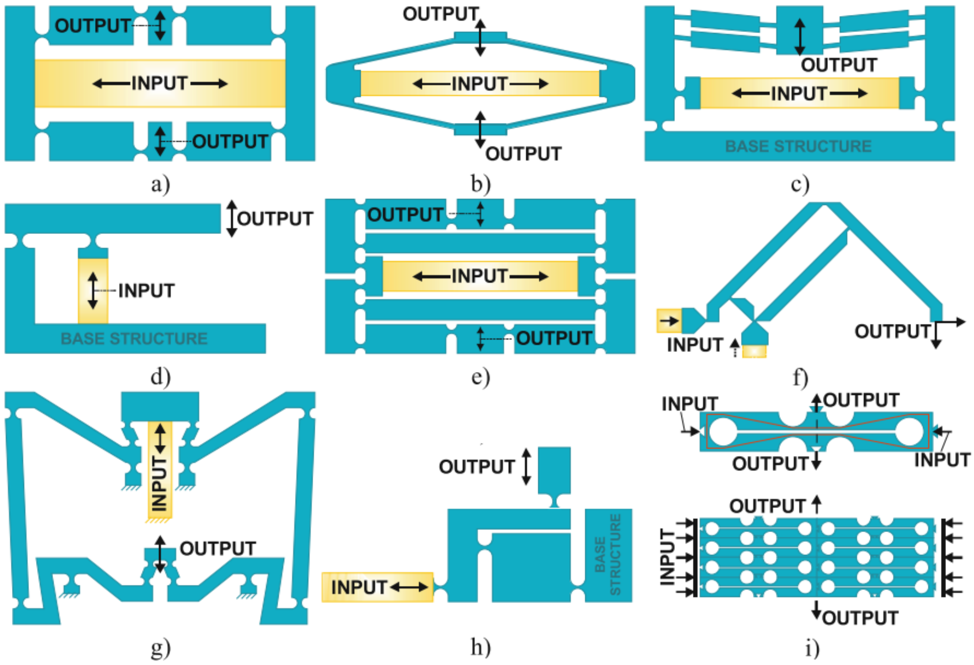

Figure 2.7 FDAMs [65]. (a) bridge type, (b) Rhombus type, (c) symmetric five bar structure, (d) lever mechanism, (e) bridge-lever-type amplifier, (f) pantograph mechanism, (g) tensural displacement amplifier, (h) Scott-Russell mechanism, (i) Re-entrant hexagonal honeycomb

The table below summarizes the advantages and disadvantages of the mechanisms shown in Figure 2.7. Also, amplification ratios, which are equal to output displacement divided by input displacement, is listed below.

Table 2.3 Comparison of different types of amplifier mechanisms

Type of Amplifier Mechanism	Amplification Ratio (R_{amp})	Geometric Compactness	Geometric Simplicity	Flexural Hinges
Bridge-type [66]	<15	+	+	Yes
Rhombus-type [67]	<10	+	++	No
Symmetric Five Bar Structure[65]	~24	+	0	Yes
Lever Mechanism [66], [68]	<10	0	+	Yes
Bridge Lever Type Amplifier [66]	<49	+	-	Yes
Pantograph Mechanism [65]	~6	-	-	Yes
Tensural Displacement Amplifier [69]	~40	-	-	Yes
Scott-Russel Mechanism [70]	~31	0	-	Yes
Re-entrant Hexagonal Honeycomb[71]	~40	0	-	Yes

(++): Best, (+): Good, (0): Average, (-): Bad

As seen from the table above, very high amplification rates could be achieved with lever-type mechanisms, but the most important handicaps of these mechanisms are that they occupy a lot of space. On the other hand, compact mechanisms like, bridge, bridge-lever and symmetric five bar have flexural hinge which leads stress concentration and dramatic decrease in mechanical efficiency. For the reasons described above, a rhombus-type (or rhombic) amplifier mechanism (RTAM) is selected for this thesis study. Even though low amplification ratio compared to other type of mechanisms is an important drawback, its compact, simple and symmetrical geometry is the major advantage. Furthermore, Rhombus amplifier translates motion via slim flexible arms which means RTAM does not have flexure hinges which causes stress concentration. In the following paragraphs, the literature on rhombus amplifier mechanism is reviewed.

In literature, there is an effort to derive an analytical formula. Some of them are derived only by considering geometry, like in the studies of Lobontiu & Garcia [84], Chen [72], Qi [86] and Zhou [69], while the formulas in the articles of Ma [85], Shao [63] Ling [68] and Cao [71] is based on elastic beam theory and energy conservation laws. In general, elasticity formulas give better results since elastic losses on the arms are taken into account. Comparison of accuracy of amplification ratio formulas is presented with Table 5.10 in Case Study IV.

In the articles reviewed above, RTAM serves as an actuator in several applications including jet dispenser, micro-pump, flow control valve, precision positioning stage and antenna orientation stage. RTAM's are generally manufactured by wire cutting (EDM) method. General topology of RTAM is illustrated by Figure 2.8.

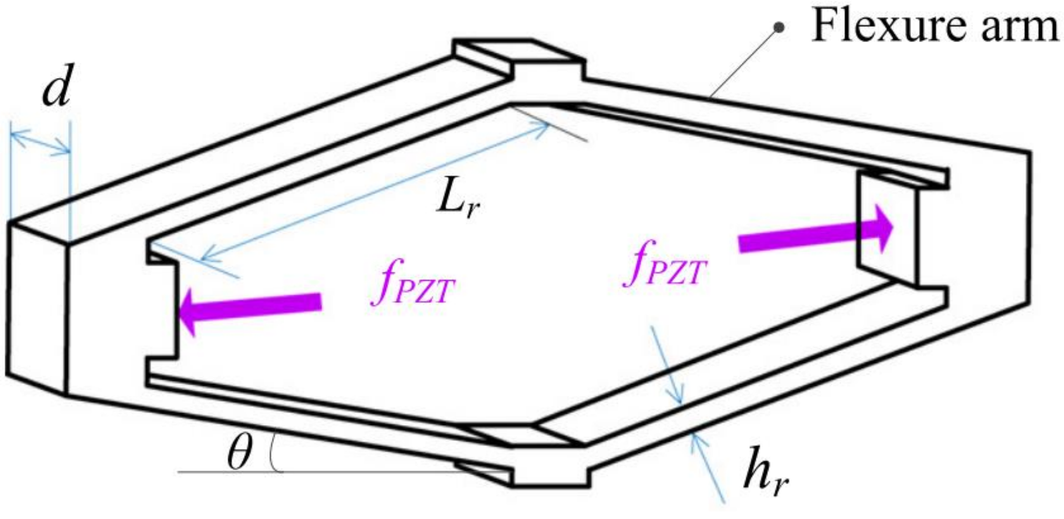

Figure 2.8 Topology of rhombus type mechanism [72]

Based on the output displacement results of Chen [73] as demonstrated in Figure 2.9, it was found that there exist a strong dependence on mechanism angle (θ), a moderate dependence of thickness of flexible arms, and a very weak dependence on radius at the beginning of the flexible arms and width of the mechanism. Sensitivity analysis done by Lu [74] also confirms the dominance of parameters θ and thickness.

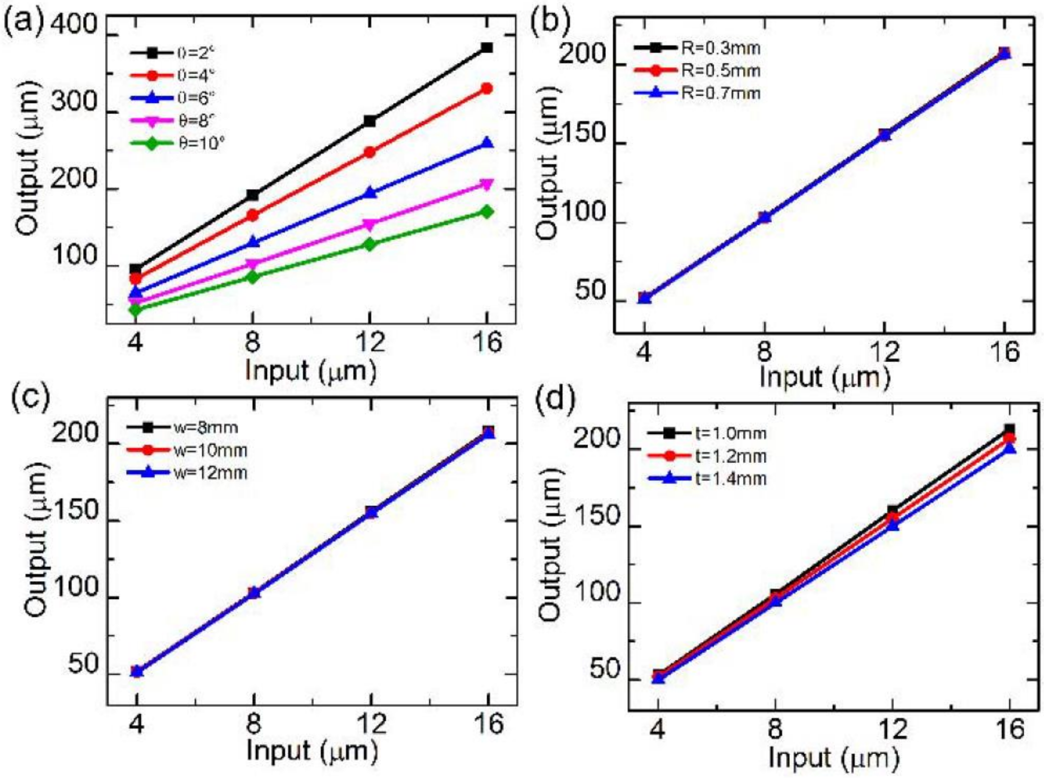

Figure 2.9 Mechanism structure parameters effects on the displacement [73]. (a) θ, (b) Radius, (c) width, (d) thickness.

The visuals of the RTAMs mentioned in the above articles are combined and presented in the figure below.

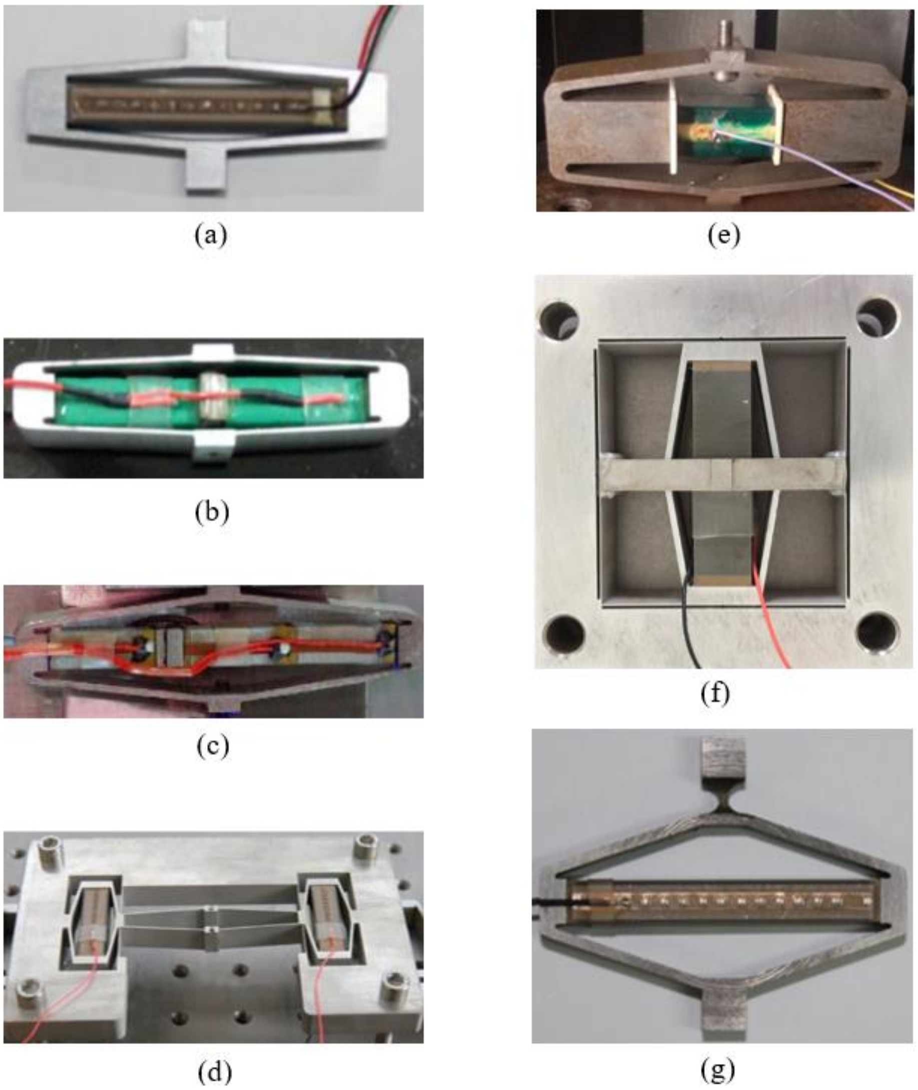

Figure 2.10 Rhombic type amplifier mechanisms: (a) Shao [75], (b) Ling [72], (c) Zhou [73], d) Chen [76] (e) Diao [77], (f) Ling [78], (g) Chen [79]

CHAPTER 3

MODELING OF PIEZOELECTRIC MATERIALS

3.1 Constitutive Equations

Piezoelectric materials are transversely isotropic materials which means symmetricity in one direction that is normal to a plane of isotropy (xy-plane). Therefore, piezoelectric material shows symmetry about the z-axis which is the poling direction [80]. Constitutive equations of piezoelectric material in strain-charge form are defined in ANSI/IEEE 176 standard [81], and these equations can be written with tensorial notation as follows:

$$S_{ij} = s^{E}_{ijkl} T_{kl} + d_{kij} E_k \tag{3.1}$$

$$D_i = d_{ikl} T_{kl} + \varepsilon^{T}_{ik} E_k \tag{3.2}$$

These equations can be also written in stress charge form as follows:

$$T_{ij} = c^{E}_{ijkl} S_{kl} - e_{kij} E_k \tag{3.3}$$

$$D_i = e_{ikl} S_{kl} + \varepsilon^{T}_{ik} E_k \tag{3.4}$$

The terms in these equations are described as [81]:

{S}: Mechanical strain vector (mm/mm)

{T}: Stress vector (N/mm^2)

{D}: Electrical displacement vector (C/mm^2)

{E}: Electrical field intensity vector (V/mm)

[s^E]: Compliance matrix at constant electrical field (mm^2/N)

[d]: Piezoelectric constant matrix for strain-charge form (mm/V)

[e]: Piezoelectric constant matrix for stress-charge form (C/mm^2)

[ε^T]: Dielectric permittivity matrix at constant stress (F/mmm)

[c^E]: Elasticity matrix at constant electrical field (N/mm^2)

The superscripts t denotes the transpose operation, while the superscripts E and T represents that corresponding constants are evaluated at constant electrical field and constant stress, respectively. Equations (3.1) and (3.2) are also can be coupled in compressed matrix form (i.e, Voight notation) as follows:

$$\begin{bmatrix} S \\ D \end{bmatrix} = \begin{bmatrix} s^E & d^t \\ d & \varepsilon^T \end{bmatrix} = \begin{bmatrix} T \\ E \end{bmatrix} \tag{3.5}$$

Open form of equation (3.5) is given with equation (3.6).

$$\begin{bmatrix} S_1 \\ S_2 \\ S_3 \\ S_4 \\ S_5 \\ S_6 \\ D_1 \\ D_2 \\ D_3 \end{bmatrix} = \begin{bmatrix} s_{11}^E & s_{12}^E & s_{13}^E & 0 & 0 & 0 & 0 & 0 & d_{31} \\ s_{12}^E & s_{22}^E & s_{13}^E & 0 & 0 & 0 & 0 & 0 & d_{31} \\ s_{13}^E & s_{13}^E & s_{33}^E & 0 & 0 & 0 & 0 & 0 & d_{33} \\ 0 & 0 & 0 & s_{55}^E & 0 & 0 & 0 & d_{15} & 0 \\ 0 & 0 & 0 & 0 & s_{55}^E & 0 & d_{15} & 0 & 0 \\ 0 & 0 & 0 & 0 & 0 & s_{66}^E & 0 & 0 & 0 \\ 0 & 0 & 0 & 0 & d_{15} & 0 & \varepsilon_{11}^T & 0 & 0 \\ 0 & 0 & 0 & d_{15} & 0 & 0 & 0 & \varepsilon_{11}^T & 0 \\ d_{31} & d_{31} & d_{33} & 0 & 0 & 0 & 0 & 0 & \varepsilon_{33}^T \end{bmatrix} = \begin{bmatrix} T_1 \\ T_2 \\ T_3 \\ T_4 \\ T_5 \\ T_6 \\ E_1 \\ E_2 \\ E_3 \end{bmatrix} \tag{3.6}$$

3.2 Linear Modeling

3.2.1 Linear Modeling of PSA

As described in equation (3.6) d_{31} (plane mode), d_{33} (thickness mode), and d_{15} (shear mode) are the three modes of actuation. In PSAs, d_{33} is the most important mode. Since PSA have multiple layers as shown in Figure 3.1, total displacement could be formulated as:

$$\Delta L = d_{33}\, n\, \emptyset \tag{3.7}$$

where n is the number of layers, and $\emptyset$ is the applied voltage. In this model, linear relation between voltage and displacement could be observed, since parameters “d_{33}” and “n” are constants.

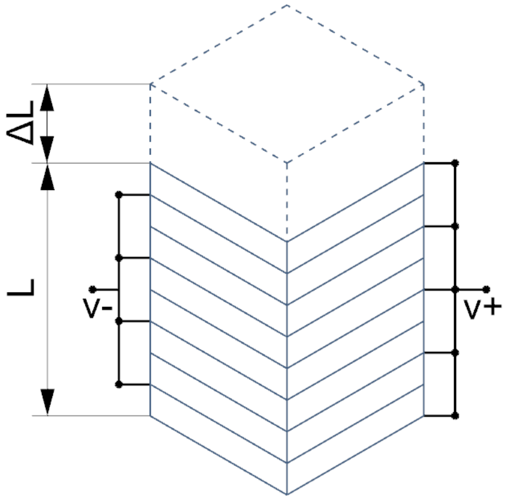

Figure 3.1 Schematic of multilayer PSA

When PSA’s are modelled main interest generally strain at z-direction generally. That’s why, following equation could be extracted from equation (3.6)

$$S_{33} = S_{31}T_1 + S_{32}T_2 + S_{33}T_3 + d_{33}E_3 \tag{3.8}$$

In modeling PSA’s, there is no stress along the planes xz and yz which means $T_1 = T_2 = 0$, strain at zz direction could be further reduced to:

$$S_{33} = S_{31}T_1 + d_{33}E_3 \tag{3.9}$$

PSAs are usually used with constant or varying load on top of them. Constant load on PSA causes linear shift on strain curve as shown in Figure 3.2. The amount of shift (ΔL_{pl}) can be calculated simply with below formula where F_{cl} is the constant load on piezo, k_{piezo} is the stiffness value.

$$S_{cl} = \frac{F_{cl}}{k_{piezo}} \tag{3.10}$$

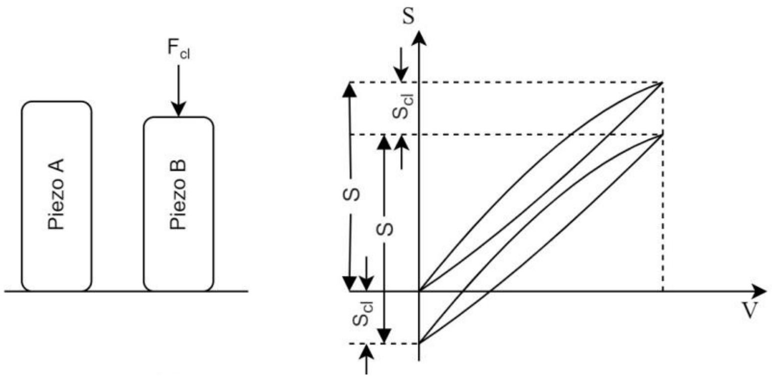

Figure 3.2 Free strain curve vs constant load strain curve

When PSA is subjected to variable load, its strain curve deviates as shown in Figure 3.3. New strain value (S_{vl}), could be obtained via eqn. (3.11).

$$S_{vl} = \frac{k_{vl}}{k_{piezo} + k_{vl}} S \tag{3.11}$$

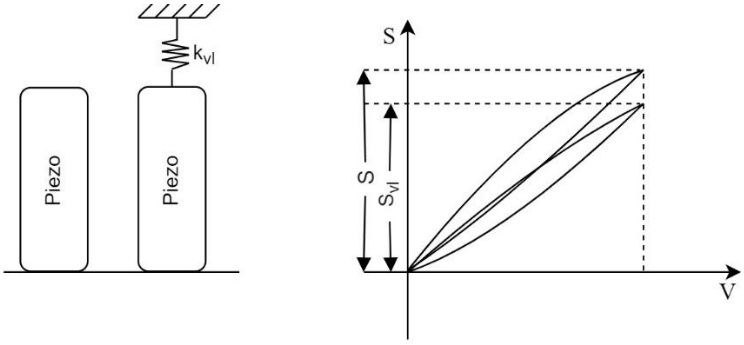

Figure 3.3 Free strain curve vs variable load strain curve

In real engineering applications, neither constant load nor variable load situation is fully correct. In these applications like mechanical amplifier mechanisms, combined load as shown in Figure 3.4 is the case. In rhombus-type mechanisms, Mechanism stiffness along piezo z-axis direction is the variable load, while preload is the constant load. However, since mechanical amplifier mechanism acts as soft spring compared to piezo stiffness, preload on PSA could be considered as constant load, so it can be assumed as both combined load and constant load cases when designing an amplification mechanism.

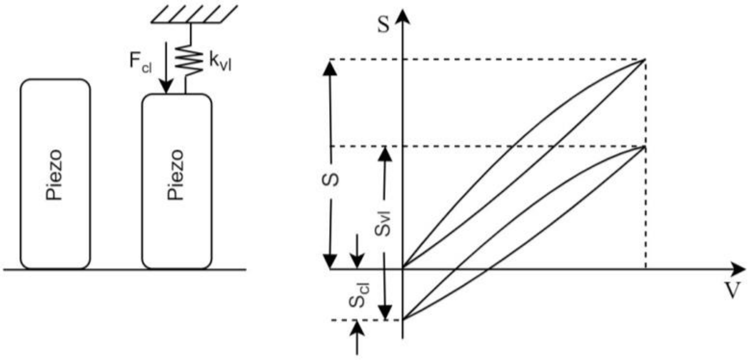

Figure 3.4 Free strain curve vs combine load strain curve

Figure 3.5 shows the linear relation with displacement and generated force of a PSA. The actuator can achieve its maximum displacement value (ΔL_{max}), only when there is no load on it. Besides, when the displacement is restricted totally, and maximum voltage is applied at the same time, the actuator reaches its maximum force capacity, and this maximum generated force is termed as blocking force.

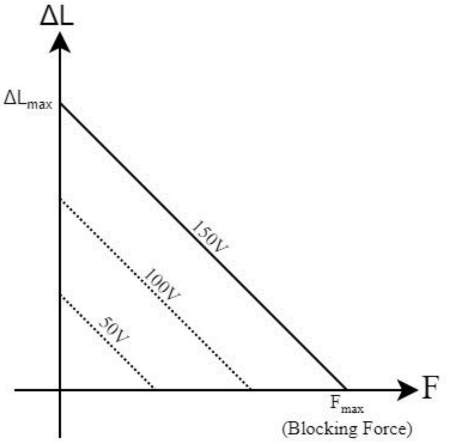

Figure 3.5 Displacement vs generated force lines with different voltage levels

3.2.2 Linear Modeling of RTAM

In flexure-based displacement amplification mechanisms, the mechanism's geometric nonlinearity could be considered negligible since the geometric nonlinearity error is quite minor compared error caused by hysteresis [82]. RTAM coordinates are described in Figure 3.6. This coordinate axis is used for both COMSOL analyses and hand calculations.

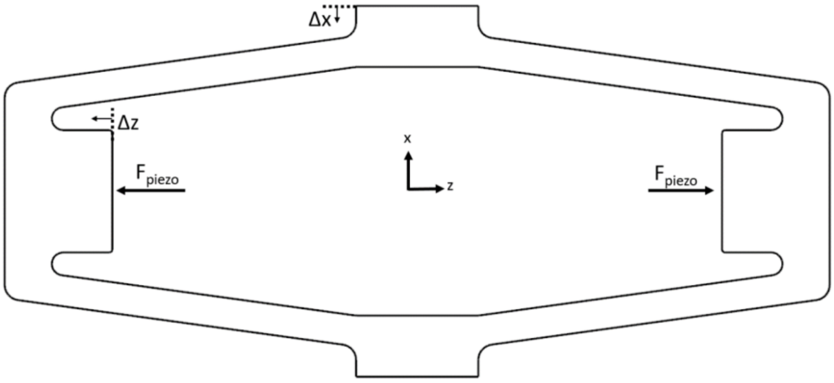

Figure 3.6 Rhombus-type amplifier mechanism coordinate definitions

In rhombus-type amplifier mechanism, elongation on PSA can be found with lateral stiffness (k_{33}) of amplifier mechanism. As illustrated in Figure 3.7, piezo displacement (Δz) in a RTAM, can be found with junction point between RTAM lateral stiffness line and displacement-force line of PSA. Lateral stifness (k_{33}) and longitiduional stifness (k_{31}) values of RTAM is shown in below equations, respectively:

$$k_{33} = \frac{F_{piezo}}{\Delta z} \tag{3.12}$$

$$k_{31} = \frac{F_{piezo}}{\Delta x} \tag{3.13}$$

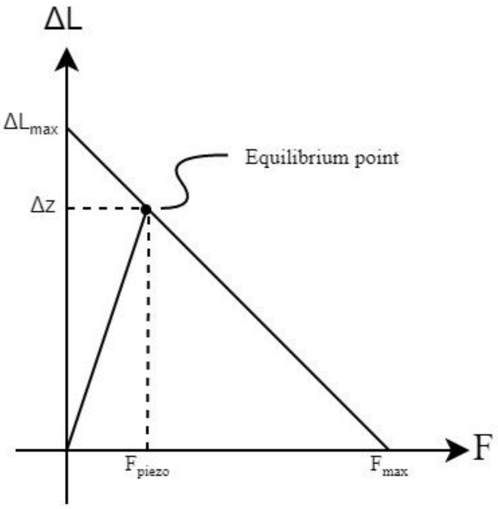

Figure 3.7 Equilibrium point of RTAM

Another critical design parameter of RTAM is the amplification ratio, which is defined in (3.14) and Figure 3.8. Comparison of different R_{amp} formulations is presented in Case Study IV.

$$R_{amp} = \frac{\Delta x}{\Delta z} \tag{3.14}$$

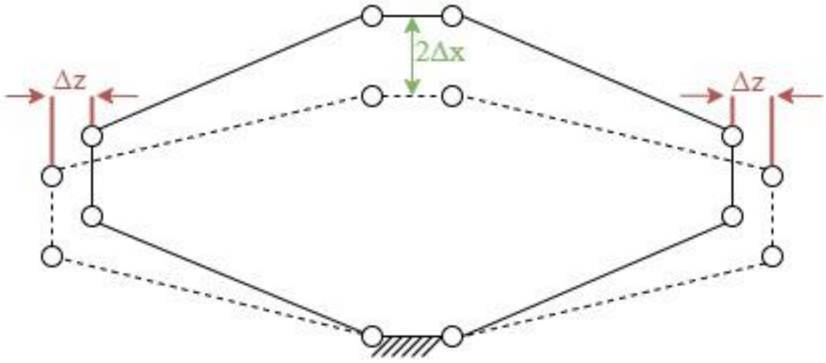

Figure 3.8 RTAM amplification ratio (R_{amp}) definition

when trying to increase the amplification ratio, it should be noted that there is a trade-off between stroke and dynamic frequency [78], [76]. To solve this optimization problem, a mechanical efficiency is used. In order to measure how effectively motion is transmitted, the following efficiency formula [83] could be utilized

$$\eta = \frac{F_{RTAM} * \delta_{RTAM}}{F_p * \delta_P} \tag{3.15}$$

where F_{RTAM} and δ_{RTAM} is blocking force and maximum displacement of RTAM respectively, while F_p and δ_P blocking force and maximum displacement of PSA.

3.3 Variational Method

In continuum mechanics, the piezoelectric dynamic equations are derived with Hamilton’s principle by adapting Lagrangian and virtual work in coupled electrical and mechanical domain [84]. The Lagrangian $\mathcal{L}$ of a bounded piezoelectric volume V is defined by summation of kinetic energy J and potential energy H in equation (3.16) by Tzou [85].

$$\mathcal{L} = \int_V (J - H) dV = \int_V \left[\frac{1}{2} \rho \{\dot{u}\}^T \{\dot{u}\} - \frac{1}{2} [\{S\}^T \{T\} - \{E\}^T \{D\}] \right] dV \tag{3.16}$$

where $\{\dot{u}\}$ velocity (time derivative of displacement u) field and ρ is the mass density. The virtual work done by both mechanical and electrical forces (electrical charges) is given with equation (3.17), where δ is variation operator, and it vanishes at the boundary where essential (dirichlet) boundary conditions are prescribed.

$$\delta\mathcal{W} = \int_V \{\delta u\}^T\{F_V\}dV + \int_{\Omega_1} \{\delta u\}^T\{F_\Omega\}d\Omega + \{\delta u\}^T\{F_\mathrm{p}\} \\ - \int_{\Omega_2} \delta\phi\varrho d\Omega - \delta\phi Q = 0 \tag{3.17}$$

where:

$\{F_V\}$: Body forces

$\{F_\Omega\}$: Surface forces on Ω_1

$\{F_P\}$: Point loads

ϕ: Electric potential

ϱ: Surface charge brought on Ω_2

Q: Applied electric charges

Ω_1: surface where traction is prescribed

Ω_2: surface where charge is prescribed

Using the definitions above, the dynamic equation of piezoelectric structure is as follows:

$$\int_V \delta(\mathcal{L} + \mathcal{W})dt = 0 \tag{3.18}$$

where $\mathcal{L}$ is denoted for Lagrangian, and W is for virtual work of both mechanical and electrical external forces. By substituting equations (3.16) and (3.17) into (3.18), Equation (3.19) is obtained which will be used as the main equation to derive FEM in the next section.

$$
\begin{aligned}
-\int_{V} \Big[\rho\{\delta u\}^{T}\{\ddot{u}\} - \{\delta S\}^{T}[c^{E}]\{S\} + \{\delta S\}^{T}[e]^{T}\{E\} + \{\delta E\}^{T}[e]\{S\} \\
+ \{\delta E\}^{T}[\varepsilon^{S}]\{E\} + +\{\delta u\}^{T}[F_{V}]\Big]\, dV \\
+ \int_{\Omega_1} \{\delta u\}^{T}\{F_{\Omega}\} d\Omega + \{\delta u\}^{T}\{F_{\mathrm{p}}\} - \int_{\Omega_2} \delta\phi \varrho d\Omega - \delta\phi Q \\
= 0
\end{aligned}
\tag{3.19}
$$

The table below illustrates an electromechanical analogy to understand coupling between electrical and mechanical domains. A significant note is that all electrical variables are one tensorial rank lower than mechanical ones.

Table 3.1 Electromechanical Analogy [21]

Mechanical Quantities	**Electrical Quantities**
$\{F\}$: Force (vector)	ϱ: Charge (scalar)
$\{u\}$: Displacement (vector)	ϕ: Voltage (scalar)
$\{T\}$: Stress (2nd order tensor)	$\{D\}$: Electric Displacement (vector)
$\{S\}$: Force (2nd order tensor)	$\{E\}$: Electric Field (vector)

3.4 Finite Element Methodology

In structural problems, the finite element method is formulated using the weak form of the problem. Boundary conditions and governing equations of physical systems constitute the strong form, while the integral form of these equations is named the weak form [86]. The general methodology for a structural problem is presented in

Figure 3.9. Firstly, partial differential equations (strong form) of modeled geometry is derived. Then, these equation(s) is converted to the weak form. Finally, discrete equations are constructed to be solved with appropriate approximation functions (e.g., shape functions).

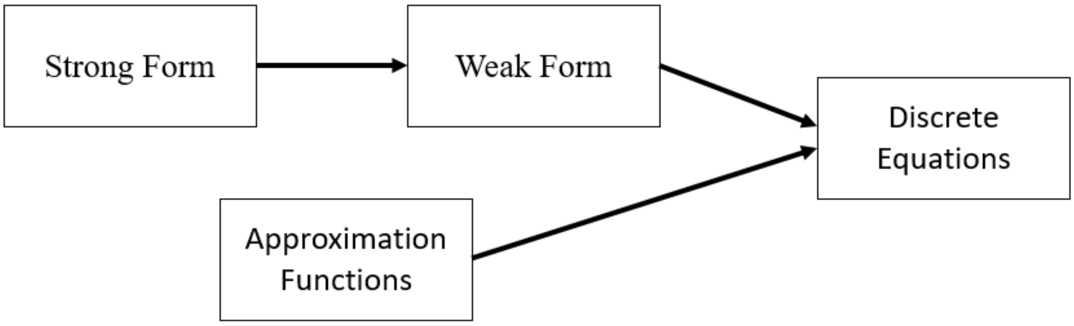

Figure 3.9. Sequence for the development of FEM [86]

Within this thesis's scope, the weak piezoelectric continuum form is derived with Hamilton Principle in section 3.3. The final form of the equation is compiled in (3.19). By using this equation, finite element discrete equations are formed as follows [84]:

The displacement {u} and electric potential $\{\phi\}$ are presented below in terms of corresponding shape functions.

$$\{u\} = [N_u]\{u_i\} \tag{3.20}$$

$$\{\phi\} = [N_\phi]\{\phi_i\} \tag{3.21}$$

Derivation operator $[\mathcal{D}]$ and gradient operator ∇ are defined as:

$$[\mathcal{D}] = \begin{bmatrix} \partial_x & 0 & 0 \\ 0 & \partial_y & 0 \\ 0 & 0 & \partial_z \\ 0 & \partial_z & \partial_x \\ \partial_z & 0 & \partial_x \\ \partial_y & \partial_x & 0 \end{bmatrix} \tag{3.22}$$

$$\nabla = \begin{bmatrix} \partial_x \\ \partial_y \\ \partial_z \end{bmatrix} \tag{3.23}$$

An important intermediate matrix is shape function derivative. B_u represents shape function derivative for displacement field, while B_ϕ stands for electric potential.

$$[B_u] = [\mathcal{D}][N_u] \tag{3.24}$$

$$[B_\phi] = \nabla\left[N_\phi\right] \tag{3.25}$$

By using definitions above, strains {S} and electric field vector {E} could be written as [87]:

$$\{S\} = [B_u]\{u_i\} = [\mathcal{D}][N_u]\{u_i\} \tag{3.26}$$

$$\{E\} = -[B_\phi]\{\phi_i\} = -\nabla\left[N_\phi\right]\{\phi_i\} \tag{3.27}$$

Substituting above expressions (3.20), (3.21), (3.26) and (3.27) in equation (3.19) leads to:

$$
\begin{aligned}
-\{\delta u_i\}^T \int_V \rho[N_u]^T[N_u]dV\,\{\ddot{u}_i\} - \{\delta u_i\}^T \int_V [B_u]^T[c^E][B_u]dV\,\{u_i\} \\
- \{\delta u_i\}^T \int_V [B_u]^T[e]\big[B_\phi\big]dV\,\{\phi_i\} \\
- \{\delta\phi_i\}^T \int_V [B_\phi]^T[e]^T[B_u]dV\{u_i\} \\
+ \{\delta\phi_i\}^T \int_V [B_\phi]^T[\varepsilon^S]\big[B_\phi\big]dV\{\phi_i\} \\
+ \{\delta u_i\}^T \int_V [N_u]^T\{F_V\}dV \\
+ \{\delta u_i\}^T \int_{\Omega_1} [N_u]^T\{F_\Omega\}d\Omega + \{\delta u_i\}^T[N_u]^T\{F_P\} \\
- \{\delta\phi_i\}^T \int_{\Omega_2} [N_\phi]^T\varrho d\Omega - \{\delta\phi_i\}^T[N_\phi]^T Q = 0
\end{aligned}
\tag{3.28}
$$

Expression (3.28) can be divided into two parts by separating $\{\delta u_i\}^T$ and $\{\delta\phi_i\}^T$ terms.

$$
\begin{aligned}
\{\delta u_i\}^T \bigg[\int_V \rho[N_u]^T[N_u]dV\,\{\ddot{u}_i\} + \int_V [B_u]^T[c^E][B_u]dV\,\{u_i\} \\
- \int_V [B_u]^T[e]\big[B_\phi\big]dV\,\{\phi_i\}\bigg] \\
= \{\delta u_i\}^T \bigg[\int_V [N_u]^T\{F_V\}dV \int_{\Omega_1} [N_u]^T\{F_\Omega\}d\Omega \\
+ [N_u]^T\{F_P\}\bigg]
\end{aligned}
\tag{3.29}
$$

$$
\begin{aligned}
\{\delta\phi_i\}^T \bigg[\int_V [B_\phi]^T[e]^T[B_u]dV\{u_i\} + \int_V [B_\phi]^T[\varepsilon^S]\big[B_\phi\big]dV\{\phi_i\}\bigg] \\
= \{\delta\phi_i\}^T \bigg[\int_{\Omega_2} [N_\phi]^T\varrho d\Omega - [N_\phi]^T Q\bigg]
\end{aligned}
\tag{3.30}
$$

By reducing $\{\delta u_i\}^T$ and $\{\delta\phi_i\}^T$ terms and arranging above expressions in more familiar form results in the following expressions:

$$[M]\{\ddot{u}_i\} + [K_{uu}]\{u_i\} + [K_{u\phi}]\{\phi_i\} = \{f_i\} \tag{3.31}$$

$$[K_{\phi u}]\{u_i\} + [K_{\phi\phi}]\{\phi_i\} = \{g_i\} \tag{3.32}$$

Expressions for mechanical force field $\{f_i\}$ and electrical charge field is presented below.

$$\{f_i\} = \int_V [N_u]^T\{F_V\}dV \int_{\Omega_1} [N_u]^T\{F_\Omega\}d\Omega + [N_u]^T\{F_P\} \tag{3.33}$$

$$\{g_i\} = \int_{\Omega_2} [N_\phi]^T\varrho d\Omega - [N_\phi]^T Q \tag{3.34}$$

where $\{F_V\}$, $\{F_\Omega\}$, $\{F_P\}$, ϱ and Q are body forces, surface forces, point force, surface charge density and total electrical charge, respectively. From equation (3.35) to (3.38), mass, stiffness, piezoelectric coupling and capacitance matrices are compiled.

$$[M] = \int_V \rho[N_u]^T[N_u]dV \tag{3.35}$$

$$[K_{uu}] = \int_V [B_u]^T[c^E][B_u]dV \tag{3.36}$$

$$\left[K_{u\phi}\right] = \int_V [B_u]^T[e]\left[B_\phi\right]dV \tag{3.37}$$

$$[K_{\phi\phi}] = \int_V [B_\phi]^T[\varepsilon^S]\left[B_\phi\right]dV \tag{3.38}$$

$$[K_{\phi u}] = [K_{u\phi}]^T \tag{3.39}$$

3.5 PSA Modeling with COMSOL

In this thesis, the structural mechanics module of COMSOL Multiphysics 5.5 (referred to as COMSOL) is utilized to model piezoelectricity and to perform FE analysis and simulations. Because a complete description of COMSOL would be impractical and unnecessary in the scope of this thesis, only important features and key aspects of COMSOL are mentioned in this section.

As shown as Figure 3.10, Definitions, geometry, materials, solid mechanics, electrostatics, mesh, study and results are the main branches for setting up a model in COMSOL [88].

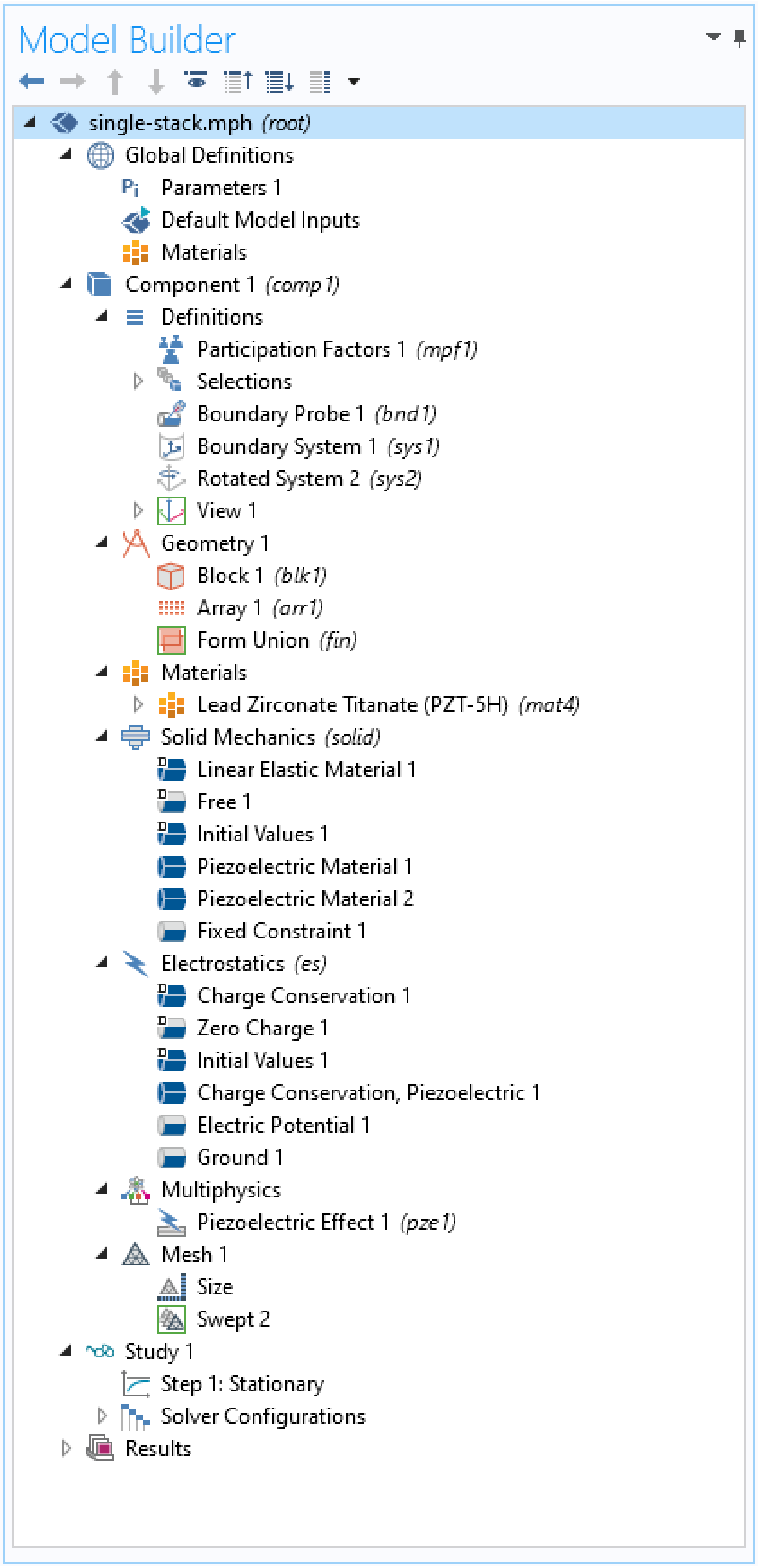

Model Builder

- single-stack.mph *(root)*
  - Global Definitions
    - Parameters 1
    - Default Model Inputs
    - Materials
  - Component 1 *(comp1)*
    - Definitions
      - Participation Factors 1 *(mpf1)*
      - Selections
      - Boundary Probe 1 *(bnd1)*
      - Boundary System 1 *(sys1)*
      - Rotated System 2 *(sys2)*
      - View 1
    - Geometry 1
      - Block 1 *(blk1)*
      - Array 1 *(arr1)*
      - Form Union *(fin)*
    - Materials
      - Lead Zirconate Titanate (PZT-5H) *(mat4)*
    - Solid Mechanics *(solid)*
      - Linear Elastic Material 1
      - Free 1
      - Initial Values 1
      - Piezoelectric Material 1
      - Piezoelectric Material 2
      - Fixed Constraint 1
    - Electrostatics *(es)*
      - Charge Conservation 1
      - Zero Charge 1
      - Initial Values 1
      - Charge Conservation, Piezoelectric 1
      - Electric Potential 1
      - Ground 1
    - Multiphysics
      - Piezoelectric Effect 1 *(pze1)*
    - Mesh 1
      - Size
      - Swept 2
  - Study 1
    - Step 1: Stationary
    - Solver Configurations
  - Results

Figure 3.10 Model tree of COMSOL

Definitions Branch: Because piezoelectric material model is anisotropic, it is important to select anisotropy direction. In COMSOL default settings, +Z direction is defined as poling direction. If poling direction is different in the model geometry, it should be arranged as rotated system in the definitions branch. Also, a probe should be added to a point, edge or boundary where measurement will be taken.

Materials Branch: COMSOL has an extensive pre-defined material collection, including piezoelectric materials in its embedded library.

Solid Mechanics Branch: Piezoelectricity is a coupled problem in mechanical and electrical domains, and this is the section where linear elastic and piezoelectric material is selected. Mechanical boundary conditions also are applied in this section.

Electrostatics Branch: Electrical boundary conditions like electric potential, ground and zero charge are applied in this branch.

Meshing: For Case Study I, a simple 8-noded brick element with linear shape function is used. For IV, brick elements generated by sweeping quadrilateral elements with quadratic shape functions is utilized, while tetrahedral elements is used for remaining parts.

Studies and Solvers: COMSOL has several prepared studies like stationary, frequency domain, time dependent and eigenfrequency. In the scope of the thesis, stationary and eigenfrequency studies are used. As solver The MUMPS (MUltifrontal Massively Parallel sparse direct Solver) is selected. The MUMPS gives solutions of large linear systems in the form of Ax=b [89]

As previously shown in Figure 1.7 and Figure 3.1, PSA consist of multiple thin layers which electric potential and grounding is applied on each layer separately. Since meshing these thin layers would be cumbersome, modeling PSA as a single layer (Figure 3.11c) is a practical solution to this problem. In this equivalent modeling method, the applied voltage value should also be equivalent (eqn. (3.40) [90].

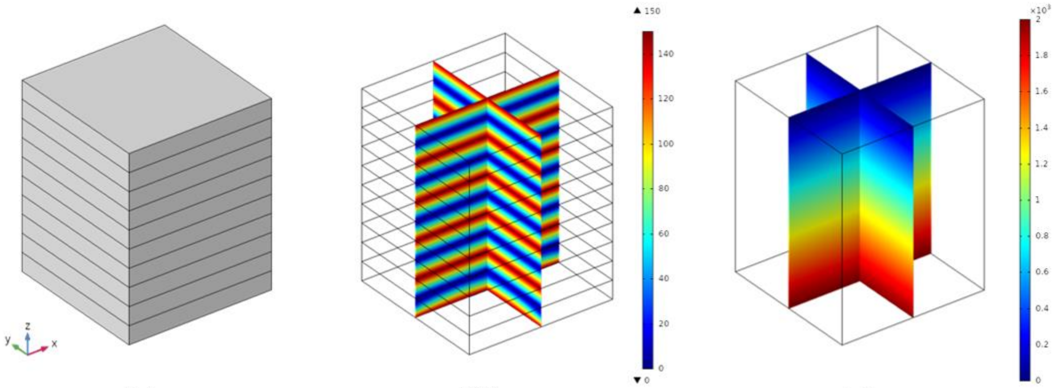

(a) (b) (c)

Figure 3.11 (a) 10 stack PSA, (b) Electric Potential of 10-stack PSA, (c) Electric Potential of Single-stack PSA

$$\phi_{eq} = \frac{\phi_m t_{eq}}{t_m} \tag{3.40}$$

where ϕ_{eq} is the equivalent electric potential, ϕ_m is the real electric potential applied on each layers, t_m is the individual layer thickness and t_{eq} is the thickness of the whole PSA.

In addition, for the optimization work in case study IV, the mechanism angle and arm thickness (Figure 3.12) are optimized using the parametric sweep command.

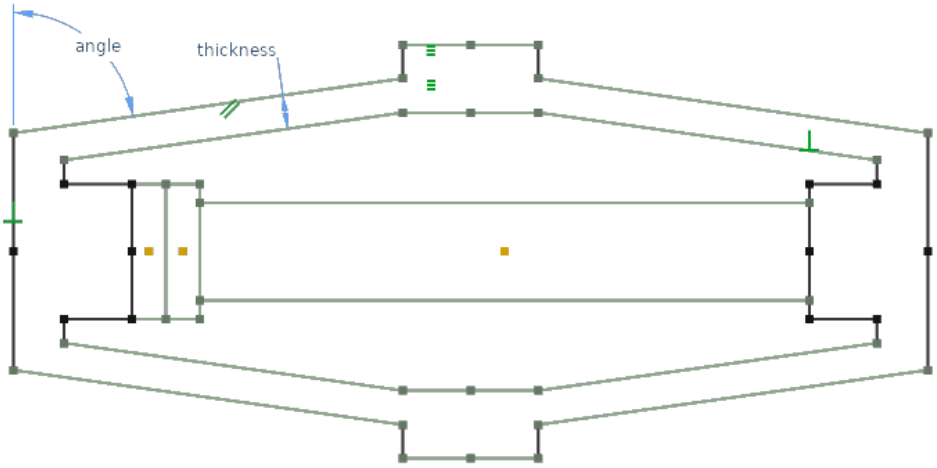

Figure 3.12 Optimization Parameters of RTAM from COMSOL

3.6 Modeling Nonlinearities in Piezoelectric Materials

Up to this point, the linear piezoelectric equations have been established without considering nonlinear effects. In the following sections, the following three nonlinearities will be examined to improve modeling accuracy.

3.6.1 Hysteresis

As previously mentioned in section 2.2.1, equation for the Classical Bouc-Wen (CB-W) model is as follows:

$$m\ddot{x} + b\dot{x} + kx = k(du - h) \tag{3.41}$$

$$\dot{h} = \alpha d\dot{u} - \beta|\dot{u}|h - \gamma\dot{u}\,|h| \tag{3.42}$$

where d (m/V), is the effective coefficient, u (volts) is the input voltage, and h (m) is the hysteretic state variable, and block diagram representation of CB-W is is illustrated in the figure below.

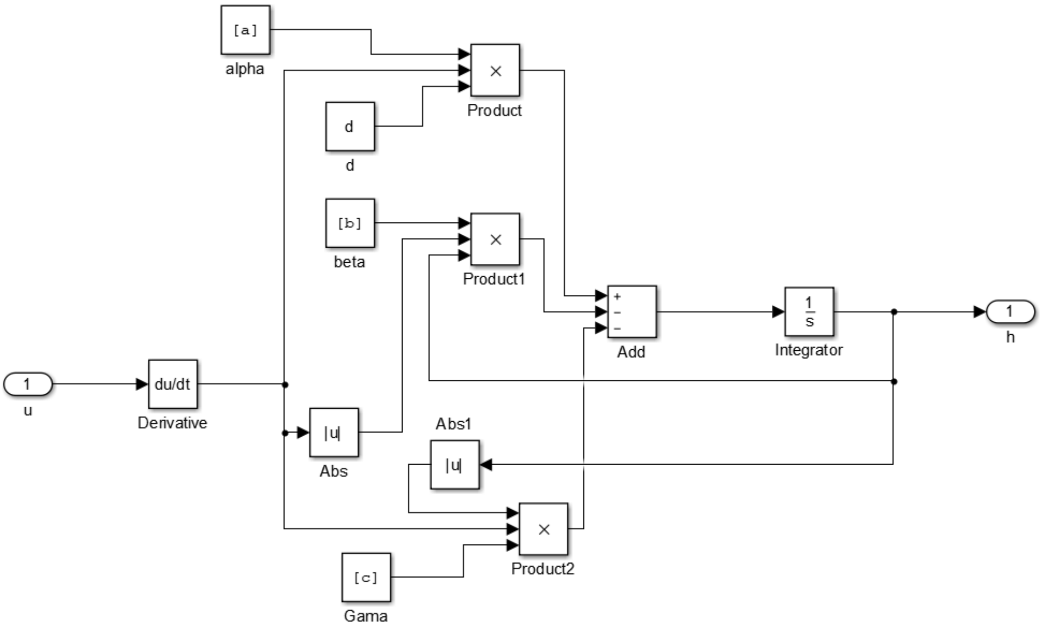

Figure 3.13 Simulink block diagram of Bouc-Wen hysteresis model

Classical Bouc-Wen and modified Bouc-Wen models were presented in Table 2.2 at section 2.2.1. Since the accuracy of these models is restricted by a limited input voltage range, a novel modified Bouc-Wen model is developed. In this model, parameters α and β has dual values according to whether state is in ascending phase or descending phase. In other words, α and β has values α_1 and β_1 when du/dt is positive, and values α_2 and β_2 when du/dt is negative. Parameter γ remains as single valued since its effects turned out to be negligible.

A "function" that takes two or more different values in its range for at least one point in its domain is referred to as a multivalued function [91]. So, this developed novel model is named as “Multivalued Bouc-Wen Model” (MVB-W). The Simulink block diagram representation of this model is shown in Figure 3.14.

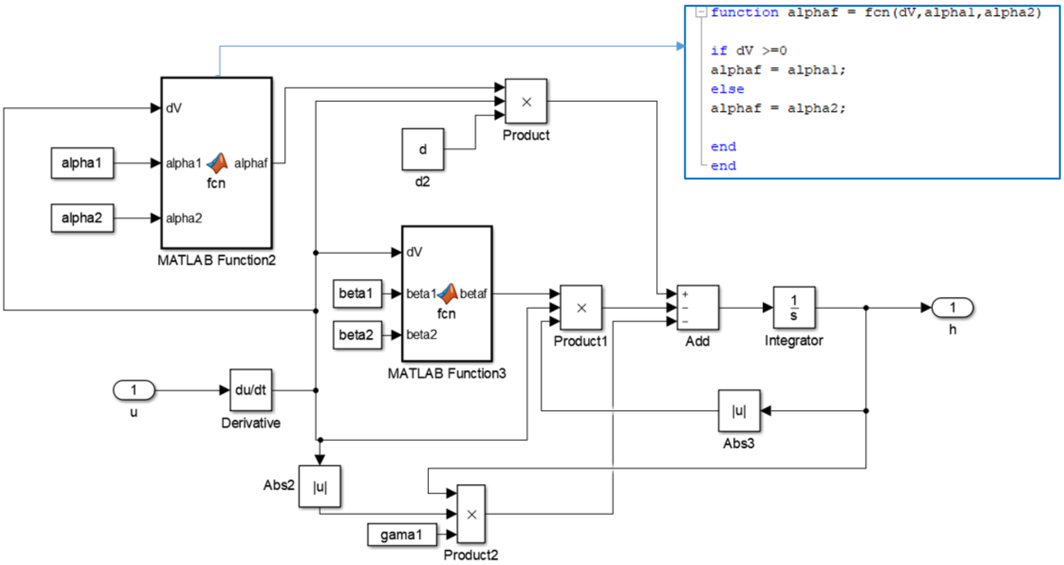

```
function alphaf = fcn(dV,alpha1,alpha2)

if dV >=0
alphaf = alpha1;
else
alphaf = alpha2;

end
end
```

Figure 3.14 Simulink block diagram of MVB-W

Actual displacement x(t) of PSA is equal to summation of linear part X(t) and hysteretic part h(t) as described in below equation. The graphs of X(t) and h(t) is presented in Figure 3.15

$$x(t) = X(t) + h(t) \tag{3.43}$$

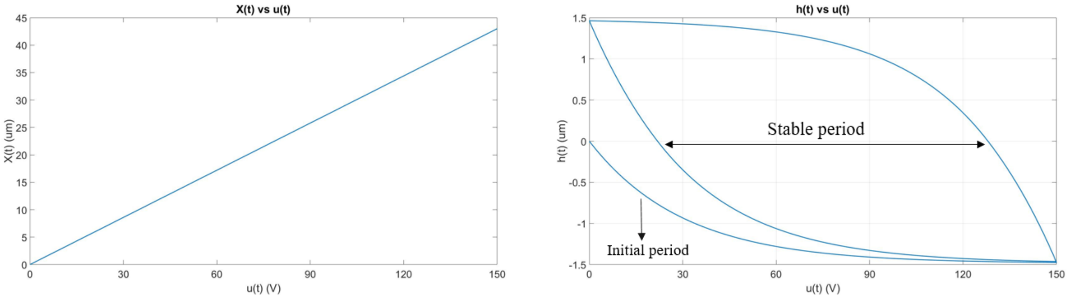

Figure 3.15 Linear and hysteretic parts of the displacement x(t): (a) the linear part and X(t) (b) the hysteretic part h(t) [33]

In CB-W model, shape of hysteresis could be changed by changing parameters α, β and γ as illustrated in Figure 3.16. The common ground of all these shapes is that in stable periods, they are symmetrical with respect to the center point at the (75, 0) coordinate.

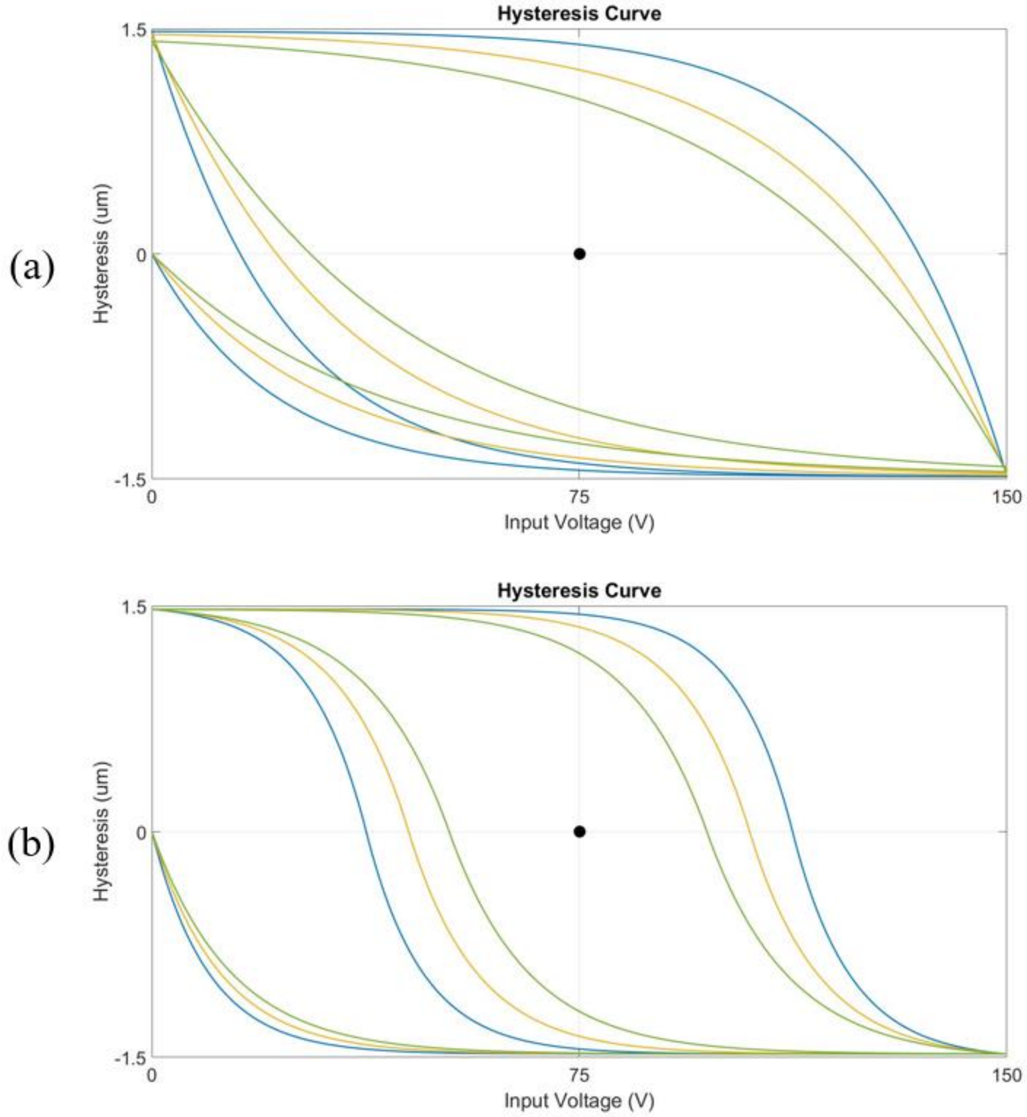

Figure 3.16 Hysteresis h(t) curves with CB-W model

A hysteresis curve of test results derived from linear d_{33} is presented in Figure 3.17-a. It is clear that shape of hysteresis is quite different than CB-W hysteresis shapes (Figure 3.16). This difference explains why it is necessary to develop a modified model. When hysteresis curve is derived from a nonlinear d_{33} (3.45), hysteresis curve becomes more similar to the classical Bouc-Wen model, but the high asymmetry is still present (Figure 3.17-b). Figure 3.17-c present shape of hysteresis of proposed MVB-W model. Thanks to its dual valued parameters according to the uptrend or downtrend of input voltage, this model easily captures asymmetrical hysteresis shape, and this is the main feature which makes MVB-W method powerful.

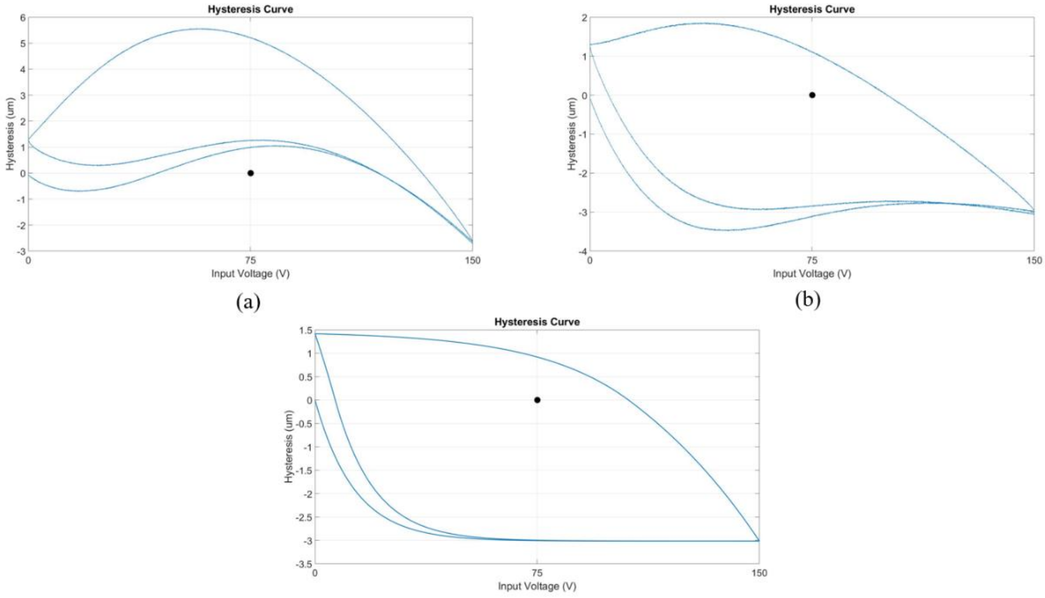

(a) (b)

(c)

Figure 3.17 Hystresis shapes: (a) Test results derived from linear d_{33}, (b) Test results derived from nonlinear d_{33}, (c) MVB-W model results

3.6.2 Creep

For this study, fractional order creep model is selected among the other models previously described in section 2.2.2. In selecting this method, application simplicity and accuracy of the model are the most essential considerations. In Laplace domain, the model is represented as follows:

$$G_c(s) = K_c \left(\frac{1}{s}\right)^{\mu} \tag{3.44}$$

Simulink block diagram representation of fractional order creep model is given in Figure 3.18. In order to run a fractional order transfer function, FOMCON toolbox [92] is installed on MATLAB.

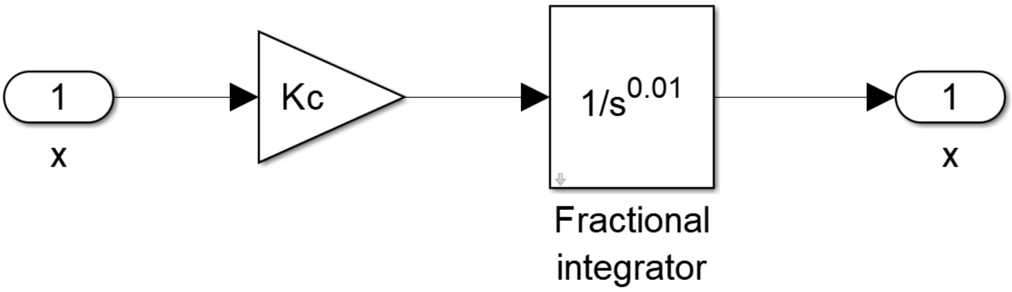

Figure 3.18 Fractional order creep model

3.7 SDOF Nonlinear Modeling

SDOF linear model is a transfer function with mass stiffness and damping. By adding nonlinear d_{33} defined in equation (3.45), previously introduced MVB-W hysteresis and fractional order creep models, SDOF nonlinear model (Figure 3.19) is created.

$$d_{33}(u) = d_2 u^2 + d_1 u + d \tag{3.45}$$

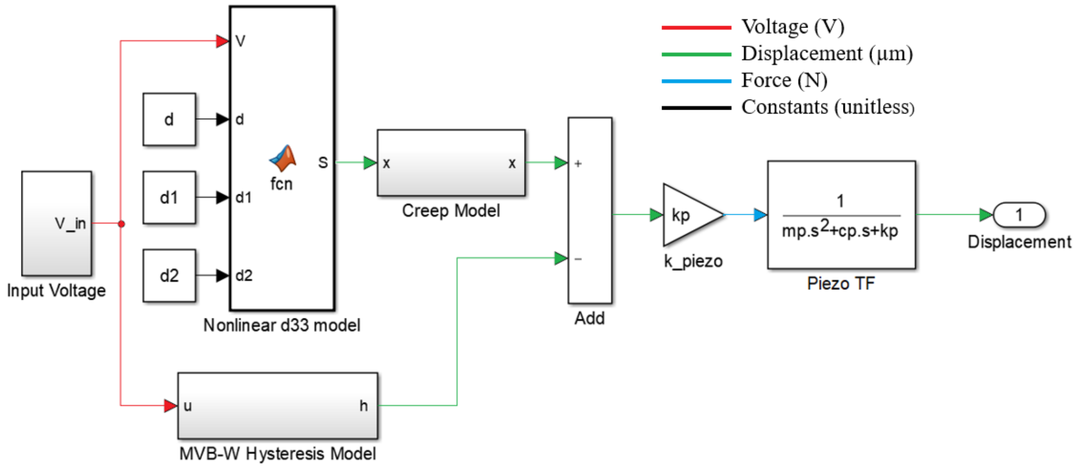

Figure 3.19 SDOF Nonlinear Model of PSA

In order to transform PSA model to RTAM model, mechanism stiffness and amplification ratio are implemented as illustrated in the below figure. Since amplifier mechanism mass is comparable with piezo mass, an equilavent mass is used instead of piezo mass.

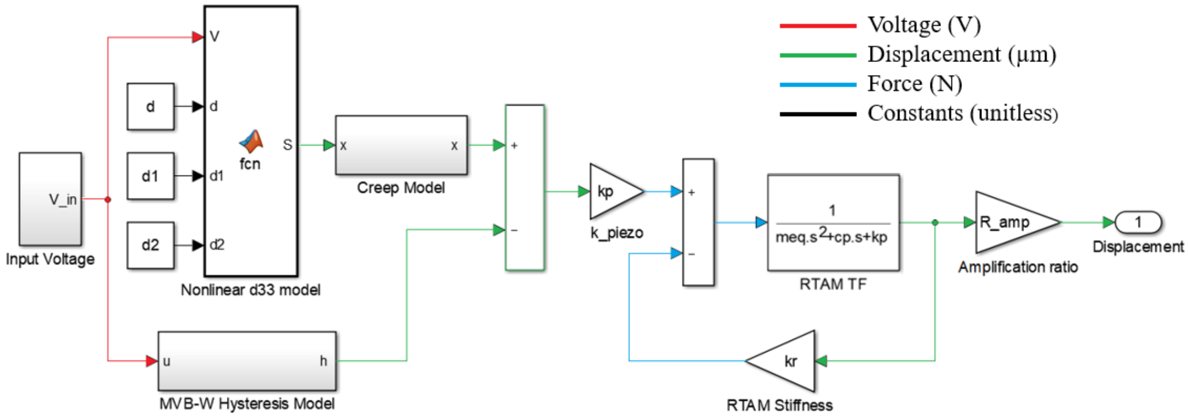

Figure 3.20 Figure 3.21 SDOF Nonlinear Model of RTAM

3.8 Parameter Estimation Methodology

In this study, parameter estimation toolbox of MATLAB/Simulink R2015b is utilized to find parameters of hysteresis (Case Study II) and creep (Case Study III) models. The parameters are identified by nonlinear least squares method with Trust-Region-Reflective algorithm as shown in Figure 3.22. Objective and cost functions are given in below equations, respectively.

$$F = Min \sum_{i=1}^{n} f^2(u) \tag{3.46}$$

$$f(u) = y_i^e(t) - y_i^m(t) \tag{3.47}$$

where y_i^e and y_i^m are experimental and model output, respectively. In order to qualify modeling errors, the root mean square error (RMSE) is defined as:

$$e_{rms} = \sqrt{\frac{1}{T}\int_0^T f^2(u)dt} \tag{3.48}$$

where T is the total time. To quantify modeling errors as a percentage, relative root-mean-square error (RRMSE) δ are defined as:

$$\delta = \frac{e_{rms}}{\max(x(t))}\ x\ 100\ \% \tag{3.49}$$

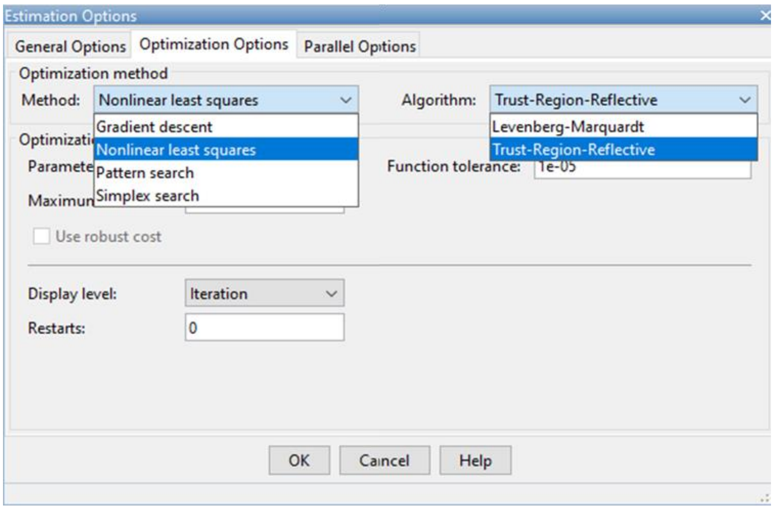

Method: Nonlinear least squares

Algorithm: Trust-Region-Reflective

Function tolerance: 1e-05

☐ Use robust cost

Display level: Iteration

Restarts: 0

Figure 3.22 Simulink parameter estimation toolbox

CHAPTER 4

EXPERIMENTS

This chapter presents experimental setup for the PSA, certain essential test results and amplifier mechanism installation setup, respectively.

4.1 Test Setup

PSA displacement is measured on the setup illustrated in the below figure. The set-up is composed of PSA with strain gauge attached as test unit, Piezo voltage amplifier, DAQ card, loadcell, xPC target, and main PC.

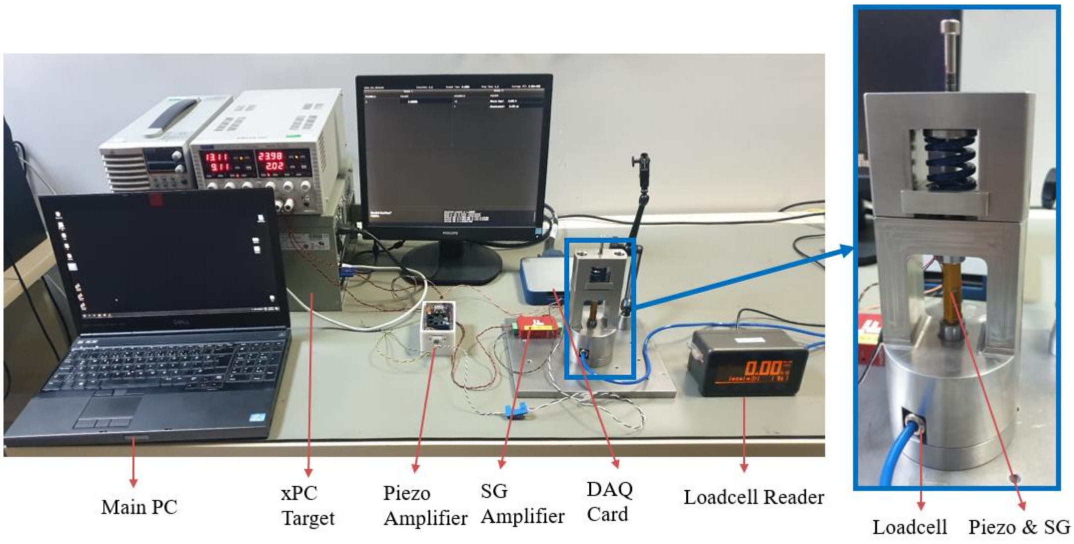

Figure 4.1 PSA test setup

Experimental method for data acquisition is as follows: xPC target and main PC are connected via TCP/UIP communication protocol. Input voltage commands send through the piezo amplifier (PiezoDrive PDu150) to PSA (Piezodrive SCL070736), and output voltage data is obtained for the SG amplifier to measure displacement. Also, preload value is observed through the loadcell reader, separately. The schematic of the test setup is illustrated in the below figure.

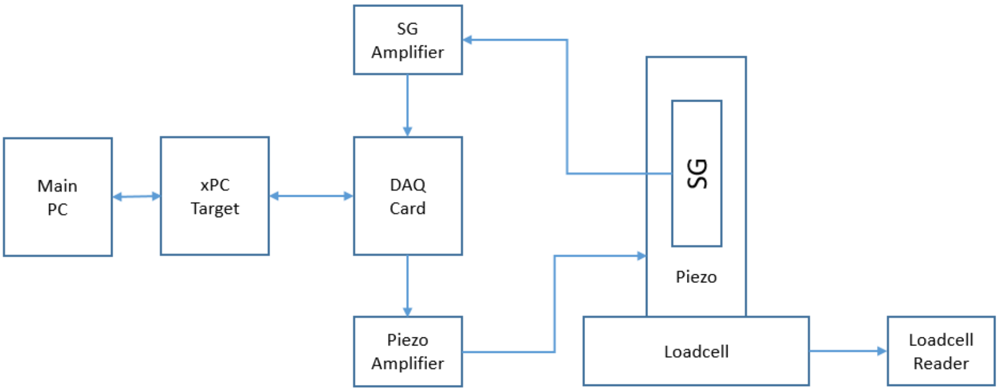

Figure 4.2 Schematic test setup

In order to test the PSA displacement under different preloads, a mechanism whose solid model is visualized in Figure 4.3 is designed. In this mechanism, PSA is placed between upper and lower pins, and preloading is performed by tightening the bolt on top of green spring. Finally, preloading force is measured with the loadcell.

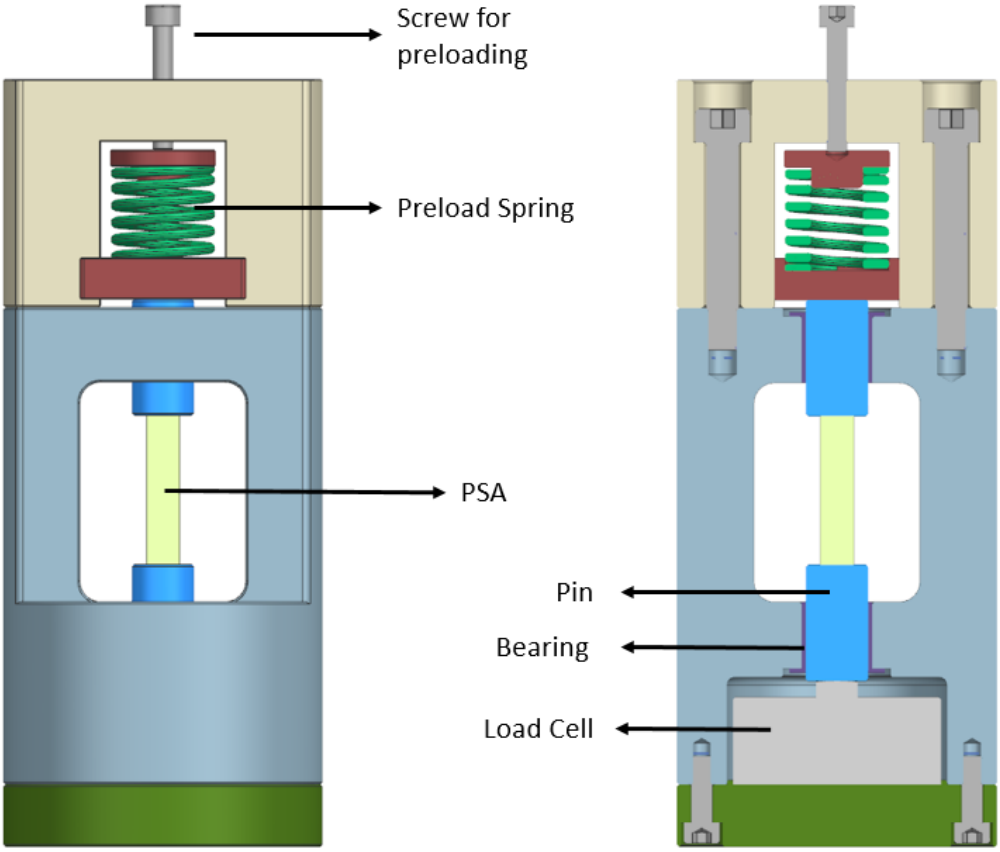

Figure 4.3 Preload mechanism

In order to validate strain gauge measurements a laser displacement sensor (MTI Instruments DTS-025-02) is implemented (Figure 4.4). In addition to that, measurement of RTAM is also performed with laser sensor (Figure 4.5).

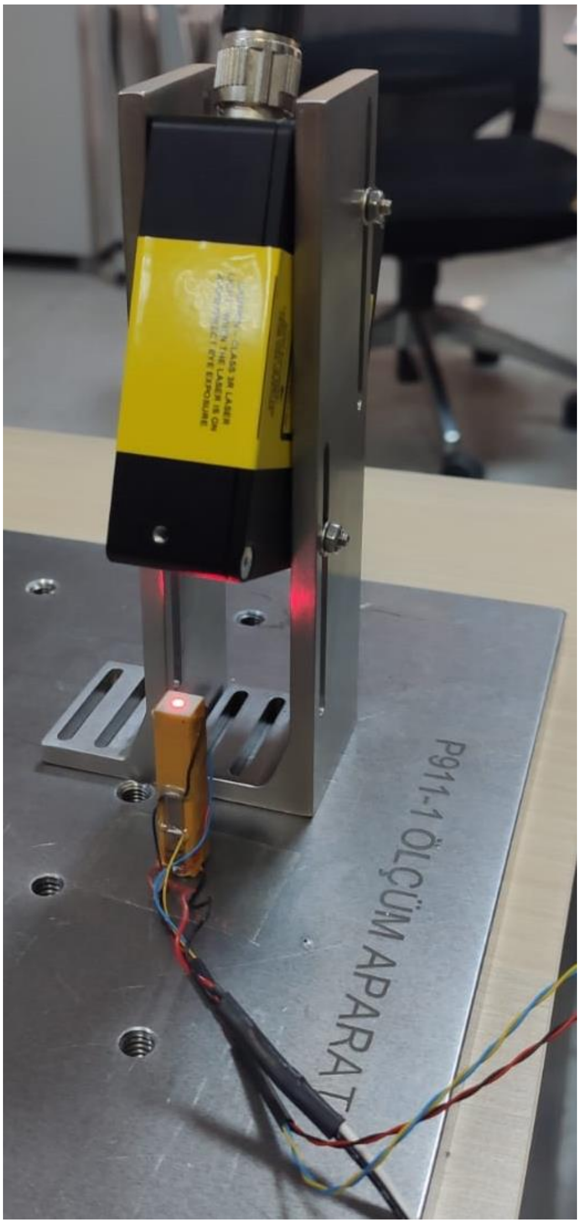

Figure 4.4 PSA measurement setup

Figure 4.5 RTAM measurement setup

4.2 Test Results

This section shows the most significant outcomes of experiments with experiment plots. Figure 4.6 shows hysteretic behavior under different preloads. As it can be concluded from the figure, prestress has an impact on shape of hysteresis. Numerical values in Table 4.1 reveals that hysteresis gap tends to increase as prestress increases.

Also, the voltage point at which maximum hysteresis occurs shifts to the right as prestress increases.

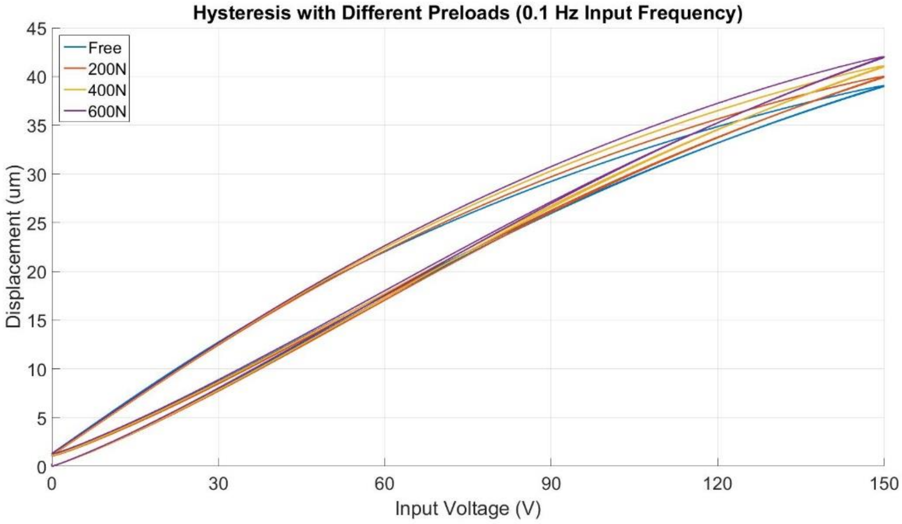

Figure 4.6 Hysteresis curves with different preloads

Table 4.1 Hysteresis values with different preloads

Preload	Max Hysteresis (µm)	Voltage (V)
Free	4.53	48.4
200 N	4.71	53.1
400 N	4.75	55.9
600 N	4.78	58.7

Figure 4.7 compares results of strain gauge and laser displacement sensor under no load case with 0.1 Hz input frequency. It is shown that the results are very similar.

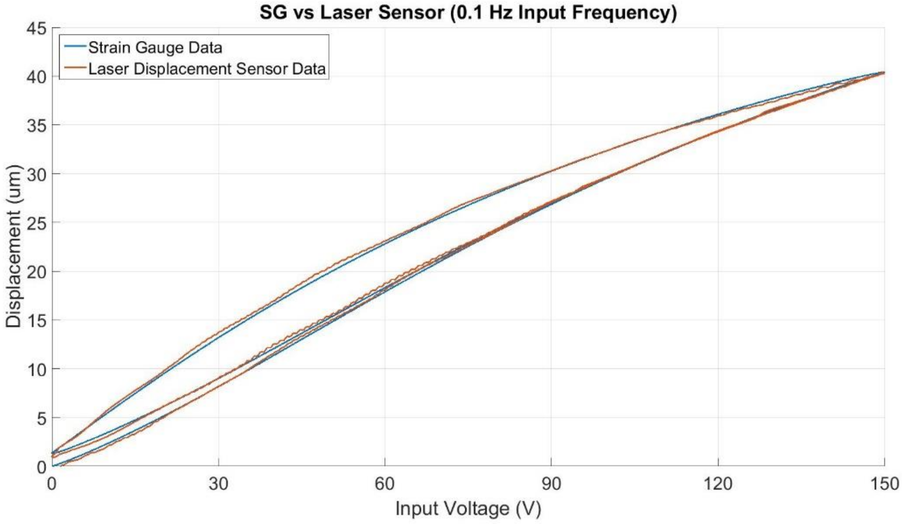

Figure 4.7 Hysteresis curves with different sensors

Variation of d_{33} with prestress and voltage is presented in Figure 4.8. After examining the effect of voltage on the shape of the d_{33} curve, a two degree polynomial (eqn. (3.45) is fitted to represent input voltage dependency of parameter d_{33}. Another important observation that can be made from this figure is that prestress has a negative impact on d_{33} up to a point (approx. 72V). However, after that point, prestress starts to boost d_{33} value.

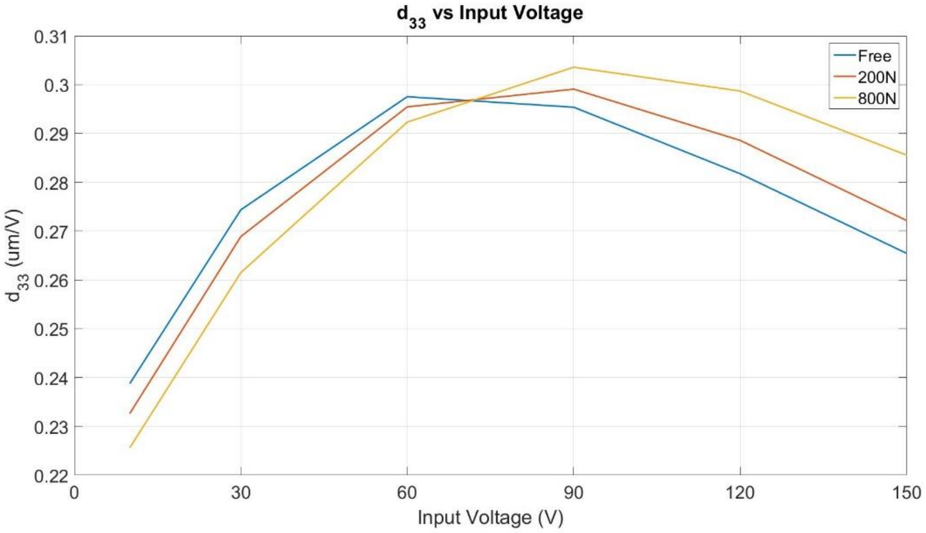

Figure 4.8 d_{33} with different preloads

As a final study of this chapter, the creep behavior is tested under 10, 30, 60 and 90V DC excitations with free boundary conditions and 800 N preload. It can be understood from below table that prestress has also an impact on creep nonlinearity. In addition, it is shown that influence of prestress increases as excitation voltage increases. Although, test results shows that creep effect is insignificant compared to hysteresis, it may lead non-negligible error in the long term. Thus, in quasi-static DC voltage excitation applications, creep should be modeled to increase precision.

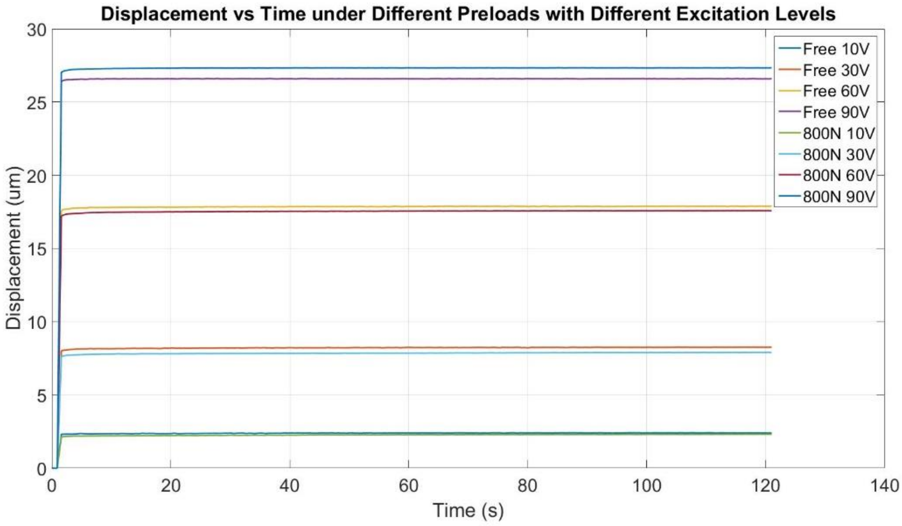

Figure 4.9 Creep under different preloads with different excitation levels

4.3 Amplifier Mechanism Installation Setup

An installation setup (Figure 4.10) is designed to mount PSA in RTAM with predefined prestress. The setup is used as follows:

- The up and down distance of RTAM is measured.
- RTAM is placed in the mechanism while the inside is empty.
- Space inside RTAM is enlarged by compressing the red spring via tightening the screw on top of it.
- The amount of compression is determined by measuring the distance between the spacer parts
- PSA and aluminum wedge inserted into the interior
- After mounting, RTAM is released by loosening the bolt
- The up and down distance of RTAM is measured again
- The difference between before installation and after installation is found, and the amount of prestress on the piezo is found by using lateral stiffness (k_{33}) value of RTAM (Eqn. (3.12)

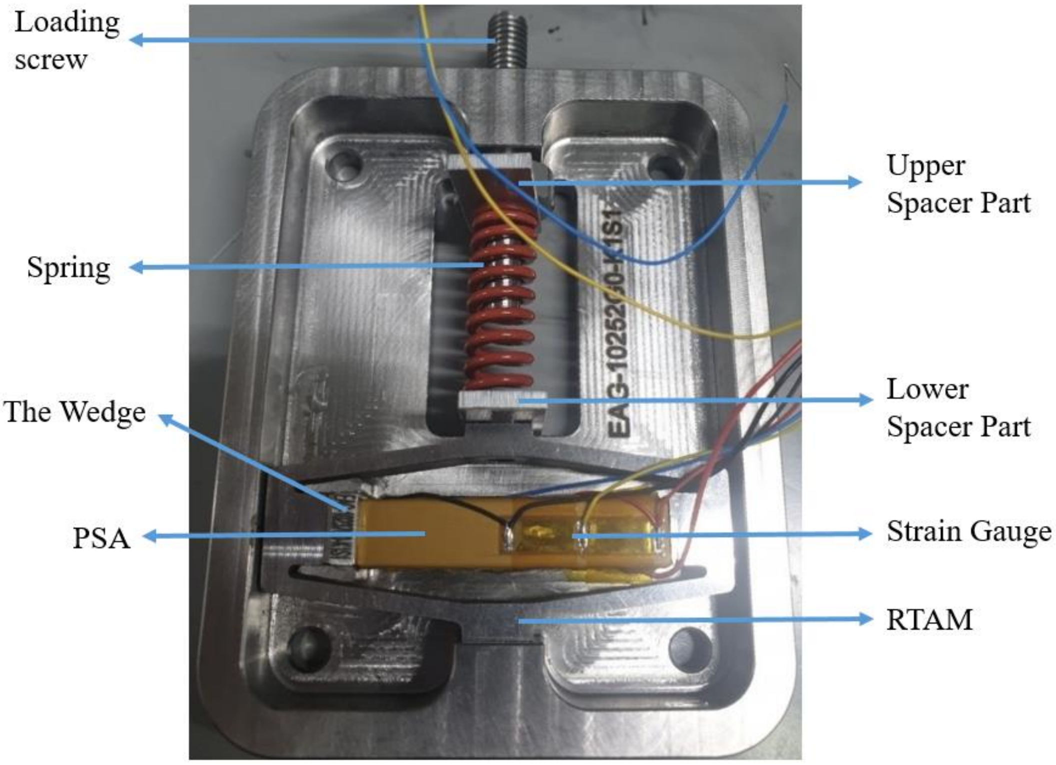

Figure 4.10 RTAM Preload Mechanism

CHAPTER 5

CASE STUDIES

Case studies demonstrating the validity and effectiveness of the suggested methodologies are provided in this chapter

5.1 Case Study I: Single Piezoelectric Element Analysis

As the first case study, a basic single piezoelectric (8-noded brick element) is analyzed. Both hand calculation and COMSOL analysis is carried out to reveal how COMSOL assembly and solve electromechanically coupled equations.

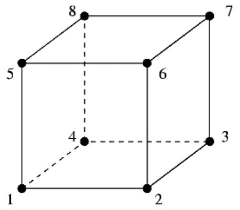

Figure 5.1 8-noded brick element

In 3-D FEA of piezoelectric domain, each node has 4 degrees of freedom. While the first three DOF is x,y and z-axis displacement values, the fourth DOF is the electric potential value. Shape functions for 3-DOF mechanical displacement field, and 1-DOF electric potential field are defined as:

$$[N_u] = \begin{bmatrix} N_1 & 0 & 0 & N_2 & 0 & 0 & \dots & 0 \\ 0 & N_1 & 0 & 0 & N_2 & 0 & \dots & 0 \\ 0 & 0 & N_1 & 0 & 0 & N_2 & \dots & N_8 \end{bmatrix}_{3x24} \tag{5.1}$$

$$N_\phi = [\, N_1\, N_2\, N_3 \, \dots \dots N_8]_{1x8} \tag{5.2}$$

$$N_i(x,y,z) = \frac{1}{8}(1 + xx_i)(1 + yy_i)(1 + zz_i) \tag{5.3}$$

where N_i is linear shape function approximation of the i^th node. By using shape function derivation definitions (3.24) and (3.25), B_u and B_ϕ results in the following expressions:

$$[B_u] = \begin{bmatrix} \frac{\partial N_1}{\partial x} & 0 & 0 & \frac{\partial N_2}{\partial x} & 0 & 0 & \dots & 0 \\ 0 & \frac{\partial N_1}{\partial y} & 0 & 0 & \frac{\partial N_2}{\partial y} & 0 & \dots & 0 \\ 0 & 0 & \frac{\partial N_1}{\partial z} & 0 & 0 & \frac{\partial N_2}{\partial z} & \dots & \frac{\partial N_8}{\partial z} \\ 0 & \frac{\partial N_1}{\partial z} & \frac{\partial N_1}{\partial y} & 0 & \frac{\partial N_2}{\partial z} & \frac{\partial N_2}{\partial y} & \dots & \frac{\partial N_8}{\partial y} \\ \frac{\partial N_1}{\partial z} & 0 & \frac{\partial N_1}{\partial x} & \frac{\partial N_2}{\partial z} & 0 & \frac{\partial N_2}{\partial x} & \dots & \frac{\partial N_8}{\partial x} \\ \frac{\partial N_1}{\partial y} & \frac{\partial N_1}{\partial x} & 0 & \frac{\partial N_2}{\partial y} & \frac{\partial N_2}{\partial x} & 0 & \dots & 0 \end{bmatrix}_{6x24} \tag{5.4}$$

$$[B_\phi] = \begin{bmatrix} \frac{\partial N_1}{\partial x} & \frac{\partial N_2}{\partial x} & \dots & \frac{\partial N_8}{\partial x} \\ \frac{\partial N_1}{\partial y} & \frac{\partial N_2}{\partial y} & \dots & \frac{\partial N_8}{\partial y} \\ \frac{\partial N_1}{\partial z} & \frac{\partial N_2}{\partial z} & \dots & \frac{\partial N_8}{\partial z} \end{bmatrix}_{3x8} \tag{5.5}$$

Table 5.1 provides material properties of PZT-5H material properties in stress-charge form.

Table 5.1 PZT-5H Material Properties

Property	Tensor	Unit
Elasticity, $[c^E]$	$\begin{bmatrix} 126 & 79.5 & 84.1 & 0 & 0 & 0 \\ 79.5 & 126 & 84.1 & 0 & 0 & 0 \\ 84.1 & 84.1 & 126 & 0 & 0 & 0 \\ 0 & 0 & 0 & 23.3 & 0 & 0 \\ 0 & 0 & 0 & 0 & 23 & 0 \\ 0 & 0 & 0 & 0 & 0 & 23 \end{bmatrix} x10^9$	Pa
Piezoelectric Coupling, $[e]$	$\begin{bmatrix} 0 & 0 & 0 & 0 & 17 & 0 \\ 0 & 0 & 0 & 17 & 0 & 0 \\ -6.5 & 0 & 0 & 0 & 0 & 23 \end{bmatrix}$	C/m^2
Permittivity, $[\varepsilon]$	$\begin{bmatrix} 1.5 & 0 & 0 \\ 0 & 1.5 & 0 \\ 0 & 0 & 1.3 \end{bmatrix} x10^{-8}$	F/m

Applied boundary conditions for this problem and node numbering are shown in Figure 5.2. Bottom nodes is fixed mechanically and 200 V electric potential is applied on them, while the mechanical displacements of nodes at the top is free and these nodes are electrically grounded.

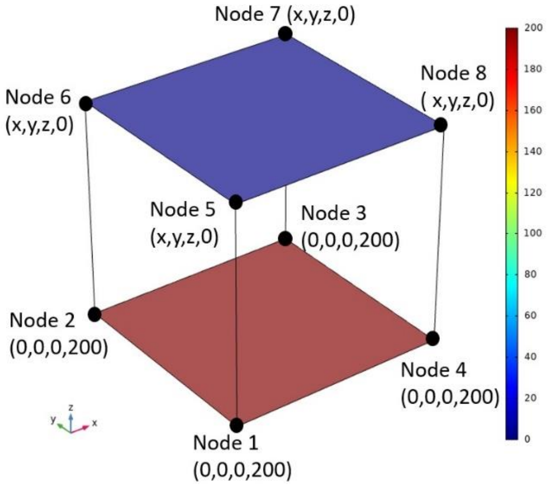

Figure 5.2 BC’s and node numbering of 8-noded brick element

Since the problem is static, equation (3.31) reduces to equation (5.6) by dropping mass term.

$$[K_{uu}]\{u\} + [K_{u\phi}]\{\phi\} = \{f\} \tag{5.6}$$

By inserting material properties into equations (3.36) and (3.37) stiffness and piezoelectric coupling matrices are calculated. After substituting electrical potential field and mechanical force field and partitioning operation, equation (5.6) is solved for unknown nodal displacement values. Also, a COMSOL model is prepared for this problem. An important note that linear discretization is selected since the selected shape function for hand calculation is also linear. The figure below compares the results of COMSOL and hand calculation in μm. There are 0.014 % error in z direction and %0.040 error in x, y directions. Source of this small discrepancy is large difference in order of magnitude of some material parameters (i.e, elasticity and permittivity matrices)

Hand Calculation Results

$$u = \begin{bmatrix} 0.02603 \\ 0.02603 \\ 0.07173 \\ 0.02603 \\ -0.02603 \\ 0.07173 \\ -0.02603 \\ -0.02603 \\ 0.07173 \\ -0.02603 \\ 0.026035 \\ 0.071739 \end{bmatrix} \begin{matrix} x \\ y \\ z \\ x \\ y \\ z \\ x \\ y \\ z \\ x \\ y \\ z \end{matrix} \begin{matrix} \left.\begin{matrix} \\ \\ \\ \end{matrix}\right\} \text{Node 5} \\ \left.\begin{matrix} \\ \\ \\ \end{matrix}\right\} \text{Node 6} \\ \left.\begin{matrix} \\ \\ \\ \end{matrix}\right\} \text{Node 7} \\ \left.\begin{matrix} \\ \\ \\ \end{matrix}\right\} \text{Node 8} \end{matrix}$$

COMSOL Results

$$u = \begin{bmatrix} 0.02604 \\ 0.02604 \\ 0.07172 \\ 0.02604 \\ -0.02604 \\ 0.07172 \\ -0.02604 \\ -0.02604 \\ 0.07172 \\ -0.02604 \\ 0.02604 \\ 0.07172 \end{bmatrix} \begin{matrix} x \\ y \\ z \\ x \\ y \\ z \\ x \\ y \\ z \\ x \\ y \\ z \end{matrix} \begin{matrix} \left.\begin{matrix} \\ \\ \\ \end{matrix}\right\} \text{Node 5} \\ \left.\begin{matrix} \\ \\ \\ \end{matrix}\right\} \text{Node 6} \\ \left.\begin{matrix} \\ \\ \\ \end{matrix}\right\} \text{Node 7} \\ \left.\begin{matrix} \\ \\ \\ \end{matrix}\right\} \text{Node 8} \end{matrix}$$

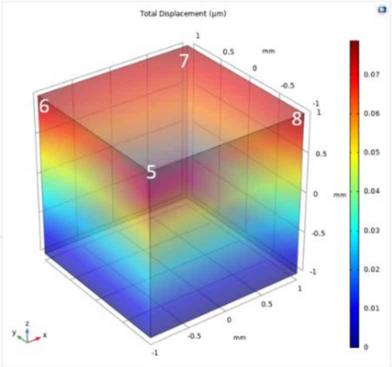

Figure 5.3 Hand calculation vs COMSOL results

5.2 Case Study II: MVB-W Model Parameter Identification

For case studies II, III and IV, a PSA (Piezodrive SCL070736), illustrated in Figure 5.4, is utilized. Properties of PSA are given in the Table 5.2.

Figure 5.4 PiezoDrive SCL070736

Table 5.2 PSA Parameters [93]

Parameter	**Value**
Type	SCL070736
Size	7 mm x 7 mm x 36 mm
Stroke (0 to 150V)	38 µm
Stroke (-30 to 150V)	50 µm
Stiffness	50 N/µm
Blocking Force	1900 N
Mass	14 gr
Resonant Frequency	35 kHz

In this case study, Bouc-Wen parameters, and d_{33} parameters of the PSA are identified with nonlinear least squares method. For the identification of CB-W, triangular wave input with 0.1Hz is used. However, a more complex input voltage (0-150-0-150-0-120-0-90-0-60-0-30-0) presented in Figure 5.5 is preferred in MVB-W model. The main reason for choosing such an input voltage is that if the MVB-W model is not characterized by intermittent voltages, although it shows very high matching performance at that specific voltage profile for which it is characterized, it shows inappropriate matching at other voltages. That’s why, MVB-W parameters should be identified with an wide range input voltage profile for corresponding application.

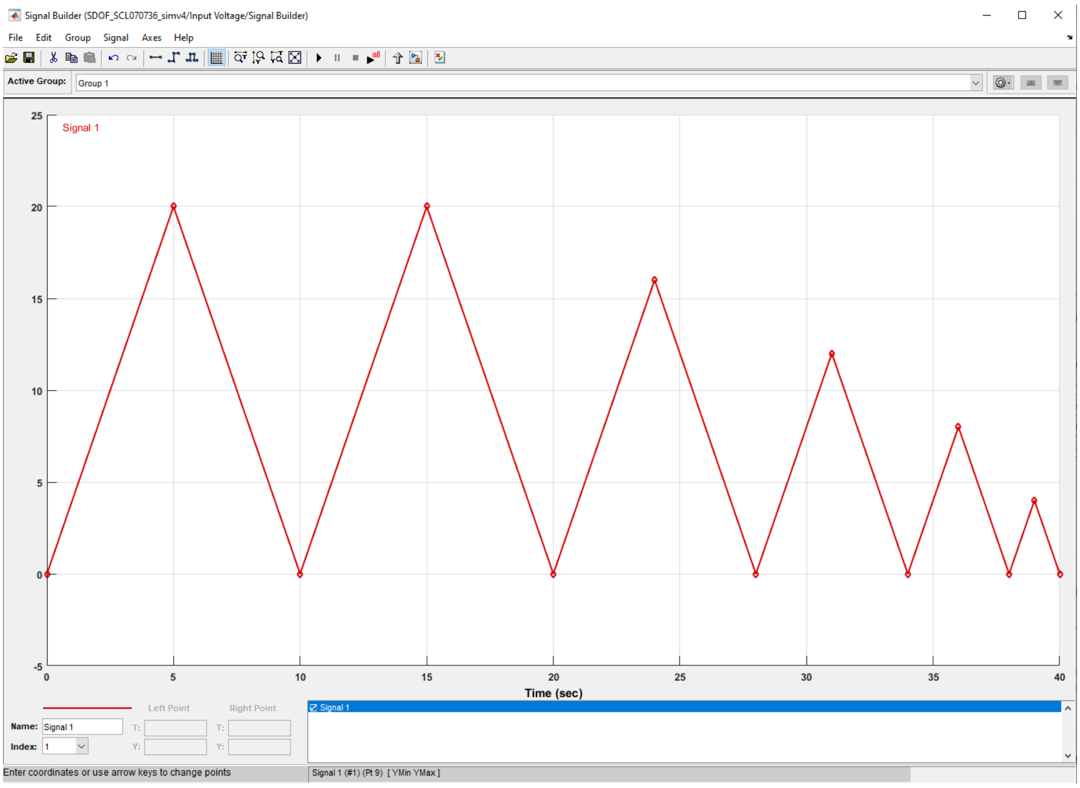
Signal Builder (SDOF_SCL070736_simv4/Input Voltage/Signal Builder)

Active Group: Group 1

Name: Signal 1

Index: 1

☑ Signal 1

Enter coordinates or use arrow keys to change points

Signal 1 (#1) (Pt 9) [YMin YMax]

Figure 5.5 Input voltage curve for MVB-W identification

Results of MVB-W and CB-W models with different preloads are presented in Table 5.3. α, β and γ are Bouc-wen parameters, and subscript 1 denotes ascending loop for hysteresis curve, while subscript 2 represents descending loops. Parameters d, d_1 and d_2 is for input dependent nonlinear d_{33} model which is explained in section 3.7.

Table 5.3 Comparison of MVB-W and CB-W with different preloads

Parameters /Models	**Free MVB-W**	**Free CB-W**	**200 N MVB-W**	**200 N CB-W**	**800 N MVB-W**	**800 N CB-W**
$\boldsymbol{\alpha_1}$	0.855	0.734	0.846	0.204	0.709	0.192
$\boldsymbol{\alpha_2}$	0.176	-	0.187	-	0.166	-
$\boldsymbol{\beta_1}$	5.16E-02	9.31E-02	5.21E-02	2.58E-06	5.36E-02	6.55E-06
$\boldsymbol{\beta_2}$	8.02E-03	-	7.74E-03	-	9.21E-03	-
$\boldsymbol{\gamma}$	0.024	0.001	0.024	0.017	0.027	0.018
$\boldsymbol{d}$	0.403	0.296	0.413	0.316	0.414	0.330
$\boldsymbol{d_1}$	-8.84E-04	-	-9.22E-04	-	-7.42E-04	-
$\boldsymbol{d_2}$	8.25E-07	-	9.21E-07	-	-3.87E-08	-
RMSE (μm)	0.246	1.835	0.251	1.171	0.247	1.445
RRMSE (%)	0.610%	4.543%	0.609%	2.835%	0.612%	3.353%

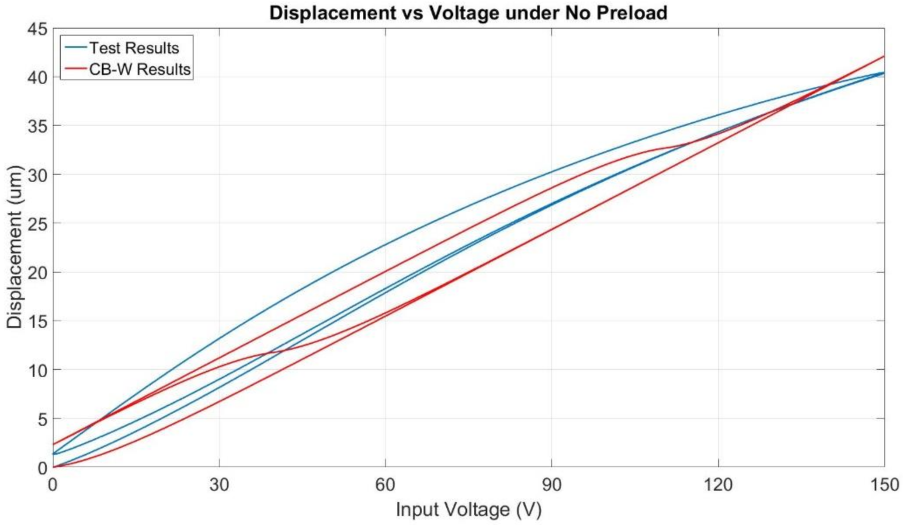

Figure 5.6 Test vs CB-W results under no load

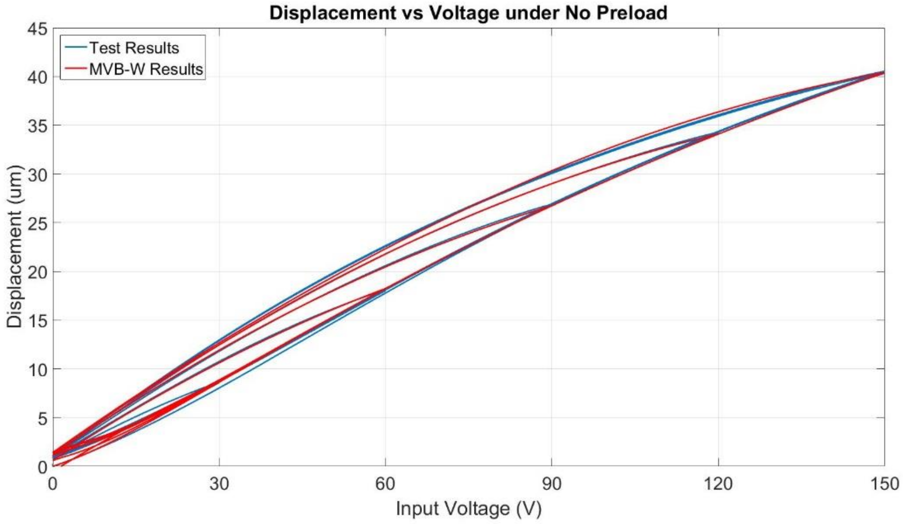

Figure 5.7 Test vs MVB-W results under no load

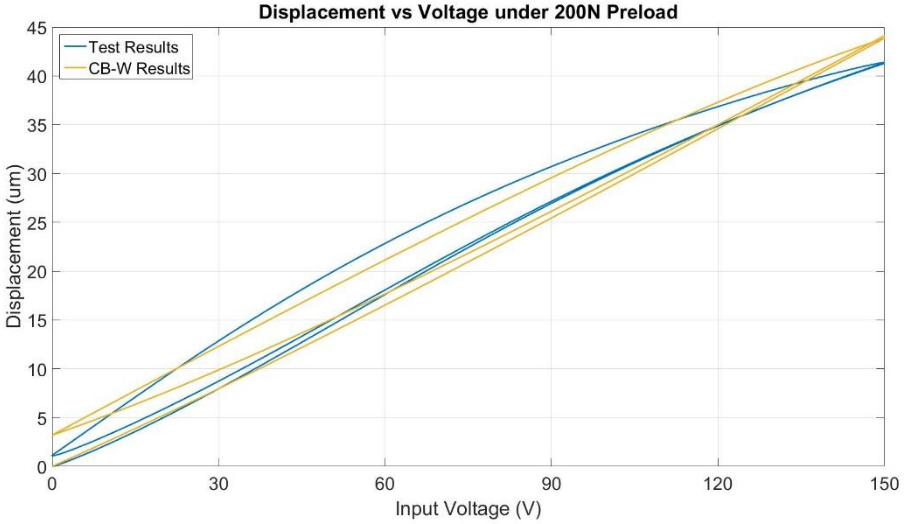

Figure 5.8 Test vs CB-W results under 200N Preload

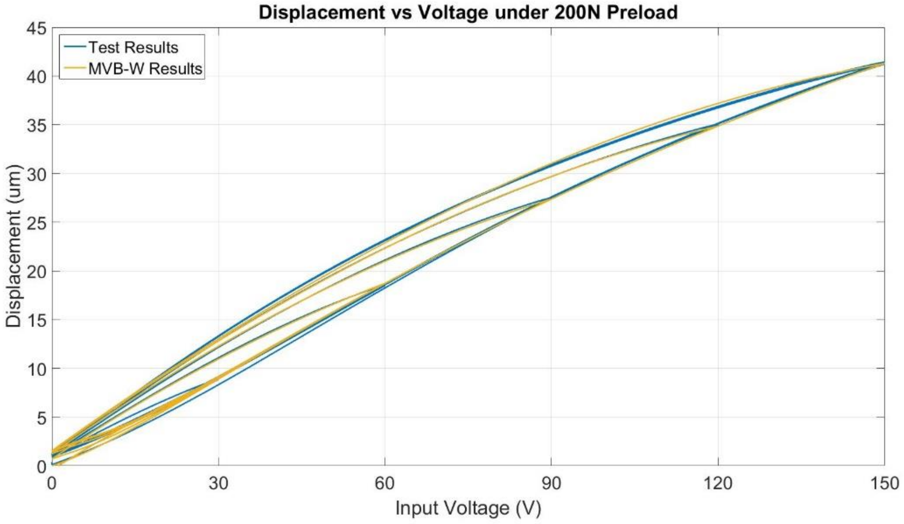

Figure 5.9 Test vs MVB-W results under 200N Preload

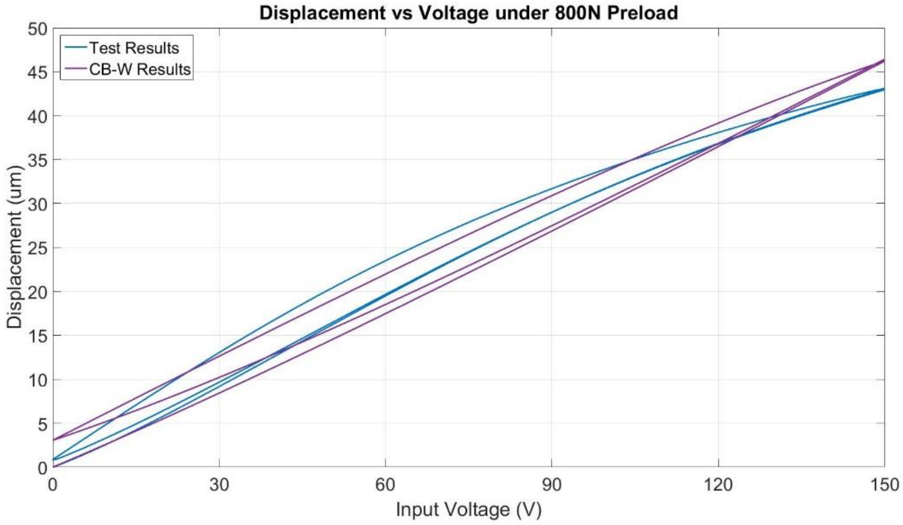

Figure 5.10 Test vs CB-W results under 800N Preload

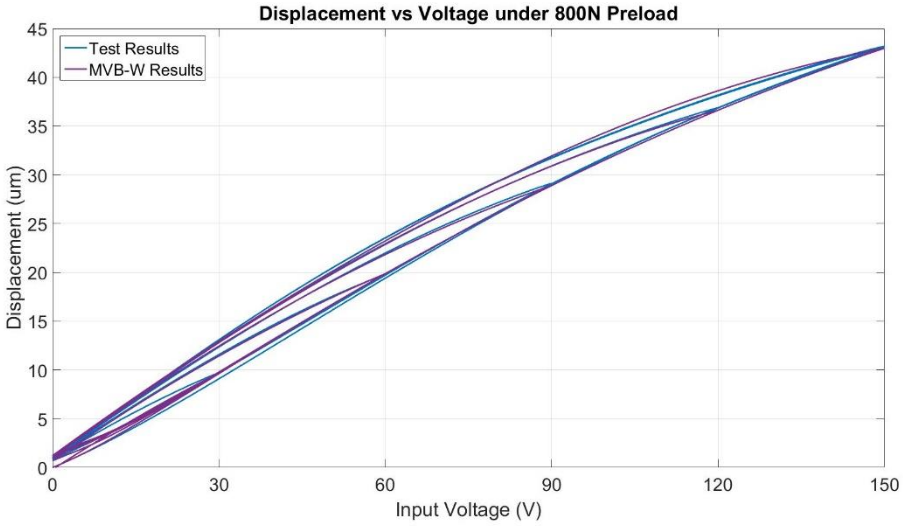

Figure 5.11 Test vs MVB-W results under 800N Preload

Referring to the figures given above and the results of Table 5.3, it is possible to conclude that Classical Bouc-Wen (CB-W) model cannot adequately capture hysteresis behavior in extended voltage ranges. Since there are enough studies [51], [52], [55], [56] about rate-dependent, i.e. frequency dependent hysteresis, no investigation has been conducted on how the CB-W parameters vary with frequency within the scope of this thesis. Table 5.3 shows that RMS error is reduced to 1.4 um from around 13 um. Thus, these findings revealed that MVB-W model describes hysteresis behavior more exactly than CB-W model for extended voltage ranges.

5.3 Case Study III: Creep Model Parameter Identification

Identification investigations of creep parameters are reported in this case study. As stated before in section 3.6.2, fractional order creep model is chosen within the scope of theses research. Parameters K_c and μ is found by using again nonlinear least squares method for different preloads and different excitation levels.

The creep behavior of PSA under 10 to 90V DC excitation with no preload is provided in Figure 5.12. In order to observe the rate of creep, all displacement values are normalized to 1 by dividing the value by itself at the time of voltage excitation.

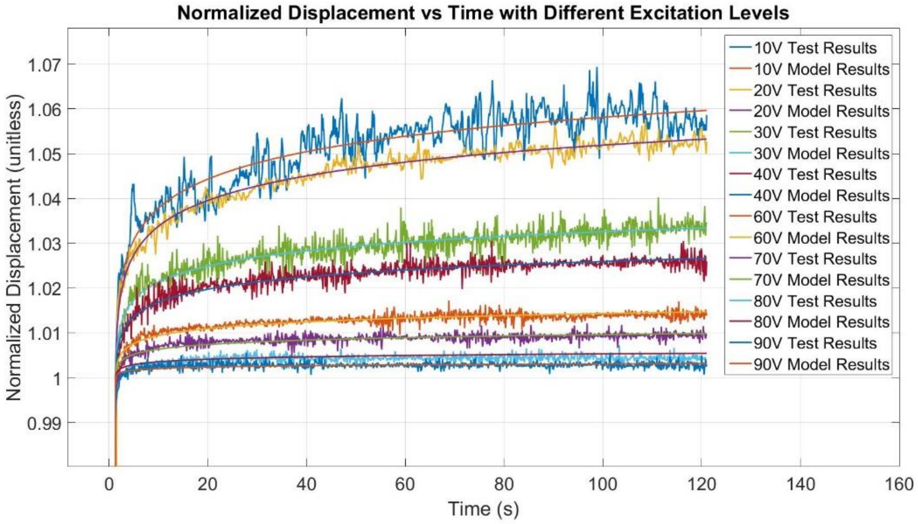

Figure 5.12 Normalized displacement with different excitation levels

Table 5.4 Parameters of creep model under no load with varying input voltage

Voltage / Parameters	K_c	μ	**RMSE (µm)**	**RRMSE (%)**
10	0.886	8.27E-03	5.35E-02	0.67%
20	0.995	7.43E-03	1.01E-02	0.29%
30	1.033	4.70E-03	4.30E-03	0.19%
40	1.076	3.82E-03	2.40E-03	0.14%
60	1.134	2.09E-03	1.20E-03	0.10%
70	1.143	1.38E-03	1.10E-03	0.09%
80	1.142	7.54E-04	9.18E-04	0.09%
90	1.134	4.45E-04	7.05E-04	0.08%

As can be seen from the Figure 5.12 and parameter μ values at the Table 5.4, creep nonlinearity tends to decreases as the input voltage increases.

In the subsequent charts and tabulated data, experimental results and fitted model results under different preloads are presented with 10, 30, 60 and 90V DC input voltage levels, respectively.

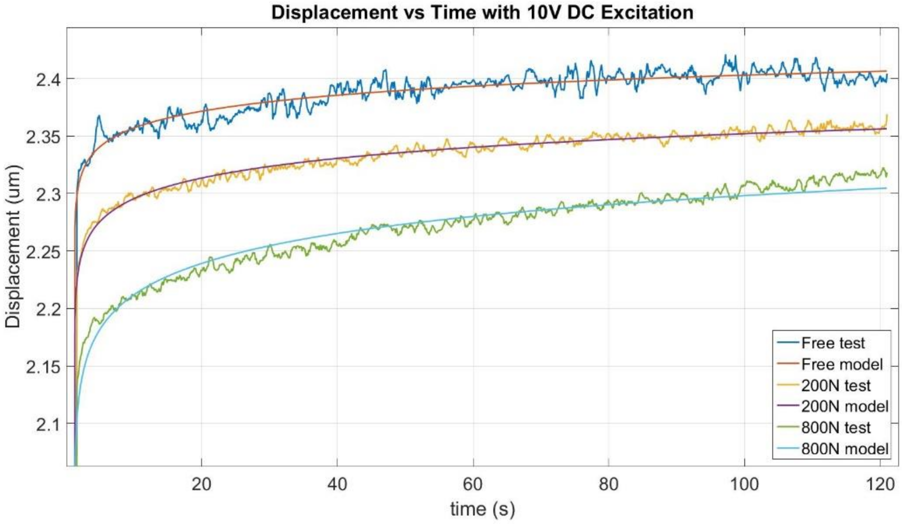

Figure 5.13 Test vs model results with 10V DC excitation under different preloads

Table 5.5 Parameters of creep model with 10V DC excitation

Parameter/ Preload	**Free**	**200 N**	**800 N**
$\boldsymbol{K_c}$	0.886	0.858	0.814
$\boldsymbol{\mu}$	8.27E-03	1.04E-02	1.64E-02
RMSE (μm)	1.60E-02	8.83E-03	1.10E-02
RRMSE (%)	0.67%	0.38%	0.48%

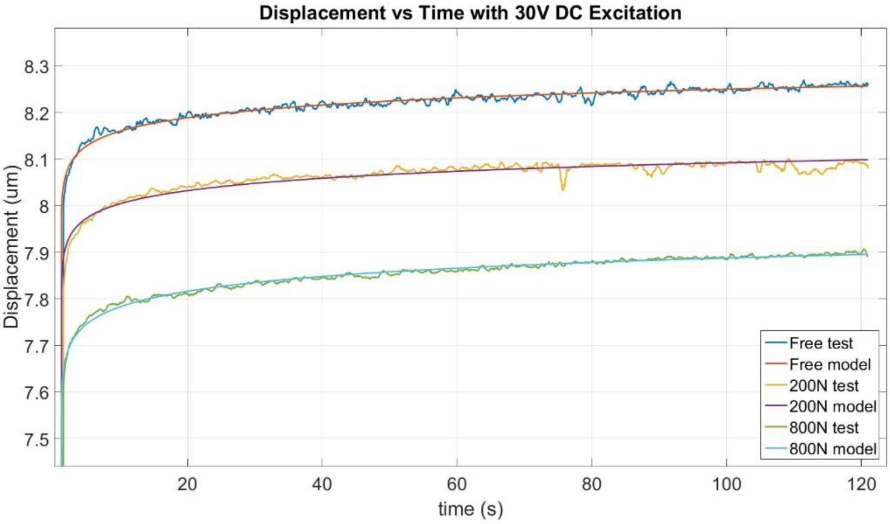

Figure 5.14 Test vs model results with 30V DC excitation under different preloads

Table 5.6 Parameters of creep model with 30V DC excitation

Parameter/ Preload	**Free**	**200 N**	**800 N**
$\boldsymbol{K_c}$	1.033	1.013	0.982
$\boldsymbol{\mu}$	4.70E-03	4.68E-03	5.73E-03
RMSE (μm)	1.54E-02	1.53E-02	9.72E-03
RRMSE (%)	0.19%	0.19%	0.12%

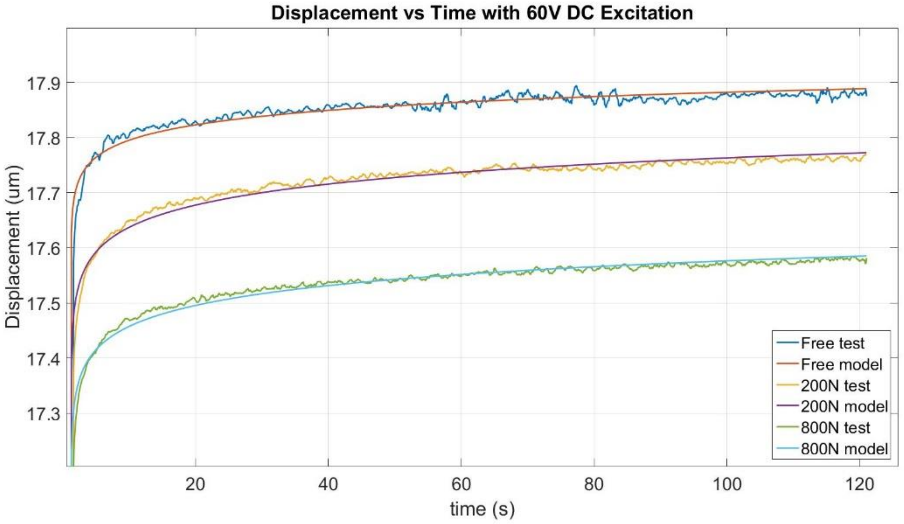

Figure 5.15 Test vs model results with 60V DC excitation under different preloads

Table 5.7 Parameters of creep model with 60V DC excitation

Parameter/ Preload	**Free**	**200 N**	**800 N**
$\boldsymbol{K_c}$	1.134	1.121	1.110
$\boldsymbol{\mu}$	2.09E-03	3.04E-03	2.90E-03
RMSE (μm)	1.76E-02	1.44E-02	1.30E-02
RRMSE (%)	0.10%	0.08%	0.07%

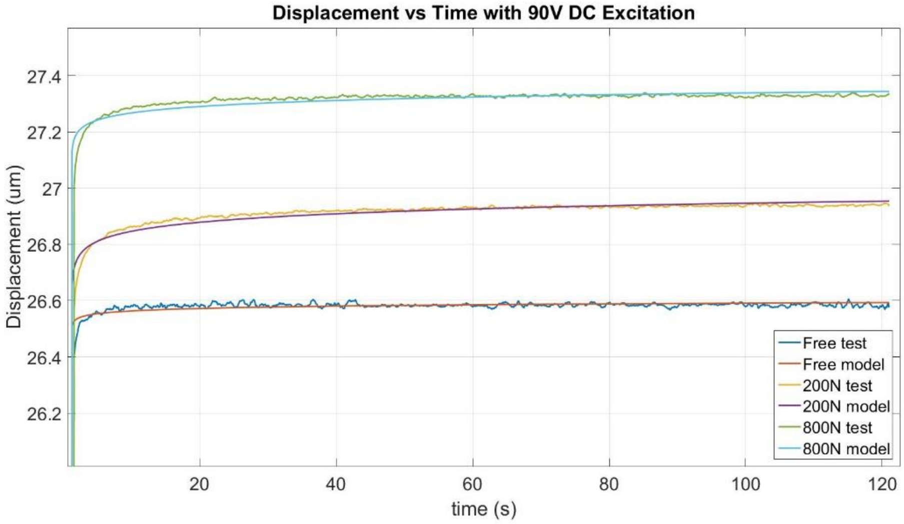

Figure 5.16 Test vs model results with 90V DC excitation under different preloads

Table 5.8 Parameters of creep model with 90V DC excitation

Parameter/ Preload	**Free**	**200 N**	**800 N**
K_c	1.134	1.142	1.162
μ	4.45E-04	1.59E-03	1.12E-03
RMSE (μm)	2.20E-02	1.77E-02	2.00E-02
RRMSE (%)	0.08%	0.07%	0.07%

Examining the RMS error values in the tables above reveals that fractional order model describes the creep behavior quite accurately. Moreover, the results show that while K_c tends to decrease as preload increases, μ tends to increase as preload increases. Since the value of parameter μ directly represents creep effect, it can be concluded that preloading has a negative impact on creep nonlinearity.

5.4 Case Study IV: Amplified Piezo Actuator (APA)

In this case study, using the methodology described in section 3.5, a RTAM is designed via COMSOL, and it is manufactured by wire cutting (EDM) method. Photograph of the RTAM is given in Figure 5.17.

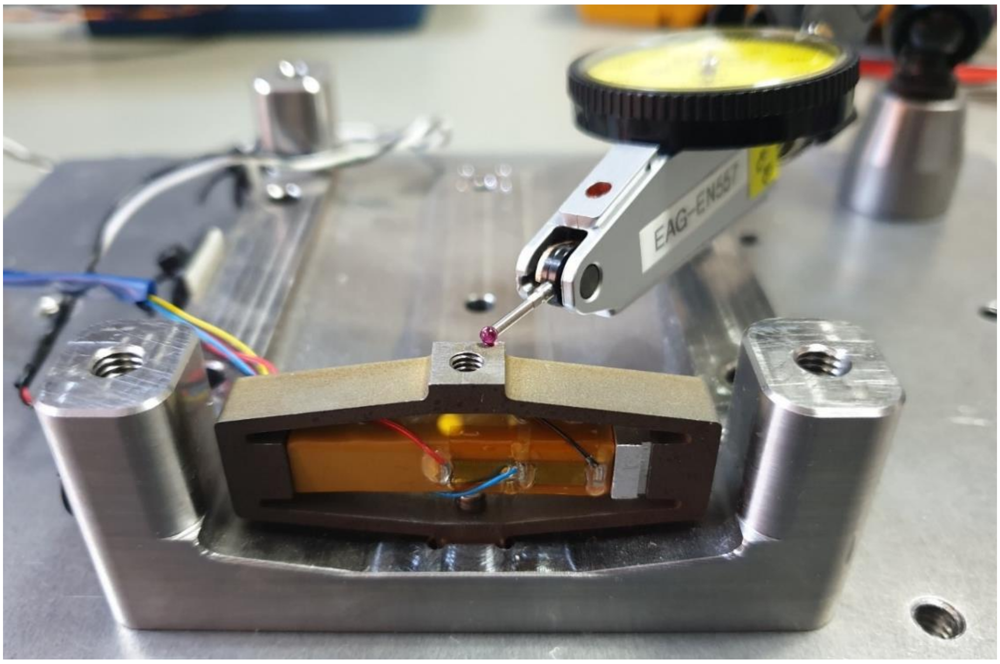

Figure 5.17 RTAM

The mesh used in the COMSOL model is illustrated in the figure below. Piezoelectric material is modeled with 10368 Quadratic brick elements, while mesh of the remaining parts consist of 161437 quadratic tetrahedral elements. A quadratic discretization is applied for both mechanical (x,y,z) and electrical (ϕ) fields, and total solved number of DOF is 1163320.

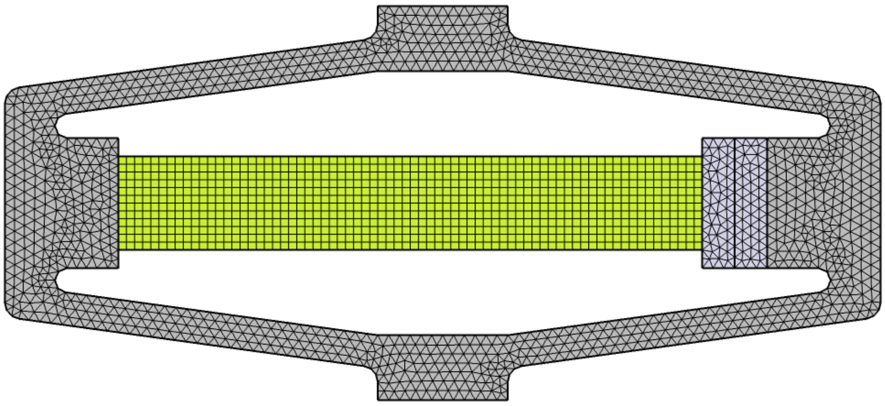

Figure 5.18 Mesh model

Modeling and test results of RTAM are presented in Figure 5.19. It is shown that the results are quite consistent with each other except hysteresis.

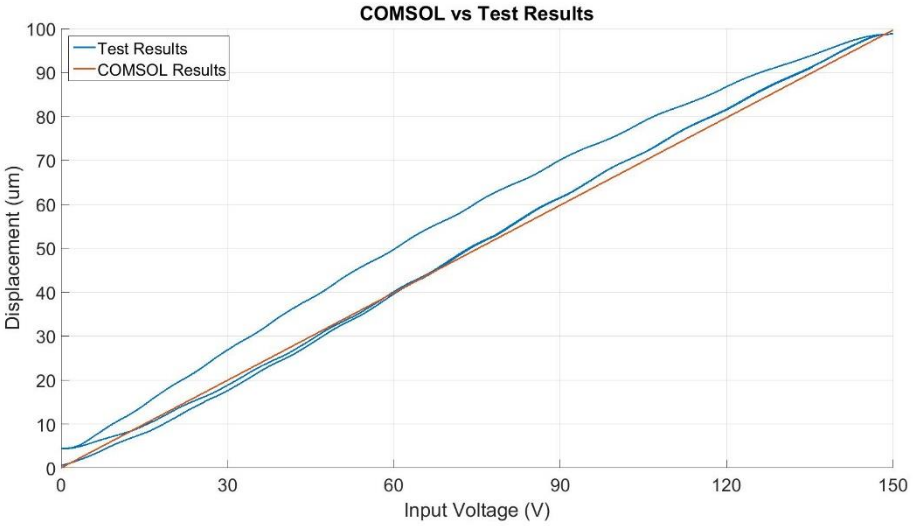

Figure 5.19 Modeling vs Test Results of RTAM

Eigenfrequency analysis is also performed for both free-free and fixed-free boundary conditions. In both configurations, no electrical boundary condition is applied. In fixed-free configuration, all three DOFs of the bottom of the RTAM are fixed, while no mechanical boundary condition is applied in the free-free configuration. Also, in free-free configuration, frequency values of the first six modes (rigid body modes) are zero as expected. Deformed shapes of the first six modes of fixed-free configuration, and the first six elastic modes of free-free configuration are presented in the following figures.

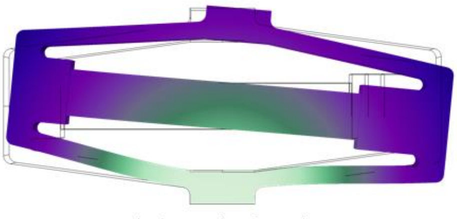

(1st mode shape)

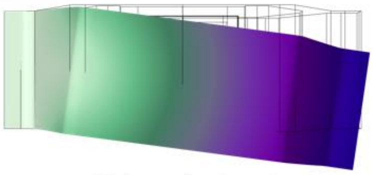

(2nd mode shape)

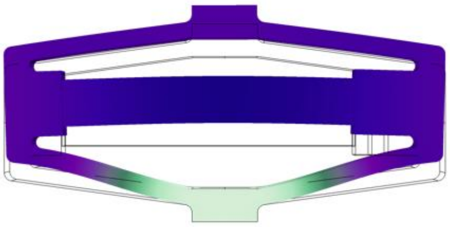

(3rd mode shape)

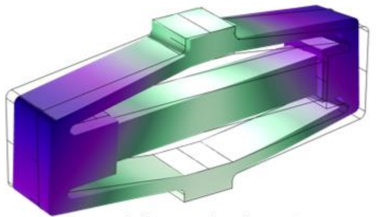

(4th mode shape)

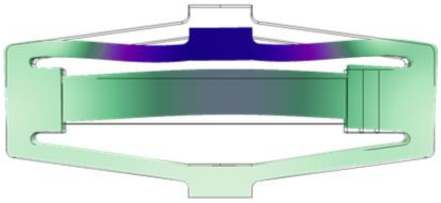

(5th mode shape)

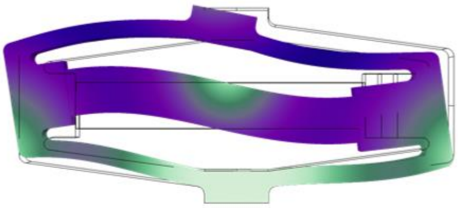

(6th mode shape)

Figure 5.20 Mode shapes of blocked-free configuration

(1st mode shape) (4th mode shape)

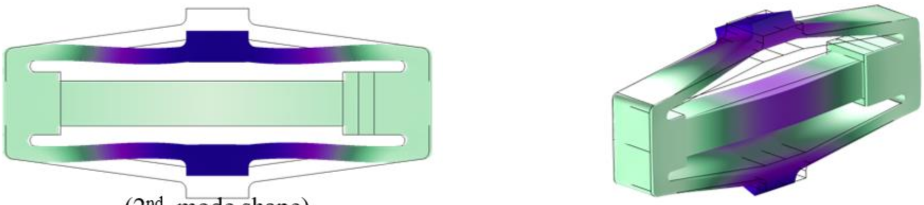

(2nd mode shape) (5th mode shape)

(3rd mode shape) (6th mode shape)

Figure 5.21 mode shapes of free-free configuration

The next table lists the natural frequencies of the initial sixth modes. Possible coupled modes with voltage excitation are highlighted in bold.

Table 5.9 Modal analysis results

Mode number	Fixed-free	Free-free
1st	1040	**4928**
2nd	1136	**5003**
3rd	**1864**	6871
4th	3032	7216
5th	**5185**	8744
6th	5801	8966

In second part of this case study, a numerical analysis is carried out to observe effect of design parameters on mechanical efficiency and natural frequency of the third mode. By using parametric sweep, a series of finite element analysis are performed. While thickness value is increased from 0.4 mm to 2.4 mm with 0.4 mm increments, mechanism angle is changed from 2 to 24 by 2 increments. In the first figure, mechanical efficiency with respect to mechanism angle with different thickness values is plotted, while the second graph is for 3rd natural frequency which is the translation mode that may be excited with electrical excitation.

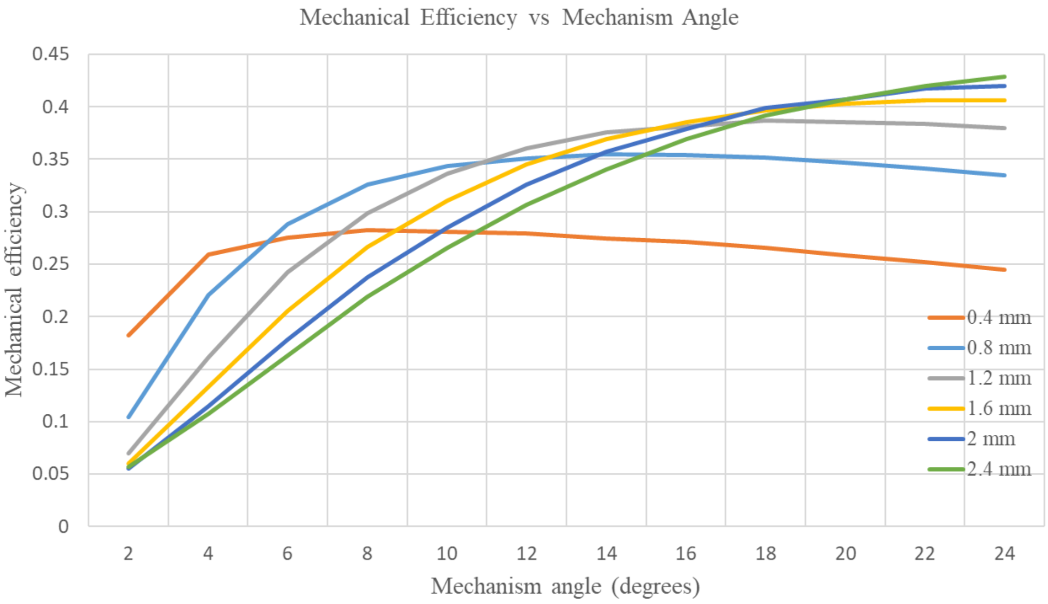

Figure 5.22 Mechanical efficiency vs mechanism angle with different thickness values

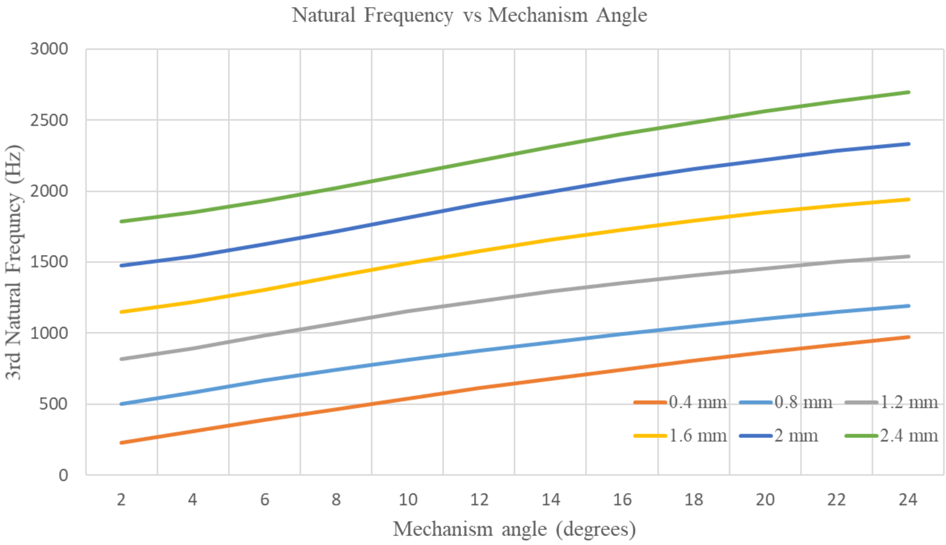

Figure 5.23 3rd natural frequency vs mechanism angle with different thickness values

From the Figure 5.22 and Figure 5.23, the following conclusions can be drawn. Firstly, mechanism angle is the primary parameter which affects mechanical efficiency and natural frequency more than the thickness parameter. Secondly, Figure 5.23 reveals that the corresponding natural frequency has an almost linear relationship with angle and thickness parameters. As a final conclusion, Figure 5.24 shows that mechanically most efficient design point tends to shift as thickness parameter changes. Thus, to design an optimum RTAM, both parameters should be used simultaneously.

As a final work of this case study, the accuracy of amplification ratio formulas in literature are compared in Table 5.10. Mechanism angle (θ) and arm length (l) is demonstrated in the sketch below. Among other parameters, “t” is the arm thickness, and k_t and k_θ are translational and rotational stiffness of mechanism, respectively.

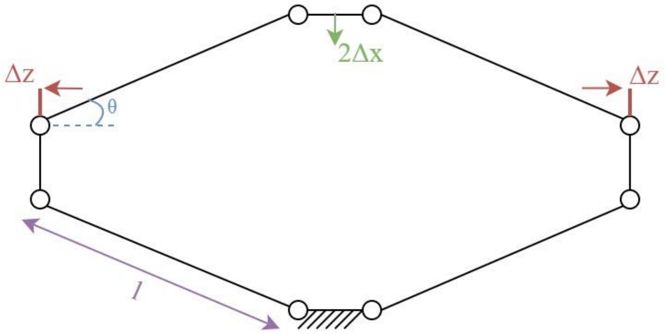

Figure 5.25 RTAM Parameters

Table 5.10 Comparison of R_{amp} formulas

Author(s)	**Formula**	**Type**	**Result**	**Error (%)**
Lobontiu & Garcia [94]	$R_{amp} = \frac{\sqrt{l^2 sin\theta + 2l\Delta z cos\theta - \Delta z^2} - l sin\theta}{\Delta z}$	Geometric	7.07	86.3
Ma [95]	$R_{amp} = \frac{l}{\frac{2k_r}{k_t l} cot\theta + l tan\theta}$	Elastic	4.76	25.4
Shao [96]	$R_{amp} = \frac{l cos\theta}{\frac{t^2 \cos^2\theta}{1.5 l sin\theta} + l sin\alpha}$	Elastic	5.39	41.8
Chen [79]	$R_{amp} = l_a \sin\theta - l_a * \sqrt{1 - \left(\frac{l_a cos\theta + \frac{\Delta z}{2}}{l_a}\right)^2}$	Geometric	3.71	2.26
Qi [97]	$R_{amp} = \frac{\ln\left(\frac{sin\theta}{sin(\theta - \Delta\theta)}\right)}{\Delta\theta}$	Geometric	5.33	40.3
Ling [72]	$R_{amp} = \frac{k_t l^2 sin\theta cos\theta}{12 k_r \cos^2\theta + k_t l^2 \sin^2\theta}$	Elastic	4.76	25.4
Cao [98]	$R_{amp} = \frac{(l^2 - t^2) * sin\theta cos\theta}{l^2 \sin^2\theta + t^2 \cos^2\theta}$	Elastic	4.71	24.1
Zhou [73]	$R_{amp} = cot\theta$	Geometric	7.30	92.2

In general, the table above shows that elastic formulations provide better results than geometric ones because the elastic formulation is more realistic thanks to accounting for decrease in deformation on the arms due to elastic behavior. This case study shows that for amplification ratio calculation finite element method is superior to all formulas in the literature.

CHAPTER 6

SUMMARY CONCLUSIONS AND FUTURE WORK

6.1 SUMMARY

In this study, a generic methodology is given to model and design rhombus type amplifier mechanism driven with piezoelectric stack actuator (PSA). In the first part of the work, piezoelectricity is introduced in a simple manner, then a detailed and comprehensive literature review is conducted about modeling methods and nonlinearities of piezoelectric actuators and amplifier mechanism to explain the objective of the study. The primary goal of this thesis is to provide an accurate nonlinear model for PSA and rhombus type amplification mechanism (RTAM). The secondary objective is obtaining a design guide for such actuators. For this purpose, starting from constitutive equations, piezoelectric linear modeling and finite element modeling methods are presented. Also, a nonlinear model is created to increase modeling accuracy by proposing a novel modified hysteresis model named as multivalued Bouc-Wen model (MVB-W). Following that, experimental setups are explained. Finally, theories are verified with four case studies. In Case Study I, COMSOL background formulation is explained by comparing the results of a single piezoelectric element. For the second and third case studies, hysteresis and creep parameters of proposed models are identified. In the fourth and the last case study, a RTAM manufactured by wire cutting method is investigated, and amplification ratio formulas in the literature are compared. Finally, the main research findings are concluded, and future work is suggested in this chapter.

6.2 CONCLUSIONS

Considering the outcomes of earlier chapters, the research findings led to following conclusions;

- Charge driving and capacitor insertion methods eliminated voltage driving removed hysteresis and creep, however because of implementation difficulty and capacity restriction, voltage driving is a common way to steer PSA despite its hysteresis and creep problem. An accurate nonlinear modeling approach removes this disadvantage of the voltage driving approach.
- Bouc-Wen hysteresis model and its modified versions are not suitable for extended input voltage ranges even though Bouc-Wen is the most commonly used hysteresis model in the literature. Therefore, a new modified Bouc-Wen model is presented to improve the accuracy of modeling.
- It has been revealed that analytical formulas of amplification ratios do not match well with empirical results due to assumptions and simplifications behind the formulas. On the other hand, the finite element method gives very close results to the real results. Thus, instead of taking analytical formula as an objective function, using FEM results will increase the design accuracy. It has been verified that FEM is a better way to design an amplifier mechanism, and FEM could be utilized via COMSOL. Also, it is proved that finite element model for piezoelectric actuators could be created in MATLAB by using Case Study I methodology.
- It has been shown in this study that thickness and mechanism angle are the most critical parameters for RTAM modeling and optimization. Then, a case study is performed to observe sensitivity of thickness and angle parameters on mechanical efficiency and natural frequency. By carrying out this numerical analyses, a general methodology is given to design an optimized RTAM.

- By uniting d_{33}, hysteresis and creep models, a nonlinear SDOF model of PSA is developed in Simulink. Furthermore, the model is upgraded to RTAM model by adding mechanism stiffness and amplification ratio. The suitability of proposed techniques is verified through experiments. Although it has been shown that proposed SDOF model represents hysteresis and creep behavior with high matching performance, identification process is the main limitation of this model. While there are two (K_c and μ) parameters need to be identified in creep model, the number is five (α_1, α_2, β_1, β_2 and γ) for hysteresis model. Another limitation the SDOF model is the deviation from the actual results when operating near the modes shown in Figure 5.20, especially for the modes that are not coupled with voltage excitation.
- Prestress has a significant effect on hysteresis, creep and therefore on d_{33}. For this reason, at which prestress value the actuator will be used, its parameters should be identified at that prestress level. Ignoring prestress may reduce modeling precision by a significant amount.

6.3 FUTURE WORK

As future work of this study, the following improvements could be made;

- Based on this developed precise nonlinear model, a controller with a high bandwith can be designed.
- In COMSOL, a two or four-axis orientation stage could be designed based on proposed modeling methodology. Also, the nonlinear model of RTAM may be upgraded to the stage model by adding stiffness values that come from other stage mechanical parts like hinges, blades, etc.
- The modeling methodology of this study can be tested with different PSAs to validate the proposed MVB-W model and nonlinear d_{33} model. Also, observing the effects of prestress in different PSAs, allows for more inclusive and precise models to be created.

- Based on FEM results, an empirical R_{amp} formula could be obtained with parameters like thickness, arm angle and arm length.
- A shape optimization could be done on the arms of the RTAM. Instead of pure rhombus, a more optimized organic geometry could be obtained.
- Temperature dependent behavior of PSA may be investigated to be able to model accurately in the broader temperature range.
- Another experimental case study can be carried out to characterize piezo mass, stiffness and damping terms, or PSA transfer function could be extracted from COMSOL as state-space matrix.
- A nonlinear finite element analysis could be done by adding creep and hysteresis nonlinearities to system matrices derived from COMSOL.

REFERENCES

[1] H. S. Tzou, H. J. Lee, and S. M. Arnold, “Smart materials, precision sensors/actuators, smart structures, and structronic systems,” *Mech. Adv. Mater. Struct.*, vol. 11, no. 4–5, pp. 367–393, 2004, doi: 10.1080/15376490490451552.

[2] I. F. Lüleci, “Active vibration control of beam and plates by using piezoelectric patch actuators,” Middle East Technical University, M.S Thesis, 2013.

[3] M. Trainer, “Kelvin and piezoelectricity,” *Eur. J. Phys.*, vol. 24, no. 5, pp. 535–542, 2003, doi: 10.1088/0143-0807/24/5/310.

[4] W. P. Mason, “Piezoelectricity, its history and applications,” *J. Acoust. Soc. Am.*, vol. 70, no. 6, pp. 1561–1566, 1981, doi: 10.1121/1.387221.

[5] K. Uchino, *The Development of Piezoelectric Materials and the New Perspective*, 2nd ed. Elsevier Ltd., 2017.

[6] P. Dineva, *Dynamic Fracture of Piezoelectric Materials - Chapter 2: Piezoelectric Materials*, no. Solid Mechanics and its applications-212. 2014.

[7] A. V. Carazo, “Piezoelectric transformers: An historical review,” *Actuators*, vol. 5, no. 2, 2016, doi: 10.3390/act5020012.

[8] H. Kawai, “The Piezoelectricity of Poly (vinylidene Fluoride),” *Jpn. J. Appl. Phys.*, vol. 8, no. 7, pp. 975–976, 1969, doi: 10.1143/jjap.8.975.

[9] K. Uchino, *Advanced Piezoelectric Materials Science and Technology*. 2008.

[10] S. O. R. Moheimani and A. J. Fleming, *Piezoelectric transducers for vibration control and damping (advances in industrial control)*. 2006.

[11] S. J. Rupitsch, *Piezoelectric Sensors and Actuators*. 2018.

[12] J. Choi, J. Lee, B. Hahn, W. Yoon, and D. Park, “Co-firing of PZN-PZT / Ag multilayer actuator prepared by tape-casting method,” vol. 43, pp. 483–490, 2008, doi: 10.1016/j.materresbull.2007.02.033.

[13] Y. Yan, A. Marin, Y. Zhou, and S. Priya, “Enhanced Vibration Energy Harvesting Through Multilayer Textured Pb(Mg1/3Nb2/3)O3–PbZrO3–PbTiO3 Piezoelectric Ceramics,” *Energy Harvest. Syst.*, vol. 1, no. 3–4, 2014, doi: 10.1515/ehs-2014-0001.

[14] P. Groen, *An Introduction to Piezoelectric Materials and Components*. 2018.

[15] X. Chen *et al.*, “Identical scaling behavior of saturated dynamic hysteresis in rhombohedral lead zirconate titanate bulk ceramics,” *J. Appl. Phys.*, vol. 114, no. 24, 2013, doi: 10.1063/1.4858355.

[16] H. Li, Y. Xu, M. Shao, L. Guo, and D. An, “Analysis for hysteresis of piezoelectric actuator based on microscopic mechanism,” *IOP Conf. Ser. Mater. Sci. Eng.*, vol. 399, no. 1, 2018, doi: 10.1088/1757-899X/399/1/012031.

[17] Y. Zhang and T. F. Lu, “On an equivalent model of multi-layer piezoelectric actuators for facilitating finite element simulations,” *Microsyst. Technol.*, vol. 25, no. 12, pp. 4455–4464, 2019, doi: 10.1007/s00542-019-04464-6.

[18] X. Liu, J. Wang, and W. Li, “Dynamic analytical solution of a piezoelectric stack utilized in an actuator and a Generator,” *Appl. Sci.*, vol. 8, no. 10, 2018, doi: 10.3390/app8101779.

[19] P. E. Bloomfield, “Multilayer Transducer Transfer Matrix Formalism,” vol. 49, no. 9, pp. 1300–1311, 2002, doi: 10.1109/TUFFC.2002.1041547.

[20] M. Goldfarb and N. Celanovic, “Modeling Piezoelectric Stack acutators for Control of Micromanipulation,” pp. 69–79, 1997, doi: 10.1109/37.588158.

[21] H. Allik and T. J. R. Hughes, “Finite element method for piezoelectric vibration,” *Int. J. Numer. Methods Eng.*, vol. 2, no. 2, pp. 151–157, 1970, doi: 10.1002/nme.1620020202.

[22] V. Piefort, “Finite Element Modelling of Piezoelectric Active Structures,” Universite Libre de Bruxelles, PhD Thesis, 2001.

[23] V. T. Nguyen, P. Kumar, and J. Y. C. Leong, “Finite element modellingand simulations of piezoelectric actuators responses with uncertainty quantification,” *Computation*, vol. 6, no. 4, pp. 1–20, 2018, doi: 10.3390/computation6040060.

[24] G. Gu, L. Zhu, C. Su, and S. Member, “Modeling and Control of Piezo-Actuated Nanopositioning Stages : A Survey,” *IEEE Trans. Automat. Contr.*, pp. 1–20, 2014.

[25] C. Yang, C. Li, and J. Zhao, “IEEE TRANSACTIONS ON INDUSTRIAL ELECTRONICS A Nonlinear Charge Controller with Tunable Precision for Highly Linear Operation of Piezoelectric Stack Actuators,” vol. 0046, no. c, 2017, doi: 10.1109/TIE.2017.2698398.

[26] R. C. Barrett and C. F. Quate, “Optical scan-correction system applied to atomic force microscopy,” *Rev. Sci. Instrum.*, vol. 62, no. 6, pp. 1393–1399, 1991, doi: 10.1063/1.1142506.

[27] J. Minase, T. F. Lu, B. Cazzolato, and S. Grainger, “A review, supported by experimental results, of voltage, charge and capacitor insertion method for driving piezoelectric actuators,” *Precis. Eng.*, vol. 34, no. 4, pp. 692–700, 2010, doi: 10.1016/j.precisioneng.2010.03.006.

[28] M. Bazghaleh, S. Grainger, and M. Mohammadzaheri, “A review of charge

methods for driving piezoelectric actuators," *J. Intell. Mater. Syst. Struct.*, vol. 29, no. 10, pp. 2096–2104, 2018, doi: 10.1177/1045389X17733330.

[29] H. Search, C. Journals, A. Contact, M. Iopscience, S. Mater, and I. P. Address, "Charge driven piezoelectric actuators for structural vibration control : issues and implementation," vol. 575, doi: 10.1088/0964-1726/14/4/016.

[30] D. V. Sabarianand, P. Karthikeyan, and T. Muthuramalingam, "A review on control strategies for compensation of hysteresis and creep on piezoelectric actuators based micro systems," *Mech. Syst. Signal Process.*, vol. 140, p. 106634, 2020, doi: 10.1016/j.ymssp.2020.106634.

[31] Y. Yang, B. Yang, and M. Niu, "Parameter identification of Jiles–Atherton model for magnetostrictive actuator using hybrid niching coral reefs optimization algorithm," *Sensors Actuators, A Phys.*, vol. 261, pp. 184–195, 2017, doi: 10.1016/j.sna.2017.05.009.

[32] R. C. Smith and Z. Ounaies, "Domain wall model for hysteresis in piezoelectric materials," *J. Intell. Mater. Syst. Struct.*, vol. 11, no. 1, pp. 62–79, 2000, doi: 10.1106/HPHJ-UJ4D-E9D0-2MDY.

[33] W. Zhu and D. Wang, "Sensors and Actuators A : Physical Non-symmetrical Bouc – Wen model for piezoelectric ceramic actuators," *Sensors Actuators A. Phys.*, vol. 181, pp. 51–60, 2012, doi: 10.1016/j.sna.2012.03.048.

[34] V. Hassani, T. Tjahjowidodo, and T. N. Do, "A survey on hysteresis modeling , identification and control," *Mech. Syst. Signal Process.*, pp. 1–25, 2014, doi: 10.1016/j.ymssp.2014.04.012.

[35] Y. Qin, H. Duan, and J. Han, "of Piezoelectric Actuators Using Adaptive Kalman Filter," vol. 69, no. 9, pp. 9385–9395, 2022.

[36] J. Liu, J. Wang, and Q. Zou, "Decomposition-Learning-Based Output Tracking to Simultaneous Hysteresis and Dynamics Control: High-Speed Large-Range Nanopositioning Example," *IEEE Trans. Control Syst. Technol.*, vol. 29, no. 4, pp. 1775–1782, 2020, doi: 10.1109/tcst.2020.3018596.

[37] W. Li, L. Nie, Y. Liu, and M. Zhou, "Rate dependent krasnoselskii-pokrovskii modeling and inverse compensation control of piezoceramic actuated stages," *Sensors (Switzerland)*, vol. 20, no. 18, pp. 1–17, 2020, doi: 10.3390/s20185062.

[38] J. Gan, Z. Mei, X. Chen, Y. Zhou, and M. F. Ge, "A modified Duhem model for rate-dependent hysteresis behaviors," *Micromachines*, vol. 10, no. 10, 2019, doi: 10.3390/mi10100680.

[39] M. Armin, P. N. Roy, and S. K. Das, "A Survey on Modelling and Compensation for Hysteresis in High Speed Nanopositioning of AFMs: Observation and Future Recommendation," *Int. J. Autom. Comput.*, vol. 17,

no. 4, pp. 479–501, 2020, doi: 10.1007/s11633-020-1225-4.

[40] M. Rakotondrabe, “Bouc – Wen Modeling and Inverse Multiplicative Structure Actuators,” *IEEE Trans. Autom. Sci. Eng.*, vol. 8, no. 2, pp. 428–431, 2011.

[41] P. Z. Li, D. F. Zhang, J. Y. Hu, B. Lennox, and F. Arvin, “Hysteresis modelling and feedforward control of piezoelectric actuator based on simplified interval type-2 fuzzy system,” *Sensors (Switzerland)*, vol. 20, no. 9, 2020, doi: 10.3390/s20092587.

[42] C. Yang, N. Verbeek, F. Xia, Y. Wang, and K. Youcef-Toumi, “Modeling and Control of Piezoelectric Hysteresis: A Polynomial-Based Fractional Order Disturbance Compensation Approach,” *IEEE Trans. Ind. Electron.*, vol. 68, no. 4, pp. 3348–3358, 2021, doi: 10.1109/TIE.2020.2977567.

[43] G. Gu and L. Zhu, “Modeling of rate-dependent hysteresis in piezoelectric actuators using a family of ellipses,” *Sensors Actuators, A Phys.*, vol. 165, no. 2, pp. 303–309, 2011, doi: 10.1016/j.sna.2010.09.020.

[44] J. Gan and X. Zhang, “A review of nonlinear hysteresis modeling and control of piezoelectric actuators,” *AIP Adv.*, vol. 9, no. 4, 2019, doi: 10.1063/1.5093000.

[45] R. Bouc, “Forced vibration of mechanical systems with hysteresis,” *Proc. Conf. Nonlinear Oscil. Prague.*, pp. 32–39, 1967.

[46] Y. K. Wen, “Method for random vibration of hysteresis systems,” *J Eng. Mech. Div.*, vol. 120, pp. 249–263, 1976.

[47] M. Ismail, F. Ikhouane, and J. Rodellar, “The hysteresis Bouc-Wen model, a survey,” *Arch. Comput. Methods Eng.*, vol. 16, no. 2, pp. 161–188, 2009, doi: 10.1007/s11831-009-9031-8.

[48] M. S. Sofla, F. Barazandeh, S. M. Rezaei, M. Zareinejad, and M. Saadat, “Observer-based robust motion control of a piezo-actuated stage under external disturbances,” *Trans. Inst. Meas. Control*, vol. 34, no. 4, pp. 365–375, 2012, doi: 10.1177/0142331210380993.

[49] S. Naz, M. A. Z. Raja, A. Mehmood, A. Zameer, and M. Shoaib, “Neuro-intelligent networks for Bouc–Wen hysteresis model for piezostage actuator,” *Eur. Phys. J. Plus*, vol. 136, no. 4, 2021, doi: 10.1140/epjp/s13360-021-01382-3.

[50] N. Ngoc, C. Van Kien, H. Pham, and H. Anh, “Engineering Applications of Artificial Intelligence Parameters identification of Bouc – Wen hysteresis model for piezoelectric actuators using hybrid adaptive differential evolution and Jaya algorithm ☆,” *Eng. Appl. Artif. Intell.*, vol. 87, no. October 2019, p. 103317, 2020, doi: 10.1016/j.engappai.2019.103317.

[51] C. Qian, Q. Ouyang, Y. Song, and W. Zhao, “Hysteresis modeling of piezoelectric actuators with the frequency-dependent behavior using a hybrid model,” *Proc. Inst. Mech. Eng. Part C J. Mech. Eng. Sci.*, vol. 234, no. 9, pp. 1848–1858, 2020, doi: 10.1177/0954406219897089.

[52] W. Zhu and X. T. Rui, “Hysteresis modeling and displacement control of piezoelectric actuators with the frequency-dependent behavior using a generalized Bouc-Wen model,” *Precis. Eng.*, vol. 43, pp. 299–307, 2016, doi: 10.1016/j.precisioneng.2015.08.010.

[53] G. Wang, G. Chen, and F. Bai, “Sensors and Actuators A : Physical Modeling and identification of asymmetric Bouc – Wen hysteresis for piezoelectric actuator via a novel differential evolution algorithm,” vol. 235, pp. 105–118, 2015.

[54] M. Ming, Z. Feng, J. Ling, and X. Xiao, “Hysteresis modelling and feedforward compensation of piezoelectric nanopositioning stage with a modified Bouc-Wen model,” *Micro Nano Lett.*, vol. 13, no. 8, pp. 1170–1174, 2018, doi: 10.1049/mnl.2017.0793.

[55] J. Gan and X. Zhang, “An enhanced Bouc-Wen model for characterizing rate-dependent hysteresis of piezoelectric actuators,” *Rev. Sci. Instrum.*, vol. 89, no. 11, 2018, doi: 10.1063/1.5038591.

[56] J. Gan and X. Zhang, “Nonlinear hysteresis modeling of piezoelectric actuators using a generalized Bouc-Wen model,” *Micromachines*, vol. 10, no. 3, pp. 1–12, 2019, doi: 10.3390/mi10030183.

[57] M. Shao, Y. Wang, Z. Gao, and X. Zhu, “Discrete-time rate-dependent hysteresis modeling and parameter identification of piezoelectric actuators,” *Trans. Inst. Meas. Control*, vol. 44, no. 10, pp. 1968–1978, 2022, doi: 10.1177/01423312211069364.

[58] S. Kang, H. Wu, Y. Li, X. Yang, and J. Yao, “A Fractional-Order Normalized Bouc-Wen Model for Piezoelectric Hysteresis Nonlinearity,” *IEEE/ASME Trans. Mechatronics*, vol. 27, no. 1, pp. 126–136, 2022, doi: 10.1109/TMECH.2021.3058851.

[59] L. Liu, H. Yun, Q. Li, X. Ma, S. L. Chen, and J. Shen, “Fractional Order Based Modeling and Identification of Coupled Creep and Hysteresis Effects in Piezoelectric Actuators,” *IEEE/ASME Trans. Mechatronics*, vol. 25, no. 2, pp. 1036–1044, 2020, doi: 10.1109/TMECH.2020.2974978.

[60] H. Jung and D. G. Gweon, “Creep characteristics of piezoelectric actuators,” *Rev. Sci. Instrum.*, vol. 71, no. 4, pp. 1896–1900, 2000, doi: 10.1063/1.1150559.

[61] Y. Liu, J. Shan, and N. Qi, “Creep modeling and identification for piezoelectric actuators based on fractional-order system,” *Mechatronics*, vol.

23, no. 7, pp. 840–847, 2013, doi: 10.1016/j.mechatronics.2013.04.008.

[62] Y. Liu, J. Shan, U. Gabbert, and N. Qi, “Hysteresis and creep modeling and compensation for a piezoelectric actuator using a fractional-order Maxwell resistive capacitor approach,” *Smart Mater. Struct.*, vol. 22, no. 11, 2013, doi: 10.1088/0964-1726/22/11/115020.

[63] M. Ling, J. Cao, Z. Jiang, M. Zeng, and Q. Li, “Optimal design of a piezo-actuated 2-DOF millimeter-range monolithic flexure mechanism with a pseudo-static model,” *Mech. Syst. Signal Process.*, vol. 115, no. June, pp. 120–131, 2019, doi: 10.1016/j.ymssp.2018.05.064.

[64] F. Chen, Q. Zhang, Y. Gao, and W. Dong, “A review on the flexure-based displacement amplification mechanisms,” *IEEE Access*, vol. 8, pp. 205919–205937, 2020, doi: 10.1109/ACCESS.2020.3037827.

[65] J. Hricko, “Compliant Mechanisms for Motion / Force Amplifiers for Robotics Compliant Mechanisms for Motion / Force Amplifiers for Robotics,” no. October 2019, 2020, doi: 10.1007/978-3-030-19648-6.

[66] W. Dong *et al.*, “Development and analysis of a bridge-lever-type displacement amplifier based on hybrid flexure hinges,” *Precis. Eng.*, no. January, pp. 0–1, 2018, doi: 10.1016/j.precisioneng.2018.04.017.

[67] M. Ling, X. He, M. Wu, and L. Cao, “Dynamic Design of a Novel High-Speed Piezoelectric Flow Control Valve Based on Compliant Mechanism,” *IEEE/ASME Trans. Mechatronics*, pp. 1–9, 2022, doi: 10.1109/tmech.2022.3169761.

[68] Y. K. Yong and S. S. Aphale, “Design , Identification , and Control of a Flexure-Based XY Stage for Fast Nanoscale Positioning,” no. February, 2009, doi: 10.1109/TNANO.2008.2005829.

[69] G. Chen, Y. Ma, and J. Li, “Sensors and Actuators A : Physical A tensural displacement amplifier employing elliptic-arc flexure hinges,” *Sensors Actuators A. Phys.*, vol. 247, pp. 307–315, 2016, doi: 10.1016/j.sna.2016.05.015.

[70] X. Sun *et al.*, “Design and analysis of a large-range precision micromanipulator,” *Smart Mater. Struct.*, vol. 28, no. 11, 2019, doi: 10.1088/1361-665X/ab4413.

[71] K. Kim, J. Lee, J. Ju, and D. Kim, “International Journal of Solids and Structures Compliant cellular materials with compliant porous structures : A mechanism based materials design,” *Int. J. Solids Struct.*, vol. 51, no. 23–24, pp. 3889–3903, 2014, doi: 10.1016/j.ijsolstr.2014.07.006.

[72] M. Ling, J. Cao, M. Zeng, J. Lin, and D. J. Inman, “Enhanced mathematical modeling of the displacement amplification ratio for piezoelectric compliant mechanisms,” *Smart Mater. Struct.*, vol. 25, no. 7, pp. 1–11, 2016, doi:

10.1088/0964-1726/25/7/075022.

[73] C. Zhou, J. Li, J. Duan, and G. Deng, “Direct-Acting Piezoelectric Jet Dispenser With Rhombic Mechanical Amplifier,” vol. 8, no. 5, pp. 910–913, 2018.

[74] Q. Lu, X. Chen, and W. Huang, “A Novel Rhombic Piezoelectric Actuator Applied in Precision Positioning Stage,” vol. 23, no. 3, pp. 405–411, 2020.

[75] S. Shao, M. Xu, S. Zhang, and S. Xie, “Stroke maximizing and high efficient hysteresis hybrid modeling for a rhombic piezoelectric actuator,” *Mech. Syst. Signal Process.*, vol. 75, pp. 631–647, 2016, doi: 10.1016/j.ymssp.2015.12.007.

[76] S. Chen, M. Ling, and X. Zhang, “Design and experiment of a millimeter-range and high-frequency compliant mechanism with two output ports,” *Mech. Mach. Theory*, vol. 126, pp. 201–209, 2018, doi: 10.1016/j.mechmachtheory.2018.04.003.

[77] W. Diao, Y. Ye, J. Chen, Q. Pan, and Z. Feng, “Effect of the compressible spaces on the performance of piezoelectric pump with rhombic micro-displacement amplifying vibrator,” *J. Intell. Mater. Syst. Struct.*, vol. 32, no. 20, pp. 2494–2504, 2021, doi: 10.1177/1045389X211006899.

[78] M. Ling, J. Cao, Z. Jiang, and Q. Li, “Development of a multistage compliant mechanism with new boundary constraint,” *Rev. Sci. Instrum.*, vol. 89, no. 1, 2018, doi: 10.1063/1.5007890.

[79] J. Chen, C. Zhang, M. Xu, Y. Zi, and X. Zhang, “Rhombic micro-displacement amplifier for piezoelectric actuator and its linear and hybrid model,” *Mech. Syst. Signal Process.*, vol. 50–51, pp. 580–593, 2015, doi: 10.1016/j.ymssp.2014.05.047.

[80] A. Erturk and D. J. Inman, *Piezoelectric energy harvesting*. 2016.

[81] A. American and N. Standard, “An American National Standard: IEEE Standard on Piezoelectricity,” *IEEE Trans. Sonics Ultrason.*, vol. 31, no. 2, pp. 8–10, 1984, doi: 10.1109/T-SU.1984.31464.

[82] J. H. Kim, S. H. Kim, and Y. K. Kwak, “Development and optimization of 3-D bridge-type hinge mechanisms,” *Sensors Actuators, A Phys.*, vol. 116, no. 3, pp. 530–538, 2004, doi: 10.1016/j.sna.2004.05.027.

[83] J. H. Kim, S. H. Kim, and Y. K. Kwaka, “Development of a piezoelectric actuator using a three-dimensional bridge-type hinge mechanism,” *Rev. Sci. Instrum.*, vol. 74, no. 5, pp. 2918–2924, 2003, doi: 10.1063/1.1569411.

[84] V. Piefort and A. Preumont, “Finite element modeling of piezoelectric structures,” *Samtech User’s Conf.*, no. December, pp. 1–17, 2001, [Online]. Available:

http://www.ulb.ac.be/scmero/documents/piezo/js2001%7B_%7Dulb%7B_%7Dvp.pdf.

[85] H. S. Tzou, *Piezoelectric Shells Distributed Sensing and Control of Continua*, vol. 53, no. 9. 2013.

[86] J. Fish and T. Belytschko, *A First Course in Finite Elements*. 2007.

[87] H. S. Tzou and C. I. Tseng, “Distributed piezoelectric sensor/actuator design for dynamic measurement/control of distributed parameter systems: A piezoelectric finite element approach,” *J. Sound Vib.*, vol. 138, no. 1, pp. 17–34, 1990, doi: 10.1016/0022-460X(90)90701-Z.

[88] COMSOL Multiphysics, “Structural Mechanics Module User’s Guide,” p. 454, 2008, [Online]. Available: www.comsol.de.

[89] COMSOL, “COMSOL Multiphysics® v. 5.5 Reference Manual,” p. 1742, 2018.

[90] P. K. Panda, B. Sahoo, S. Raja, V. K. M. P, and V. Shankar, “Electromechanical and Dynamic Characterization of In-House-Fabricated Amplified Piezo Actuator,” vol. 2012, no. Ml, 2012, doi: 10.1155/2012/203625.

[91] K. Knopp, “Multiple-Valued Functions,” in *Theory of Functions Parts I and II, Two Volumes Bound as One*, Dover Publications, 1996, p. 320.

[92] A. Tepljakov, “FOMCON Toolbox for MATLAB,” 2022. https://www.mathworks.com/matlabcentral/fileexchange/66323-fomcon-toolbox-for-matlab (accessed Jul. 13, 2022).

[93] PiezoDrive, “SCL Actuators,” 2022. https://www.piezodrive.com/actuators/sclactuators (accessed Jul. 10, 2022).

[94] N. Lobontiu and E. Garcia, “Analytical model of displacement amplification and stiffness optimization for a class of flexure-based compliant mechanisms,” *Comput. Struct.*, vol. 81, no. 32, pp. 2797–2810, 2003, doi: 10.1016/j.compstruc.2003.07.003.

[95] H. W. Ma, S. M. Yao, L. Q. Wang, and Z. Zhong, “Analysis of the displacement amplification ratio of bridge-type flexure hinge,” *Sensors Actuators, A Phys.*, vol. 132, no. 2, pp. 730–736, 2006, doi: 10.1016/j.sna.2005.12.028.

[96] S. B. Shao, M. L. Xu, J. Chen, and B. Feng, “Optimal design of the large stroke piezoelectric actuator using rhombic mechanism,” pp. 442–446, 2014, doi: 10.1533/9780081002254.442.

[97] K. Q. Qi, Y. Xiang, C. Fang, Y. Zhang, and C. S. Yu, “Analysis of the displacement amplification ratio of bridge-type mechanism,” *Mech. Mach. Theory,* vol. 87, pp. 45–56, 2015, doi:

10.1016/j.mechmachtheory.2014.12.013.

[98] J. Cao, M. Ling, D. J. Inman, and J. Lin, “Generalized constitutive equations for piezo-actuated compliant mechanism,” *Smart Mater. Struct.*, vol. 25, no. 9, pp. 1–10, 2016, doi: 10.1088/0964-1726/25/9/095005.